REPORT DOCUMENTATION PAGE

1. REPORT DATE *(DD-MM-YYYY)*	2. REPORT TYPE	3. DATES COVERED *(From - To)*
04-04-2008	FINAL REPORT	01 Dec 05 - 31 Aug 07

4. TITLE AND SUBTITLE	5a. CONTRACT NUMBER
WAVEFORM FOR ACTIVE SENSING: OPTICAL WAVEFORM DESIGN AND ANALYSIS FOR BALLISTIC IMAGING THROUGH TURBID MEDIA	FA9550-06-1-0047

5b. GRANT NUMBER

05NM271

5c. PROGRAM ELEMENT NUMBER

6. AUTHOR(S)
PEYMAN MILANFAR

5d. PROJECT NUMBER

5e. TASK NUMBER

5f. WORK UNIT NUMBER

7. PERFORMING ORGANIZATION NAME(S) AND ADDRESS(ES)
UNIV OF CALIFORNIA, SANTA CRUZ
SANTA CRUZ, CA 95064

8. PERFORMING ORGANIZATION REPORT NUMBER

9. SPONSORING/MONITORING AGENCY NAME(S) AND ADDRESS(ES)
AF OFFICE OF SCIENTIFIC RESEARCH
875 NORTH RANDOLPH STREET ROOM 3112
ARLINGTON VA 22203

10. SPONSOR/MONITOR'S ACRONYM(S)

11. SPONSOR/MONITOR'S REPORT NUMBER(S)

12. DISTRIBUTION/AVAILABILITY STATEMENT
DISTRIBUTION STATEMENT A: UNLIMITED

13. SUPPLEMENTARY NOTES

14. ABSTRACT

This program was intended to develop theory, a broad range of algorithms and proof of concept in detection, estimation, and reconstruction of objects embedded in turbid media, which hamper visibility (such as fog, clouds, smoke, and other types of aerosol particles).

15. SUBJECT TERMS
Ballistic Imaging

16. SECURITY CLASSIFICATION OF:			17. LIMITATION OF ABSTRACT	18. NUMBER OF PAGES	19a. NAME OF RESPONSIBLE PERSON
a. REPORT	b. ABSTRACT	c. THIS PAGE			
					19b. TELEPHONE NUMBER *(Include area code)*

Final Report

Waveforms for Active Sensing: Optical Waveform Design and
Analysis for Ballistic Imaging Through Turbid Media

Principal Investigator: <u>Peyman Milanfar</u>
Department of Electrical Engineering
University of California
Santa Cruz, CA, 95064

1. Objectives

This program was intended to develop theory, a broad range of algorithms and proof of concept in detection, estimation, and reconstruction of objects embedded in turbid media, which hamper visibility (such as fog, clouds, smoke, and other types of aerosol particles). In particular, the program addresses the following eight specific areas:

1. We exploit recent advances in the physical design of fast optical systems which enable active imaging and ranging with "ballistic" light. In this modality, fast bursts of optical energy are transmitted into a medium, and the ballistic component of light (which travels through a medium with minimal diffusive distortion) is detected in either backscatter from the target, or in trans-illuminated form through the medium.

2. We simultaneously optimize the shape and duration of the optical pulses and the design of the optical detectors to achieve maximum signal detectability. The currently existing ballistic imaging practice has been based largely on ad-hoc choices of the optical waveforms, and static detector designs based on time-gating.

3. We study the ballistic imaging problem as (1) a detection problem where the simple presence or absence of some target and its rough dimensions are sought; and (2) a reconstruction problem, where a full image of the object is to be obtained when possible. The first approach is based on statistical detection theory, whereas the second is a statistical estimation problem.

4. We study two complementary approaches for addressing the detection problem and improving the baseline performance. First, we formulate and use a forward model of the ballistic imaging process to enable the determination of the optimum signaling strategies. Second, to improve the detection performance, we adopt an active heterodyne signaling/sensing which uses temporal modulation of light to significantly improve the detector sensitivity by mitigating the ill effects of amplifier noise.

5. We exploit temporal, spatial, wavelength diversity and coding for ballistic imaging. Most, if not all, ballistic imaging methods described in the literature employ a raster-scanned point-by-point imaging system. Such approaches are inherently limited as they do not take full advantage of the degrees of freedom in the signal space. We study the array imaging framework where multiple emitters will transmit coordinated pulses of light; and for their part, a collection of photon-detecting elements will gather the received data and compute a resultant image. In addition to this spatial component, and the temporal modulations introduced for the heterodyne signaling framework, the wavelength of light may also be used to advantage and adapted. Furthermore, there is the possibility of analyzing various ways of coding these pulses (e.g. transmitting sequences of pulses as is done in Ultra-Wide-Band communications).

6. We study novel multi-scale approaches to the photon-limited image reconstruction problem. Recently developed methodology in this area will enable imaging through turbid media at very low average photon counts. Meanwhile, adaptive sampling strategies, motivated by the same multi-scale models, have also been considered. These will allow for a coarse-to-fine sampling strategy which will bootstrap few coarse (but less noisy) samples, to guide the selection of higher resolution samples to form a complete image.

7. Theoretical models for the detection and estimation problems developed above are subjected to sensitivity analysis, hence yielding fundamental performance bounds in the form of (1) analytical relationships between minimum required SNR's to achieve a particular detection power, and (2) mean-squared error bounds that will demonstrate how the performance of the image estimation problem will depend upon the underlying physical and sensor parameters. Relationships thus derived can then be used to optimize system performance (e.g. by minimizing the Cramér-Rao bound for instance for an estimation problem.)

8. Proof of concept is carried out in both the desk-top and the bench-top. We build simulated models of the forward ballistic light transport process and test the signaling strategies and detection algorithms with this model.

2. Status of Effort

The work during the past 15 month has culminated in several peer reviewed publications, which are attached to this report. The topics we have addressed include the following:

1. Collection of existing data for light propagation through turbid media which enabled us to move forward with the analytical work without having to wait for the experimental setup to be completed. As will be explained later in this document, aside from the data generated at our UCSC lab, we have experimented on several data sets generated by the leading physics research groups in the area of ultrafast ballistic imaging (City University of New York and Università della Tuscia, Italy).

2. Forward Modeling and Simulation of ballistic and diffuse data. A forward model of light propagation through turbid media allows us to formulate analytical detection and estimation problems and study the performance bounds. We have combed the literature, and identified the most appropriate and parsimonious models which can be used to describe light propagation through turbid media. We have validated these models using statistical means (Adjusted R^2 goodness of fit) against real data.

3. UCSC laboratory setup and data collection are completed which enabled us to produce data under controlled conditions to aid model development and verification of the performance of proposed analytical algorithms. UCSC laboratory is developed in order to be flexible for active waveform design. Single point optical autocorrelation, and repeatable Ballistic Imaging experiments have already been demonstrated in this laboratory.

4. Development of detection algorithms based upon ballistic and diffuse data is completed. In trans-illumination mode, such algorithms enable the detection of objects present between a transmitting light source and a detector. The output of this process is a "binary" image, indicating the presence or absence of obstructing objects. For instance, looking down a foggy road, we can anticipate the presence of enemy soldiers or vehicles. We have derived ROC curves for detection of a canonical object using current state of the art (time-gating) methods. We showed improvement upon these ROC curves by developing appropriate optimal statistical signal processing methods.

5. Development of image reconstruction and denoising algorithms based upon ballistic and diffuse data is completed. Image reconstruction allows for computation of a more sophisticated output. Namely the output of this stage is a gray-level image (or a sequence of images) that indicate not only the presence

or absence of objects, but also the relative reflectivity (in reflection mode) or opaqueness (in trans-illumination mode) of objects of interest in the turbid medium. Using the measure of relative PSNR (Peak Signal to Noise Ratio), compared to the state of the art (time-gating) image capture, images reconstructed using methods developed by Milanfar et al. and Nowak et al. showed improvement of about 10 dB relative to direct ballistic image reconstruction procedures previously proposed in the literature.

6. Development of performance characteristics/bounds on above algorithms based upon the forward model is completed. Performance analysis and bounds enabled us to understand the limitations inherent in the solution of the detection/estimation problems. Understanding these limitations will help in defining what is possible and impossible. We have already provided analytical formulae for predicting bias, variance (or lower bounds to these) for detection/estimation algorithms.

7. Development of waveform design methodologies to maximize the performance of the above detection/reconstruction algorithms. Using the performance metrics defined above, better design of waveforms and corresponding light detectors will enable improve visibility in turbid media. Some preliminary theoretical work has been already conducted and further work is underway..

3. Accomplishments

Below we present the abstracts of our key recent accomplishments which detail the progress made to date on problems of concern to this program.

- We have investigated and validated a computationally efficient, yet sufficiently accurate mathematical model for light propagation in homogeneous (target absent) and inhomogeneous (target present) turbid media.

- We have derived the fundamental limits on the accuracy of the estimated parameters of the said mathematical model of an unknown turbid medium. This study also guides us toward the most efficient experiments (with respect to both time/accuracy) for calibrating the model parameters of the unknown turbid medium as well as the optical properties of the target (which can be used to identify/categorize it). Our simulation results show that for the medium of most interest, namely heavy fog; optical parameters can be estimated with very high accuracy. These experiments are equally valid in assessing the effectiveness of our imaging techniques in virtually any unknown turbid medium.

4

- We used the said model to derive optimal statistical tests for detecting objects hidden in turbid media. Performance analysis was carried out by computing ROC curves for the proposed optimal tests, showing that by considering only the ballistic photons, we are able to detect opaque objects hidden in heavy fog in the range of approximately 380 meters (i.e. 30 mean-free paths or MFP's). Detection rate of the semi transparent objects are shown to be slightly less than this distance.

- To further improve the detection rate of the aforementioned single pixel optimal detectors and penetrate longer distances in turbid media, we exploited sampling at a diversity of locations in space. We then developed an algorithm based upon the Generalized Likelihood Ratio Test (GLRT) framework which takes advantage of the spatial correlation of nearby samples. In several experiments, we showed that objects of different size and shape that are completely unrecognizable using the common single pixel detection techniques, are detectable with very high accuracy using the said multi-scale technique.

- Considering the effect of diffraction in turbid media, we have derived a lower bound on the achievable spatial resolution of the proposed imaging systems. A basic example of such study is that it is theoretically possible to resolve, with high accuracy, opaque objects of radius on the order of 6mm in heavy fog at a distance of 200 meters.

- To penetrate farther in turbid media, and more importantly to reduce the image scanning time, we have studied and experimented on several adaptive sampling techniques. The experiments preformed using our ballistic imaging laser scanner at UCSC, demonstrate that we may reduce the scanning (imaging) time by as much as a factor of 60 (depending on the shape/size of the target), which is extremely important for imaging in hostile battlefield environments. A theoretic study on the expected gain (in Mean Square Error term) of our proposed adaptive sampling technique is also derived and presented.

- Since the output of adaptive scans are in general irregularly sampled images, we have developed optimal image reconstruction algorithms to effectively reconstruct a high resolution image from a set of irregularly sampled, blurry, noisy images. Moreover, our image reconstruction technique is especially useful as the proposed time resolved holistic imaging system exploits diffused photons as well as the ballistic ones.

- We established the performance tradeoffs between transillumination (TRT) imaging and conventional (un-gated) imaging. On the one hand, time-gated, First arrival photons are unscattered and therefore provide very high spatial resolution. But, very few photons arrive at the detector without scattering, effectively resulting in a very low SNR. On the other hand, conventional (un-gated) imaging is based on

all photons (scattered and unscattered), resulting in lower spatial resolution, but higher SNR (due to the large number of photons). This tradeoff was analyzed using a decision-theoretic approach to ascertain bounds on the minimum resolvable occluding object size with and without time-gated photon acquisition. The theoretical predictions are validated through a realistic simulation of tumors in breast tissue. Our mathematical analysis clearly indicates in which regimes (of turbidity and scattering) TRT imaging outperforms conventional imaging. These theoretical predictions match very well with experimental results. We also developed a novel algorithm for TRT image reconstruction, based on the principle of Maximum Likelihood Estimation. The innovative algorith combines multiple snapshot observations of time-gated photons to reconstruct a high-resolution, low-noise image. In effect, the algorithm allows us to obtain the "best-of-both-worlds" by combining the spatial resolution of the first-arrival photons, with the higher SNR provided by scattered photons.

- We set up a ballistic imaging laboratory at UCSC, enabling us to capture ballistic images with what can be thought of as the "optimal" (500fs) time resolution, as this is virtually the resolution of the generated ballistic pulses.

4. Personnel Supported

Peyman Milanfar, PI
Benjamin Friedlander, Co-PI
Ali Shakouri, Co-PI
Michael Isaacson, Co-PI
Robert Nowak, (Univ. of Wisconsin) Co-PI
Jonathan Saint Clair, (Boeing Co.) Co-PI

Post-docs:
Sina Farsiu
James Christofferson

Graduate Students:
Brian Eriksson
Priyam Chatterjee
Hae Jong Seo

5. Peer-reviewed Technical Publications

"Maximum Likelihood Methods For Time-resolved Imaging Through Turbid Media",
Eriksson, B., Nowak, R., in Proc. of the International Conference on Image Processing, Atlanta, GA, October 2006, pp 641-644

"Robust Kernel Regression for Restoration and Reconstruction of Images from Sparse, Noisy Data"
Takeda, H., S. Farsiu, P. Milanfar, in Proc. of the International Conference on Image Processing, Atlanta, GA, October 2006, pp1257-1260

"A Decision-Theoretic Approach to Transillumination Imaging in Biological Mediums", B. Eriksson And R. Nowak, Proceedings of the IEEE International Symposium on Biomedical Imaging, April 2007.

"Statistical Detection and Imaging of Objects Hidden in Turbid Media Using Ballistic Photons", S. Farsiu, J. Christofferson, B. Eriksson, P. Milanfar, B. Friedlander, A. Shakouri, R. Nowak, Applied Optics, vol. 46, no. 23, pp. 5805-5822, Aug.2007.

"Multi-Scale Statistical Detection and Ballistic Imaging Through Turbid Media", S. Farsiu and P. Milanfar, In proceedings of the IEEE International Conference on Image Processing (ICIP), San Antonio, TX, Sept. 2007.

"Resolution Bounds and Reconstruction Techniques for Time-Resolved Transillumination Imaging", B. Eriksson, and R. Nowak, Submitted to IEEE Transactions on Image Processing, July 2007

6. Interactions/Transitions

The PI, Co-PIs and Post-docs have presented 17 invited talks in the course of this project. These have resulted in excellent technical interactions and dissemination of our work. In many cases, the talks have motivated members of the audience to look at the research problems we are posing, and therefore we believe our work has spurred a healthy amount of new activity in application of statistical signal processing methods to imaging problems. In some cases, these applications have been in unexpected areas such as medical imaging.

6.1 Invited Presentations

Invited Speakers, Peyman Milanfar, Ali Shakouri, Robert Nowak, Waveforms for Active Sensing Program Kick Off Presentations, Washington D.C., Sept 2005

Invited Speakers, Peyman Milanfar, Ali Shakouri, Robert Nowak, Benjamin Friendlander, Waveforms for Active Sensing Program, First Program Review Presentations, Portland, OR, March, 2005

Invited Speaker, Peyman Milanfar, Air Force Office of Scientific Research TCATS Workshop, Tucson, AZ, 2006

Invited Speaker, Peyman Milanfar, DARPA Waveforms for Active Sensing Workshop, Portland, OR, 2006

Invited Speaker, Peyman Milanfar, European Signal Processing Conference, Florence, Italy, 2006

Invited Speaker, Peyman Milanfar, SIAM Conference on Imaging Science, Minneapolis, MN, 2006

Invited Speaker, Sina Farsiu, Department of Electrical and Computer Engineering, University of Wisconsin, Madison, WI, May, 2006

Invited Speaker, Sina Farsiu , Waveforms for Active Sensing Program, Second Program Review Presentation, San-Agustin, FL, September, 2006

Invited Speaker, Peyman Milanfar, International Conference on Image Processing, Atlanta, GA, Oct. 2006

Invited Speaker, Robert Nowak, International Conference on Image Processing, Atlanta, GA, Oct. 2006

Invited Speaker, Sina Farsiu, Duke University Eye Center, Durham, NC, Feb 2007

Invited Speaker, Sina Farsiu, Biomedical Engineering Department, Duke University, Durham, NC, Feb, 2007

Invited Speaker, Sina Farsiu, Sony Electronics, San Jose, CA, Feb. 2007

Invited Speaker, Peyman Milanfar Conference on Applied Inverse Problems, Vancouver, BC, Canada, June 2007

Invited Speaker, Peyman Milanfar , AFOSR Sensing Program Review, Harvard Univ., Cambridge, MA June 2007

Invited Speaker, Peyman Milanfar, SENSIP Center, Arizona State University, Tempe, AZ, March 2007

Invited Speaker, Peyman Milanfar, Center for Advanced Signal and Image Sciences, Lawrence Livermore National Labs, April 2007

6.2 Interactions

Aside from the interactions between the group members, and the members of the other groups in this program, we have made contacts with many prominent researchers in the academic community. Below we list a number of university colleagues who have been consulted:

- Prof. Ines Delfino
  Biophysics & NanoScience Centre
  CNISM - Unità di Ricerca di Viterbo
  Dipartimento di Scienze Ambientali -
  Università della Tuscia, Largo dell'Università, 01100 Viterbo,
  ITALY

- Prof. Robert R. Alfano's Group especially Dr. M. Alrubaiee
  Department of Science And Engineering
  City College and Graduate School, City University of New York
  USA

- Prof. Stefan Dilhaire
  Centre de Physique Moléculaire Optique et Hertzienne – UMR 5798
  University of Bordeaux,
  France

Statistical detection and imaging of objects hidden in turbid media using ballistic photons

Sina Farsiu,[1,*] James Christofferson,[2] Brian Eriksson,[3] Peyman Milanfar,[2] Benjamin Friedlander,[2] Ali Shakouri,[2] and Robert Nowak[3]

[1]Eye Research Center, Duke University, Durham, North Carolina 27710, USA
[2]Electrical Engineering Department, University of California, Santa Cruz, California 95064, USA
[3]Electrical Engineering Department, University of Wisconsin-Madison, Madison, Wisconsin 53706, USA

*Corresponding author: sina.farsiu@duke.edu

We exploit recent advances in active high-resolution imaging through scattering media with ballistic photons. We derive the fundamental limits on the accuracy of the estimated parameters of a mathematical model that describes such an imaging scenario and compare the performance of ballistic and conventional imaging systems. This model is later used to derive optimal single-pixel statistical tests for detecting objects hidden in turbid media. To improve the detection rate of the aforementioned single-pixel detectors, we develop a multiscale algorithm based on the generalized likelihood ratio test framework. Moreover, considering the effect of diffraction, we derive a lower bound on the achievable spatial resolution of the proposed imaging systems. Furthermore, we present the first experimental ballistic scanner that directly takes advantage of novel adaptive sampling and reconstruction techniques.   © 2007 Optical Society of America

OCIS codes: 100.0100, 030.6600, 140.0140, 320.0320.

1. Introduction

High-resolution imaging and detection of objects hidden in a turbid (scattering) medium have long been challenging and important problems with many industrial, military, and medical applications. Although turbid media such as fog, smoke, haze, or body tissue are virtually transparent to radar range electromagnetic waves, the resolution of radar-based imaging systems is often insufficient for many practical applications. Moreover, in some instances the transparency characteristics of certain objects (targets) and the medium are very close in the radar range spectrum, making them practically indistinguishable from each other. On the other hand, although the resolution of imaging systems using ultrashort wavelengths (e.g., x rays) is desirable, there exist potential health hazards for imaging subjects and technicians alike.

As an alternative, imaging systems working in the optical–infrared spectrum range (laser scanners) are potentially able to produce high-resolution images without the likely health hazards. Unfortunately, even a very thin and powerful collimated laser beam quickly diffuses as it travels in turbid media, similar to a car's headlights in fog. Therefore, a naive approach to optical imaging of objects hidden inside a turbid medium results in blurry images where targets are often indistinguishable from each other or the background.

Fortunately, the advent of the new tunable solid-state lasers and ultrafast optical detectors has enabled us to acquire high-quality images through turbid media where the resolution is only limited by diffraction. Although many efficient imaging systems for capturing high-resolution images through turbid media have been proposed throughout the years [1], in this paper we mainly focus on ultrafast time-gated or coherent imaging systems [2]. We note that the proposed methods and analysis are valid and applicable for a great range of imaging systems including optical coherence tomography [3] and x-ray imaging systems.

Ultrafast time-gated imaging is based on scanning the region of interest (ROI) point by point by sending

fast bursts of optical energy (laser pulses) and detecting the unscattered (coherent) photons that have passed through the medium or reflected from the object. Although most of the photons in a laser pulse are either randomly scattered (losing their coherence) or absorbed as they travel through turbid media, across short distances, a few photons keep their coherence and pass through in straight lines without being scattered. These coherent photons are commonly referred to as the ballistic photons. Aside from the diffusive and ballistic photons, the photons that are slightly scattered, retaining some degree of coherence, are referred to as snake photons.

In what follows in this paper, we focus on studying and improving the performance of ballistic imaging systems. In Section 2, we describe a statistical model for the signal and noise in a typical ballistic imaging scenario. Furthermore, we describe optimal methods for characterizing the optical properties of the scattering medium and the semitransparent objects inside it. In Section 3, we study the performance limits of optimal single-pixel detection systems. Moreover, we show that better detection rates are achievable using a multipixel detection technique based on the generalized likelihood ratio test (GLRT) principle. The effect of diffraction on the detection rate is discussed in Section 4. In Section 5, we describe a laboratory setup for detecting ballistic photons and capturing high-resolution images through turbid media, where real experimental data are presented to further clarify the concept of ballistic imaging. In Subsection 5.B, we describe an adaptive sampling scheme that effectively reduces the image acquisition time, making ballistic imaging more suitable for practical applications. A summary and future work directions are given in Section 6, which concludes this paper.

2. Statistical Model for Ballistic Imaging Systems

To have a better understanding of the practical issues involved in photon-limited imaging via ballistic systems, let us consider the imaging system described by Zevallos *et al.* [4] where the pumped Ti:sapphire laser radiates 800 nm pulses at a repetition rate of 1 kHz and an average power of 60 mW. It is easy to show that the energy delivered by the laser during each pulse is

$$e_{\mathrm{pulse}} = \frac{60 \times 10^{-3} \times 1 \text{ s}}{1000} = 6 \times 10^{-5} \text{ J},$$

and the energy of each photon is computed as

$$e = hf = \frac{hc}{\Lambda} = 2.4830 \times 10^{-19} \text{ J},$$

where $h = 6.626 \times 10^{-34}$ is Planck's constant, $c = 299,792,458$ m/s is the speed of light, and $\Lambda = 800$ nm is the wavelength. Now the number of photons in each packet of energy (pulse) is easily

computed as

$$I_0 = \frac{6 \times 10^{-5}}{2.4830 \times 10^{-19}} = 2.4164 \times 10^{14} \text{ photons.} \qquad (1)$$

Because of the statistical nature of pulse propagation, as a laser beam travels through a diffusive medium, it is possible that some of the photons emerge without being scattered. By selecting these unscattered ballistic photons and rejecting the scattered (diffused) ones, it is possible to obtain nonblurred images that are the sharp shadows of targets buried in the diffusive medium.

Since the diffusive and ballistic photons have different path lengths, a femtosecond laser pulse generator and an ultrafast time gate can be paired to separate the relatively slow (delayed) diffusive photons from the ballistic ones. We will say more on a practical setup of a ballistic photon imaging system in Section 5. In what follows in this section, we focus on modeling the detected ballistic photons and noise from a statistical point of view.

A. Modeling Received Signal Power

As expected, in relatively long distances, the number of detected ballistic photons is extremely small. Indeed, Beer's law [5] dictates an exponential relationship between the intensity of the transmitted light and that of the ballistic component as

$$I_b = I_0 \exp\left(-\frac{d}{L}\right). \qquad (2)$$

In this expression, I_0 is the number of the generated photons in one laser pulse before entering the turbid medium, I_b is the number of the ballistic photons that survive traveling through the medium, d is the distance traveled through the medium, $L = 1/\mu_t$ is the mean free path (MFP) length (average distance photons travel before being scattered), and $\mu_t = \mu_s + \mu_a$ is the medium extinction factor (the summation of scattering and absorptive coefficients, respectively). From Eqs. (1) and (2), it is clear that for the laboratory imaging systems with laser power of the order of the one described by Zevallos *et al.* [4], it is fairly unlikely that any ballistic photon survives imaging scenarios where the ratio of d/L is larger than $\sim$30 MFPs. In Appendix A, we have included a detailed decision-theoretic study for defining the critical distance after which the conventional (non-time-gated) imaging systems are preferred to the time-gated ballistic systems.

The exponential drop in the number of received photons is the main prohibitive factor for using such high-resolution optical imaging systems across long distances. In such imaging scenarios, we are forced to rely on the less immediately informative (due to the inherently severe blur) snake and diffusive photons. In recent literature [6,7], an accurate yet computationally manageable mathematical model for diffu-

sive light propagation in turbid media is presented. Cai *et al.* [8] analyzed and experimented on such an imaging modality and Das *et al.* [9] and Gibson *et al.* [10] presented some excellent literature surveys on the subject of diffusive imaging systems. However, imaging systems that are able to time resolve both ballistic and diffusive photons are rather expensive (e.g., a gated optical intensifier camera costs about $100,000) and are not discussed in this paper. Here, we focus on and derive fundamental performance limits for imaging systems that detect ballistic photons only. We exploit these statistical studies to improve the performance of ballistic imaging systems even in long distances where the signal power is weak.

It is important to note that because of the stochastic nature of photon propagation, I_b, calculated in Eq. (2), is merely the expected value of a Poisson random variable that estimates the number of surviving ballistic photons. Moreover, we assume that the received signal at the detector is contaminated with some amount of independent Poisson noise due to shot noise and other degrading effects. Therefore, since the received signal at the detector is the unweighted summation of two Poisson random variables, it can be modeled as a Poisson random process with the following expected value:

$$I = I_0 \exp(-\mu_t d) + X_e = X_s + X_e,$$

where X_e and X_s are the expected values of the noise and signal, respectively. Note that weighted summation of Poisson random variables in general is not Poissonian, which in some cases can be approximated as a truncated Gaussian distribution [11]. However, summation of Poisson random variables with integer weights is yet another Poisson random variable.

B. Characterizing the Optical Properties of the Medium in the Absence of Targets

Accurate characterization of the scattering medium's optical properties is essential for designing optimal detectors. Since light propagation in ballistic imaging systems is described by the single-parameter Beer's law model, we are mostly interested in measuring (characterizing) the medium or semitransparent object's extinction factor.

In the imaging model of Subsection 2.A, the received signal is modeled as a Poisson random variable with probability density function

$$f(\underline{y} | X_{\underline{s}} + X_{\underline{e}}) = \prod_{k=1}^{N} \frac{e^{-(X_{e_k} + X_{s_k})}(X_{e_k} + X_{s_k})^{y_k}}{y_k!}, \qquad (3)$$

where y_k is the kth measurement, $\underline{y} = [y_1, y_2, \ldots, y_k, \ldots, y_N]^T$, $X_{\underline{e}} = [X_{e_1}, X_{e_2}, \ldots, X_{e_k}, \ldots, X_{e_N}]^T$, and $X_{\underline{s}} = [X_{s_1}, X_{s_2}, \ldots, X_{s_k}, \ldots, X_{s_N}]^T$. Note that the laser emits thousands of pulses per second and in practical implementation each spatial position is measured N times to improve the quality of estimation, and therefore the model in Eq. (3) is presented in vector form.

Since the average power of the laser or the detector (and medium) characteristics are assumed not to be changing abruptly, to simplify notations, we assume that $X_{e_1} = X_{e_2} = \ldots = X_{e_N} = X_e$ and $X_{s_1} = X_{s_2} = \ldots = X_{s_N} = X_s$ (extension to the more general time-varying signal and noise case is straight forward). The maximum likelihood (ML) estimate of the medium's extinction factor is given by

$$\frac{\partial \log[f(\underline{y} | X_{\underline{s}} + X_{\underline{e}})]}{\partial \mu_t} = 0 \Rightarrow \hat{\mu}_t = \frac{\ln\left(-\dfrac{NI_0}{NX_e - \sum\limits_{k=1}^{N} y_k}\right)}{d}.$$

Study of the Fisher information matrix (FIM) determines the accuracy of the above estimation scheme. Each element of this matrix can be computed [12] as

$$\mathbb{I}_{i,j} = -E\,\frac{\partial^2 \log[f(\underline{y} | X_{\underline{s}} + X_{\underline{e}})]}{\partial \Theta_i \partial \Theta_j} = \sum_{k=1}^{N}\left(\frac{1}{X_e + X_{s_k}}\frac{\partial X_{s_k}}{\partial \Theta_i}\frac{\partial X_{s_k}}{\partial \Theta_j}\right),$$

where E is the expected value operator and Θ_k is the kth parameter of the model. For the case of characterizing the extinction factor of the medium, the FIM has only one element:

$$\mathbb{I}(\mu_t) = \frac{NI_0^2 d^2 e^{-2\mu_t d}}{X_e + NI_0 e^{-\mu_t d}}.$$

Note that an unbiased estimator can be found that attains the Cramér–Rao bound (CRB), which defines a lower bound on the covariance of any unbiased estimator [13], if and only if the estimator is a linear transformation of the gradient of the log-likelihood (score) function [13,14]

$$\frac{\partial \log[f(\underline{y} | I_0 e^{-\mu_t d} + X_e)]}{\partial \mu_t} \overset{?}{=} \mathbb{I}(\mu_t)(\hat{\mu}_t - \mu_t).$$

Now, since

$$\frac{\partial \log[f(\underline{y} | I_0 e^{-\mu_t d} + X_e)]}{\partial \mu_t} = \mathbb{I}(\mu_t)\left[I_0 d e^{-\mu_t d}(X_e + I_0 e^{-\mu_t d}) - \frac{I_0 d e^{-\mu_t d}}{N}\sum_{k=1}^{N} y_k\right],$$

it is clear that no efficient estimate of the extinction parameter can be found and such estimates will always be biased. This suggests that, in general, the lower bound on the variance of such an estimator cannot be computed by simply inverting the Fisher matrix element. Fortunately, we can numerically show that for the turbid media that are of most interest to us [such as [15] heavy fog ($\mu_t = 12.5^{-1}$ m^{-1}), light fog ($\mu_t = 125^{-1}$ m^{-1}), and haze ($\mu_t = 505.05^{-1}$ m^{-1})], the bias component relative to the
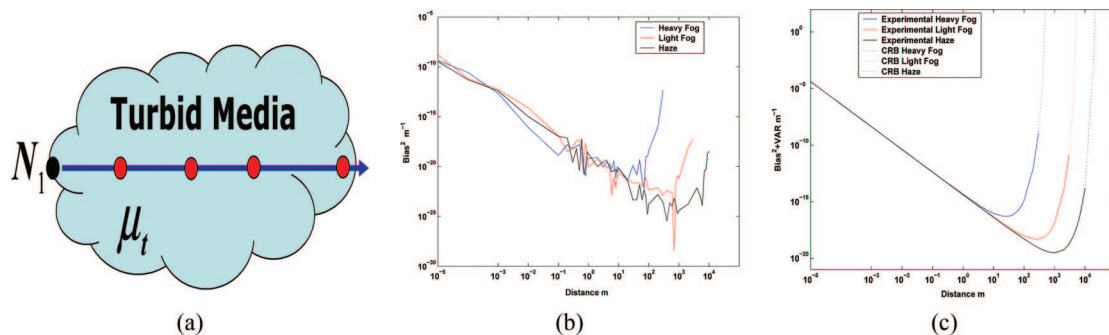
Fig. 1. (Color online) Optimal distance for calibrating the medium extinction factor for heavy fog, light fog, and haze. (a) Experimental setup, where the detector is moved to different locations [marked by lighter (red) dots] inside the turbid medium. (b) Bias of estimation that is calculated over 60,000 Monte Carlo simulations. (c) Summation of squared bias and variance (solid curves) that is dominated by the variance component and perfectly fits the predicted results from CRB formulation (dotted curves) in short distances.

variance is small and can be ignored. Therefore the CRB on the variance can be expressed as

$$Var(\mu_t) > \frac{X_e + I_0 e^{-\mu_t d}}{N I_0^2 d^2 (e^{-\mu_t d})^2}. \tag{4}$$

Aside from theoretical analysis, in practice, this simple closed-form expression of the lower bound to the variance of the estimate can help us design optimal experiments to characterize the optical properties of the medium and the target.

For example, the CRB analysis helps us find the optimal distance between the laser and the detector for estimating the medium extinction factor. Figure 1(a) shows the setup of this numerical experiment, where the black dot represents the position of the laser and the lighter (red) dots represent the possible locations of the detector. The optimal distance minimizing the lower bound on the estimator variance can be easily calculated by differentiation of Eq. (4) with respect to the distance (d). Figure 1(b) shows the estimated bias for this experiment (via 60,000 Monte Carlo experiments), which are small and negligible. In Fig. 1(c), we have plotted the summation of the numerically experimented bias (squared) and the minimum variance (solid curves) and the CRB (dotted curves) predicted from Eq. (4), which perfectly fit the numerically experimented results in shorter distances. These plots suggest that, for calibrating heavy fog, the optimal distance between the laser and the detector is less than 100 m, whereas such a distance for light fog is of the order of a few hundred meters and for haze is of the order of 1 km. Note that the dotted curves (numerically experimented results) in Figs. 1(b)–1(c) are discontinued after certain distances. The reason for such discontinuity is that in long distances, where the signal power is about the same as the noise level, the estimated bias is not negligible and abruptly tends to infinity. Therefore, the proposed CRB formulation (4), depending on the scattering properties of the medium, is only valid up to some distance as plotted in Fig. 1. Practically, this is of no concern, since these distances are away from the optimal calibration distance.

C. Joint Characterization of the Medium and the Target's Optical Properties

A related and more practical problem, namely, characterizing the optical properties of an object located inside an unknown turbid medium, requires two independent sets of experiments. The first set of experiments is performed in the absence of the object (and repeated N_1 times to improve the accuracy) and the second set of experiments is performed in the presence of the presumed object (and repeated N_2 times). Figure 2 illustrates such an imaging scenario, for which we can easily derive the ML estimates of the medium and the object (inclusion) extinction factors as

$$\hat{\mu}_t = \frac{\ln\left(-\dfrac{N_1 I_0}{N_1 X_e - \sum\limits_{k=1}^{N_1} y_k}\right)}{d},$$

$$\hat{\mu}_{t_{inc}} = \frac{d \ln\left(-\dfrac{N_2 I_0}{N_2 X_e - \sum\limits_{k=1}^{N_2} y_k}\right) - (d - d_{inc})\ln\left(-\dfrac{N_1 I_0}{N_1 X_e - \sum\limits_{k=1}^{N_1} y_k}\right)}{d d_{inc}},$$

respectively, where d_{inc} is the thickness of the object.

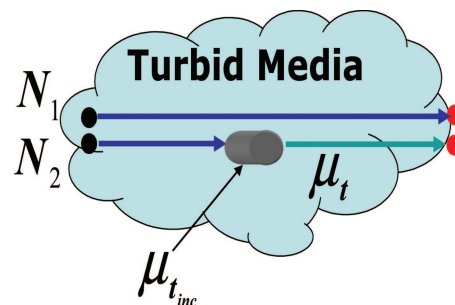The general FIM formulation of Eq. (4) can be exploited for both of these imaging scenarios. In this

Fig. 2. (Color online) Experimental setup for characterizing the optical properties of the medium (μ_t) and a semitransparent object ($\mu_{t_{inc}}$).

case, the CRBs are derived from the inverse of a $[2 \times 2]$ FIM, the diagonal elements of which define the variance bounds:

$$Var(\mu_t) > \frac{X_e + I_0 e^{-\mu_t d}}{N_1 I_0^2 d^2 (e^{-\mu_t d})^2},$$

$$Var(\mu_{tinc}) > \frac{\Omega e^{2\mu_t d - 2\mu_t d_{inc} + 2\mu_{tinc} d_{inc}}}{I_0^2 d^2 N_1 d_{inc}^2 N_2}$$

$$\Omega = (N_1 d^2 X_e + N_1 d^2 e^{-\mu_t d + \mu_t d_{inc} - \mu_{tinc} d_{inc}} I_0$$
$$+ N_2 e^{2\mu_t d_{inc} - 2\mu_{tinc} d_{inc}} d^2 X_e$$
$$+ N_2 e^{-\mu_t d + 2\mu_t d_{inc} - 2\mu_{tinc} d_{inc}} d^2 I_0$$
$$- 2N_2 e^{2\mu_t d_{inc} - 2\mu_{tinc} d_{inc}} d d_{inc} X_e$$
$$- 2N_2 e^{-\mu_t d + 2\mu_t d_{inc} - 2\mu_{tinc} d_{inc}} d d_{inc} I_0$$
$$+ N_2 e^{2\mu_t d_{inc} - 2\mu_{tinc} d_{inc}} d_{inc}^2 X_e$$
$$+ N_2 e^{-\mu_t d + 2\mu_t d_{inc} - 2\mu_{tinc} d_{inc}} d_{inc}^2 I_0). \qquad (5)$$

As an illustrative example, we fixed N_1 and N_2 to 50 each, $X_e = 20$, and assumed that semitransparent objects with extinction factors of $\mu_{t_{inc}} = 0.124$, $\mu_{t_{inc}} = 1.24$, and $\mu_{t_{inc}} = 12.4$ and 1 m thickness are present inside heavy fog. In Fig. 3, we compared the numerically experimented squared bias and variance (via 5000 Monte Carlo simulations) to the CRB limit, assuming that the distance between the laser and the detector are variant between 50 and 300 m. The results basically show that the numerically experimented and CRB values of the medium extinction factor in all cases are indistinguishably close to each other. On the other hand, as the inclusive object becomes more opaque, the theoretic CRB and numerically experimented variance diverge from each other.

3. Performance Analysis of Pixelwise Optimal Detectors

In this section, assuming that the laser, target, and turbid medium are accurately calibrated, we study the performance bounds of optimal detectors in the presence of opaque or semitransparent objects.

A. Detecting Opaque Objects

In this subsection, we study the performance of the Neyman–Pearson (NP) type statistical test [16] for detecting opaque objects hidden in a turbid medium versus distance. In this test, we basically compare the likelihood of the following two scenarios:

- $\mathbb{H}_0$: An opaque object is hidden in the scattering medium, blocking the laser pulse (i.e., measurements contain only noise).
- $\mathbb{H}_1$: No opaque object exists in the propagation line of the laser pulse (i.e., measurements contain noise plus an attenuated laser pulse).

The probability density function of these two scenarios when such tests are repeated N times are given by

$$\mathbb{H}_0 : f(\underline{y}|X_e) = \prod_{k=1}^{N} \frac{e^{-(X_e)}(X_e)^{y_k}}{y_k!},$$

$$\mathbb{H}_1 : f(\underline{y}|X_s + X_e) = \prod_{k=1}^{N} \frac{e^{-(X_e + X_s)}(X_e + X_s)^{y_k}}{y_k!}, \qquad (6)$$

and therefore the NP test is derived by comparing the log-likelihood ratio to a threshold as

$$\log \prod_{k=1}^{N} \left[\frac{\frac{e^{-(X_e + X_s)}(X_e + X_s)^{y_k}}{y_k!}}{\frac{e^{-X_e}(X_e)^{y_k}}{y_k!}} \right] \underset{\mathbb{H}_0}{\overset{\mathbb{H}_1}{\gtrless}} \gamma \Rightarrow \sum_{k=1}^{N} y_k \underset{\mathbb{H}_0}{\overset{\mathbb{H}_1}{\gtrless}} \frac{\log(\gamma) + NX_s}{\log\left(\frac{X_e + X_s}{X_e}\right)} = \gamma'. \qquad (7)$$

Noting that $\sum_{k=1}^{N} y_k$ is yet another Poisson process, the probabilities of false alarm (P_{FA}) and detection (P_D) are computed as

$$P_{FA} = P\left\{ \sum_{k=1}^{N} y_k > \gamma' | \mathbb{H}_0 \right\} = \sum_{k=\gamma'+1}^{\infty} \frac{e^{-NX_e}(NX_e)^k}{k!}$$
$$= 1 - \sum_{k=0}^{\gamma'} \frac{e^{-NX_e}(NX_e)^k}{k!} = 1 - \text{CDF}(NX_e), \qquad (8)$$

$$P_D = P\left\{ \sum_{k=1}^{N} y_k > \gamma' | \mathbb{H}_1 \right\} = \sum_{k=\gamma'+1}^{\infty} \frac{e^{-NX_e - NX_S}(NX_e + NX_S)^k}{k!}$$
$$= 1 - \sum_{k=0}^{\gamma'} \frac{e^{-NX_e - NX_S}(NX_e + NX_S)^k}{k!}$$
$$= 1 - \text{CDF}(NX_e + NX_S), \qquad (9)$$

where CDF is the cumulative distribution function of a Poisson random variable. Note that, in some scientific communities, the false alarm is commonly referred to as a false positive and detection is referred to as a true positive.

Figure 4(a) shows the receiver operating characteristics (ROC) (P_D versus P_{FA}) curves for detecting opaque objects in heavy fog, considering a detector with $X_e = 20$ and a laser power as in Eq. (1). This experiment shows that, by using only ballistic photons, it is possible to reliably detect the existence (or absence) of opaque objects in this scattering medium up to a distance of ~30 MFPs. Figure 4(b) shows the system performance curves by fixing the false alarm rate (P_{FA}) at 0.0015, 0.015, and 0.15 values and plotting the detection rate versus distance (P_D versus d).

B. Detecting Semitransparent Objects

Detection of semitransparent objects is based on differentiating between the following two imaging scenarios:

- $\mathbb{H}_0$: A semitransparent object is hidden in the scattering medium, partially blocking the laser pulse
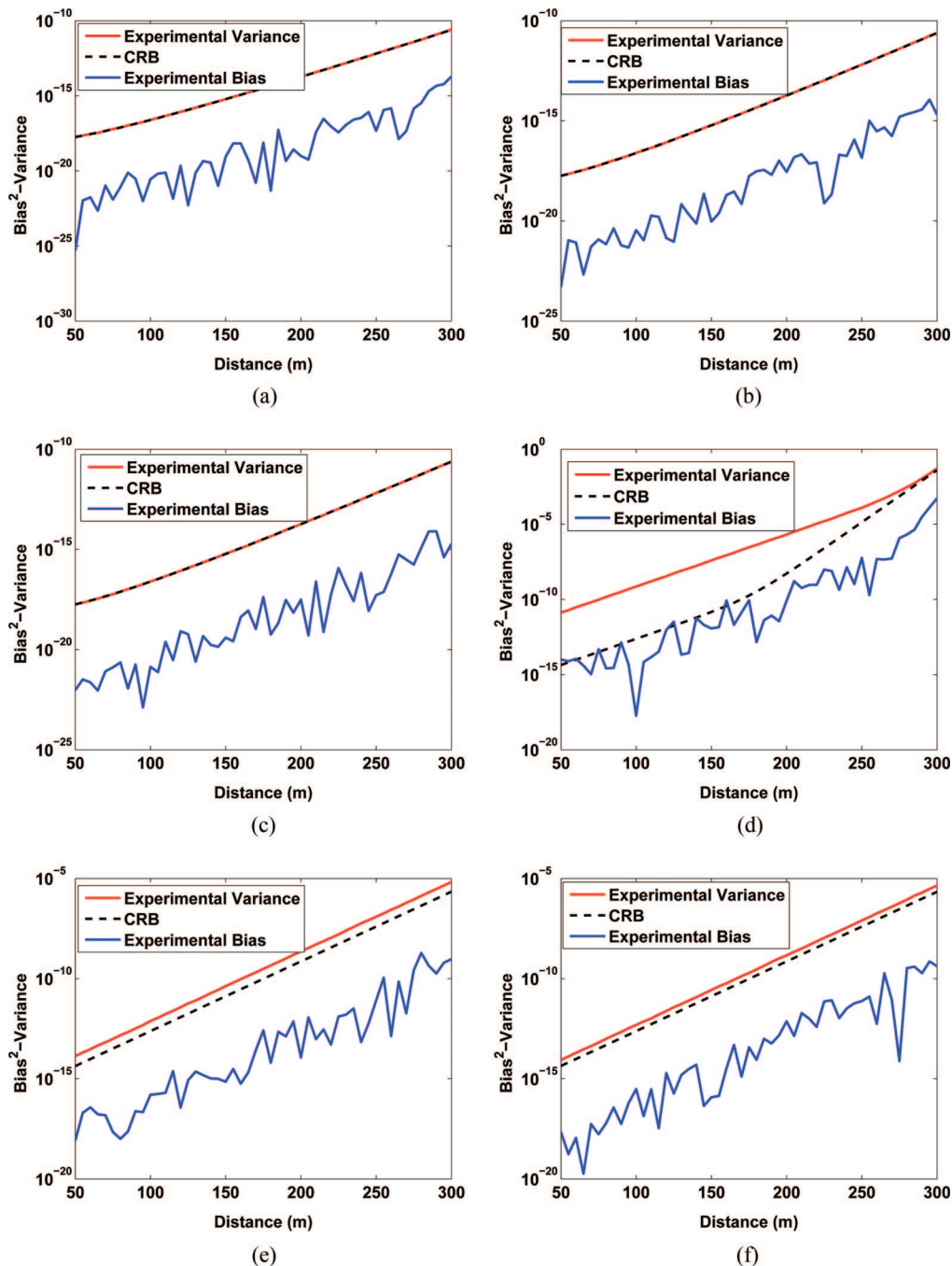
Fig. 3. (Color online) Comparison of the bias and variance from 5000 Monte Carlo simulations (numerically experimented) and the estimated CRB values of the medium and the semitransparent target's optical properties versus distance. The bias, variance, and CRB of the medium extinction factor are compared in (a), (b), and (c). The bias, variance, and CRB of the target's extinction factor are compared in (d), (e), and (f).

(i.e., the measurement is noise plus signal attenuated by both the medium and the target).

- $\mathbb{H}_1$: No semitransparent object exists in the propagation line of the laser pulse in the scattering (i.e., measurement is noise plus signal attenuated by the medium).

The number of ballistic photons in the attenuated signal that travel through both the medium and the semitransparent object is calculated as

$$X_{s_{inc}} = I_0 e^{-\mu_{t_{inc}} d_{inc} - \mu_t (d - d_{inc})},$$

where $\mu_{t_{inc}}$ and d_{inc} are the extinction factor and the thickness of the object, respectively. Based on this model, a NP detection rule is derived as

$$\sum_{k=1}^{N} y_k \overset{\mathbb{H}_1}{\underset{\mathbb{H}_0}{\gtrless}} \frac{\log(\gamma) + N(X_{s_{inc}} - X_s)}{\log\left(\dfrac{X_e + X_{s_{inc}}}{X_e + X_s}\right)} = \gamma'. \qquad (10)$$
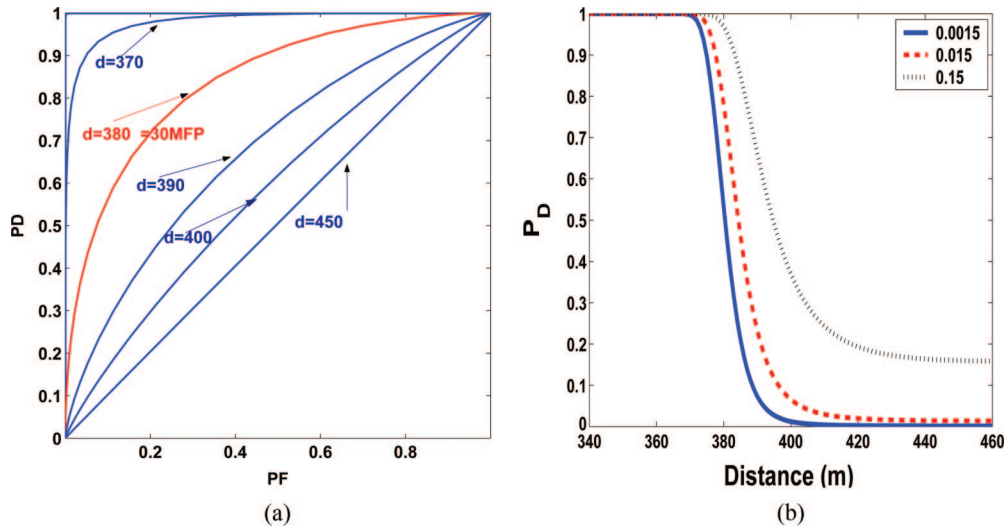
Fig. 4. (Color online) (a) ROC plots at different distances for detecting opaque objects in heavy fog ($\mu_t = 12.5^{-1}\,\mathrm{m}^{-1}$) and $X_e = 20$. (b) By fixing the P_{FA} at different values, the detection rate (P_D) is plotted versus the distance.

The probabilities of false alarm and detection are computed as

$$P_{FA} = P\left\{\sum_{k=1}^{N} y_k > \gamma' \,|\, \mathbb{H}_0\right\} = \sum_{k=\gamma'+1}^{\infty} \frac{e^{-NX_e - NX_s}(NX_e + NX_s)^k}{k!}$$
$$= 1 - \sum_{k=0}^{\gamma'} \frac{e^{-NX_e - NX_s}(NX_e + NX_s)^k}{k!}$$
$$= 1 - \mathrm{CDF}(NX_e + NX_S), \qquad (11)$$

$$P_D = P\left\{\sum_{k=1}^{N} y_k > \gamma' \,|\, \mathbb{H}_1\right\} = \sum_{k=\gamma'+1}^{\infty} \frac{e^{-NX_e - NX_{s_{inc}}}(NX_e + NX_{s_{inc}})^k}{k!}$$
$$= 1 - \sum_{k=0}^{\gamma'} \frac{e^{-NX_e - NX_{s_{inc}}}(NX_e + NX_{s_{inc}})^k}{k!}$$
$$= 1 - \mathrm{CDF}(NX_e + NX_{s_{inc}}). \qquad (12)$$

Figure 5 shows the ROC curves for detecting a semitransparent object in heavy fog. In this experiment using a laser and detector similar to the ones in Subsection 3.A, the distance was fixed at 300 m, which according to Fig. 4 delivers almost perfect detection for opaque objects. Figure 5(b) shows the system performance curves by fixing the false alarm rate (P_{FA}) at 0.00015, 0.0015, and 0.015 values and plotting the detection rate versus the object's extinction factor (P_D versus $\mu_{t_{inc}}$). As expected, this experiment shows that the detection performance deteriorates as the object becomes less opaque.

C. Multipixel GLRT Detection

As explained in Subsection 2.A, in ballistic imaging the field of view is scanned at multiple points to create a 2-D image of the objects in the ROI. In this subsection, we propose an effective algorithm that
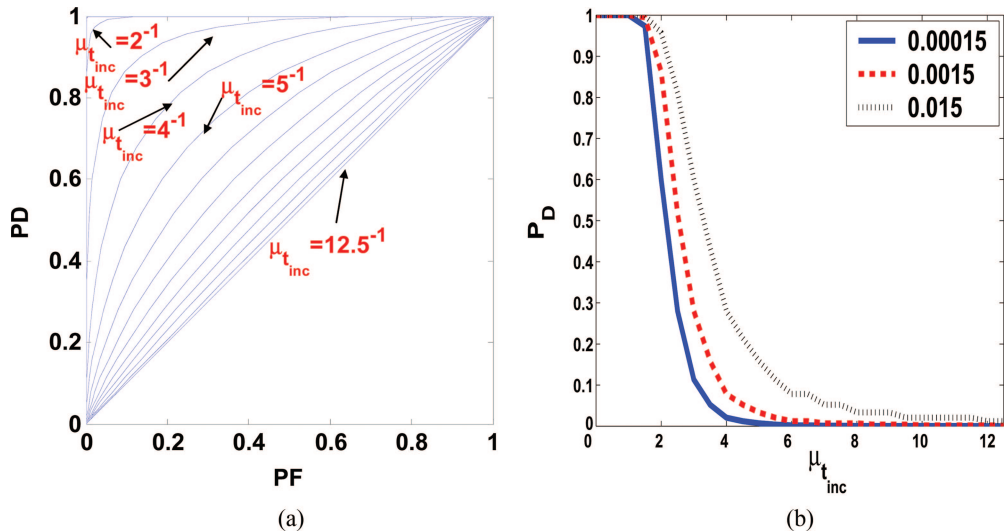

Fig. 5. (Color online) (a) ROC plots for detecting transilluminative objects at 300 m distance in heavy fog ($\mu_t = 12.5^{-1}\,\mathrm{m}$) and $X_e = 20$. (b) By fixing the P_{FA} at different values, detection rate (P_D) is plotted versus the object's transparency ($\mu_{t_{inc}}$).

exploits the spatial correlation of the nearby samples in a multipixel imaging scenario to improve on the performance of the single-pixel optimal detectors developed in the previous section.

The proposed multipixel detection technique generalizes the single-pixel detection techniques and performs tests on superpixels, which are the collective intensities of a set of neighboring pixels in size and shape of the hidden objects. However, since in general the size and shape of the hidden objects is not known *a priori*, we develop a GLRT-based algorithm that simultaneously tests the existence and also estimates the shape and size of the objects hidden in turbid media.

The outline of the proposed GLRT algorithm is illustrated by an example in Fig. 6. First, for a given (fixed) false alarm rate the optimal detectors developed in the previous section are exploited to test the existence or absence of objects at each individual pixel. As an illustrative example, this test is applied to the central pixel (shaded) of Fig. 6(a), where the measured pixel value (0.4) is compared with the NP

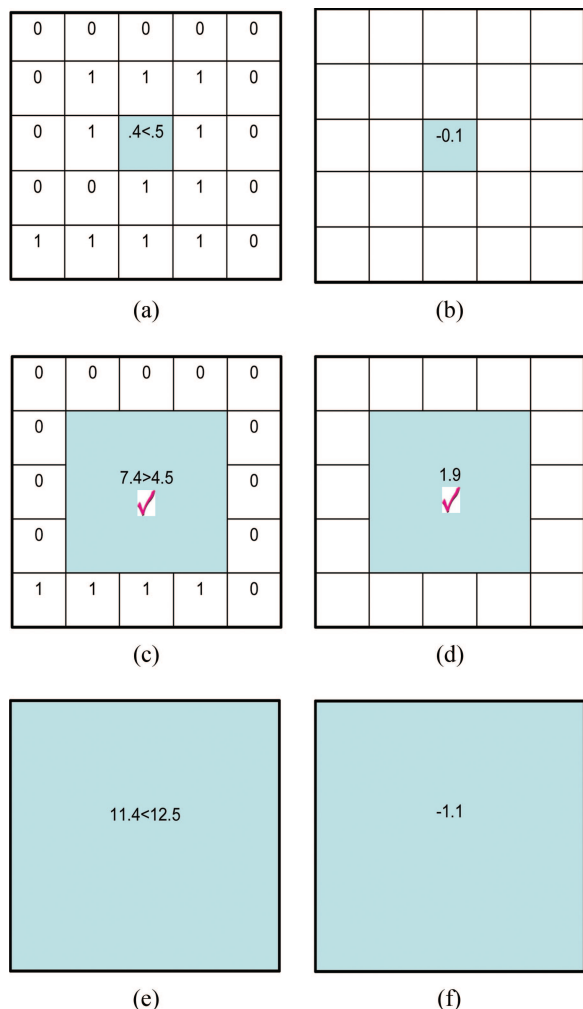(a)   (b)

(c)   (d)

(e)   (f)

Fig. 6. (Color online) Illustrative example showing the outline of the proposed multiscale GLRT algorithm. The check-marked second scale gives the highest confidence value for the central pixel.

test threshold (0.5). Of course, the greater the distance of the measurement from the threshold, the more confident we are in the accuracy of the test result. Next, we integrate the gray-level values of all immediate neighboring pixels, and in effect consider them as one superpixel, as illustrated in Fig. 6(b). Since the false alarm rate is fixed for all scales, the decision threshold is different than the threshold calculated in the previous step, which is recalculated based on the gray-level value of the superpixel. In the next steps, we repeat this process by fixing the false alarm rate and considering larger neighborhoods. The generalized NP test for these steps is formulated as follows:

$$ y_{m,l}{}^{scale} \underset{\mathbb{H}_0}{\overset{\mathbb{H}_1}{\gtrless}} \frac{\log(\gamma^{scale}) + N_{scale}X_s}{\log\left(\dfrac{X_e + X_s}{X_e}\right)}, \qquad (13) $$

where $y_{m,l}{}^{scale}$ is the summation of the pixel values in the $N_{scale} = N(2 \times scale - 1)^2$ pixels neighborhood around the pixel at position $[m, l]$. Our confidence in the decision made on each scale is simply defined as the distance between the summation of measurements in the superpixel and that of the threshold set by the GLRT:

$$ \text{Confidence}_{m,l}{}^{scale} = \left| y_{m,l}{}^{scale} - \frac{\log(\gamma^{scale}) + N_{scale}X_s}{\log\left(\dfrac{X_e + X_s}{X_e}\right)} \right|. \tag{14} $$

Finally, we decide on the presence or absence of the object at a particular pixel based on the test result of the scale that shows the highest confidence value. Note that the optimal scale is not unique for all pixels, as finer scales are more suitable for pixels located on the texture or edge areas, and coarser scales are more suitable for the pixels located in flat areas. The memory requirements of this technique are independent of the maximum scale number, since we only need to keep the original image, the last estimated image, and the corresponding confidence values.

To have a better understanding of the proposed multiscale GLRT technique and its performance, we set up an illustrative controlled imaging scenario. Figure 7(a) shows an ideal (noiseless and deterministic) image of objects of different sizes and shapes. To depict an experiment at the limit distance where the signal of interest is weak, we consider an imaging scenario in which the average number of received ballistic photons for each pixel is one photon. Figure 7(b) shows such Poisson random signals (free of additive noise effect).

Detection of such signals becomes more difficult when we consider the system noise as illustrated in Figs. 8(a) and 9(a), where the Poisson noise variances (mean) are 20 and 40, respectively. Figs. 8(b) and 9(b) are images reconstructed by implementing the point-
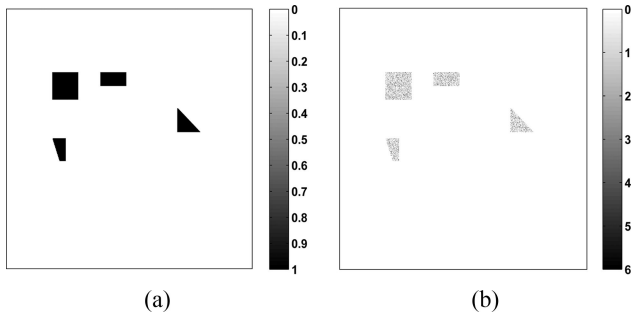
(a)   (b)

Fig. 7. (a) Ideal deterministic and noise-free image of four objects of different sizes and shapes. (b) Corresponding image as a Poissonian noise-free stochastic signal, with $X_s = 1$.

by-point single-pixel detection techniques, considering a false alarm rate of 0.00125, where none of the objects are correctly identified. On the other hand, Figs. 8(c) and 9(c) are the results of exploiting the multiscale GLRT techniques, showing a considerably more accurate detection of such objects. Figures 8(d) and 9(d) illustrate the scale from which each pixel in the final images of Figs. 8(c) and 9(c), respectively, are selected. Note that, as expected, the pixels in the flat area are selected from the coarser scales, whereas the pixels on the edge areas are selected from the finer scales. Figures 8(e) and 9(e), show the confidence in the detection result (14) with respect to the corresponding pixels. These figures show higher confidence levels in the flat and less confidence in the

edge areas. Also, in Fig. 9(e) we see that the area with the lowest confidence is the place where most misclassifications happen. This is good news, since to increase the detection rate, we may opt to do a second (and faster) round of scans, sampling only on these very low-confidence regions. In Figs. 8(f) and 9(f), we plot the misclassification rates at each scale (curve), and compare it with the overall multiscale rate (line). These numerically experimented plots show that the performance of the proposed pixelwise GLRT technique (depending on the noise level) is either very close to [Fig. 8(f)] or even better than [Fig. 9(f)] the best fixed-scale technique. In Figs. 10(a) and 10(b), the performance of the single-pixel detection technique is compared with the multiscale ones via their corresponding ROC curves. Once again, the multiscale technique shows the best or close to the best performance.

4. Diffraction Effects

So far in this paper, all detection tests and related performance analysis were derived based on a simplified model of light propagation that ignores diffraction. Although such approximation works well for many practical applications, it is not a suitable model for detecting or imaging relatively small sized objects. In this section, we present statistical analysis of the resolution limits in ballistic imaging systems by defining the smallest size of resolvable objects in a turbid medium at given false alarm and detection rates.
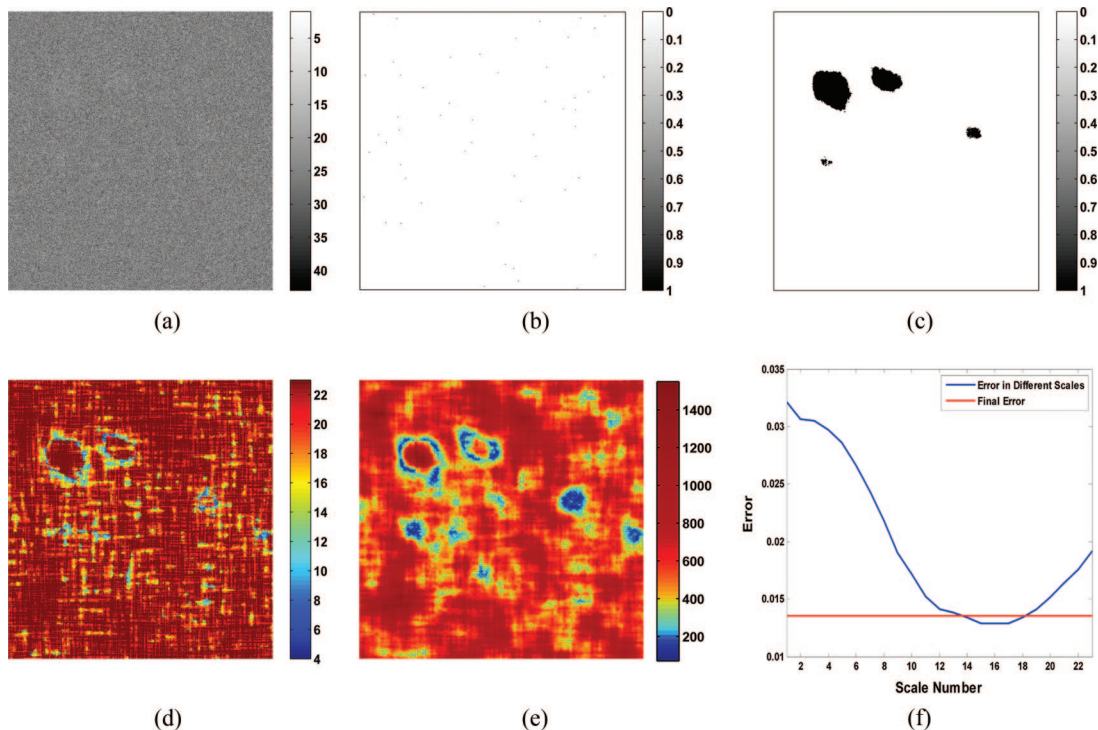

(a)   (b)   (c)

(d)   (e)   (f)

Fig. 8. (Color online) Application of the proposed multiscale GLRT technique for improving the detection rate. (a) Result of adding Poisson noise ($X_e = 20$) to Fig. 7(a). (b) Result of the single-pixel detection. (c) Result of the proposed multiscale detection technique. (d) Image that corresponds to the selected scales for the image shown in (c). (e) Corresponding confidence values. (f) Misclassification probability in different scales.

Fig. 9. (Color online) Application of the proposed multiscale GLRT technique for improving the detection rate. (a) Result of adding Poisson noise ($X_e = 40$) to Fig. 7(a). (b) Result of the single-pixel detection. (c) Result of the proposed multiscale detection technique. (d) Image that corresponds to the selected scales for the image shown in (c). (e) Corresponding confidence values. (f) Misclassification probability in different scales.
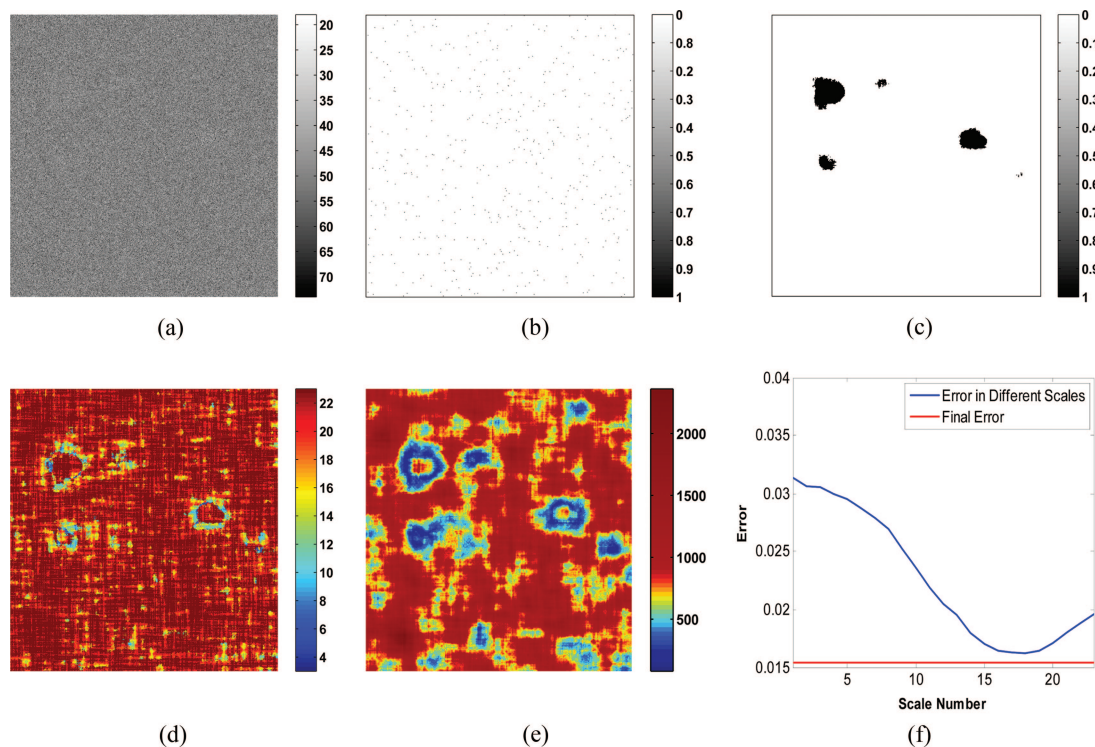
Our study is the continuation of previous work [17], generalized by considering the effects of the turbid medium and ballistic imaging setup.

Figure 11 is a 1-D illustration of the diffraction, which is described as "any deviation of light rays from rectilinear paths which can not be interpreted as reflection or refraction" [18]. In this figure, the dashed (red) line represents the case in which light propagates in a straight line creating a sharp-edged

shadow of a hidden opaque object at the detector. The solid (green) curve, on the other hand, illustrates a more realistic case in which the object's shadow appears blurry at the detector as a result of diffraction.

The blur induced by diffraction can be calculated from the Helmholtz–Kirchhoff wave propagation equations [19]. However, for the experimental setups that are of most interest to us with respect to the scope of this paper, the diffraction effect can be taken
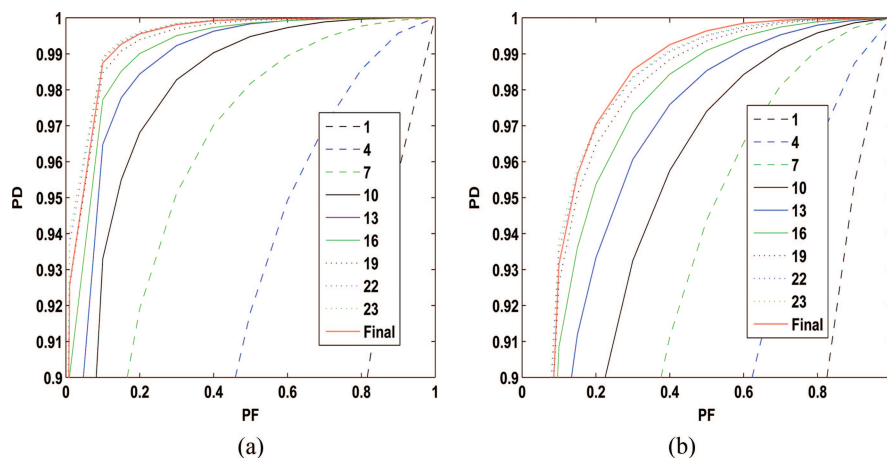

Fig. 10. (Color online) Application of the proposed multiscale GLRT technique for enhancing the detection rate. ROC plots for the proposed multiscale detection scenario in the imaging scenarios of Figs. 8 and 9 (with 25 Monte Carlo experiments) are shown in (a) and (b), respectively. The numerical labels "1, 4, . . . , 23" correspond to the scale at which detection tests are performed, and the plot labeled "Final" represents the performance of the proposed multiscale (fused) technique.
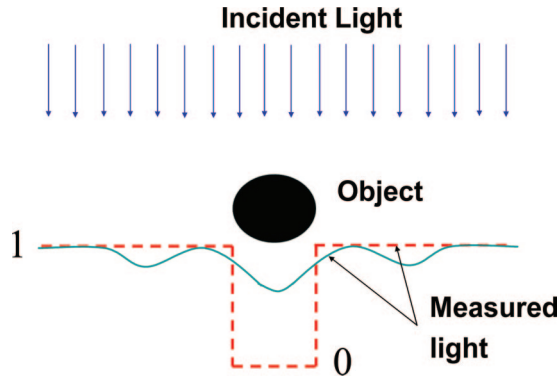
Fig. 11. (Color online) Shadow of an opaque object illuminated by a homogeneous widespread light beam. The dashed (red) curve represents the intensity of the measured light ignoring diffraction. The solid (green) curve represents the diffraction-induced PSF.

into account by convolving the expected signal value with an appropriate point-spread function (PSF) that describes the blurring effect of an object estimated from the Fraunhofer approximation. For a circular opaque object, such a PSF is given by

$$H(r) = 1 - \frac{2k\rho^2}{z} \sin \frac{kr^2}{2z} \frac{J_1\left(\frac{k\rho r}{z}\right)}{\frac{k\rho r}{z}} + \frac{k^2\rho^4}{z^2}\left[\frac{J_1\left(\frac{k\rho r}{z}\right)}{\frac{k\rho r}{z}}\right]^2,$$

(15)

where $k = 2\pi/\Lambda$ is the wavenumber, $J_1(\ )$ is the order 1 Bessel function of the first kind, ρ is the radius of the opaque object, r is the radius coordinate in the detector plane, and z is the distance between the object and the detector [20]. Note that the Fraunhofer approximation is only valid when $z \gg 4\rho^2/\Lambda$, and therefore in this paper we only consider far-field imaging scenarios. Ignoring the effect of a turbid medium and considering homogeneous illumination with intensity I' at the object plane, the radially symmetric intensity of the detected signal at the radius coordinate r is simply given by $I = I'H(r)$. Figure 12(a) shows the diffraction pattern of a circular opaque object with a distance of $z = 100$ m from the detector, illuminated by unit-intensity ($I' = 1$) light with 800 nm wavelength.

In the imaging scenarios considered in this paper, the detected signal is further attenuated by the turbid medium, and the expected value of the signal intensity at the radius coordinate r and distance z from the object plane can be approximated as

$$I = I' \exp(-\mu_t z)H(r),$$

where we have ignored the fact that due to diffraction some parts of the wavefront travel slightly longer distances. Note that in practice, due to the far-field imaging assumption, such variance in attenuation is small. This effect is shown in Fig. 12(b), where the path lengths L_1 and L_2 are practically equal if the distance between the opaque object and the detector (z) is significantly larger than the PSF spread. The detection problem associated with the signal model defined above is described in the following two imaging scenarios:

- $\mathbb{H}_0$: An opaque object of unknown but small size ($\rho > 0$) is hidden in the scattering medium, blocking and blurring the laser pulse (i.e., measurements contain noise plus attenuated and blurred laser pulse).
- $\mathbb{H}_1$: No opaque object exists ($\rho = 0$) in the propagation line of the laser pulse (i.e., measurements contain noise plus attenuated laser pulse).

The above GLRT detector is different than the NP detectors of Section 3 since the size of the object is now assumed to be unknown. Following Eq. (2), the expected value of the intensity in the absence of the object ($\mathbb{H}_1$) is given by

$$I(k, 0) = I_0 e^{-\mu_t d} + X_e.$$
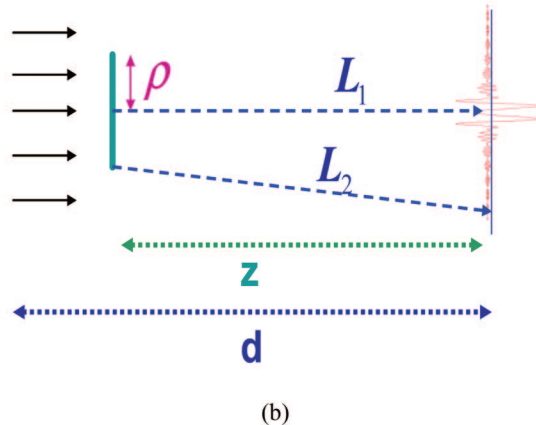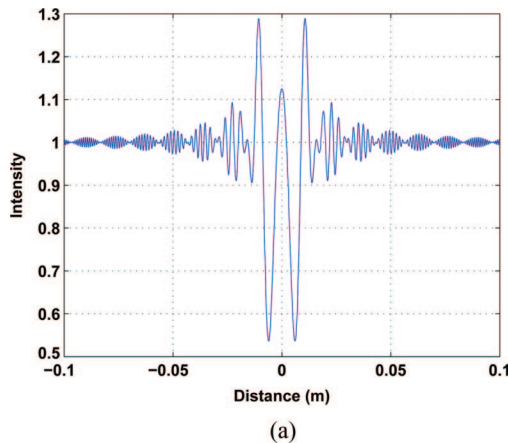

Fig. 12. (Color online) (a) 1-D slice of the diffraction pattern of a circular object of radius 3 mm at 100 m distance and 800 nm wavelength. (b) 1-D slice of the imaging scenario, where z is the distance between the opaque circular object (radius ρ) and the detector. d is the distance between the laser and the detector. The pass length $L_1 \simeq L_2$ when z is very long.

The intensity of the signal in the presence of the object ($\mathbb{H}_0$) is estimated as

$$I(k,\ \hat{\rho}) = I_0 e^{-\mu_t d} H(r_k) + X_e, \qquad (16)$$

where $\hat{\rho}$ is the estimate of the opaque object's radius and r_k is the radial distance of the kth pixel from the axes passing through the center of the object. The unknown radius of the opaque object is estimated as

$$\hat{\rho} = \arg\max_{\rho} \prod_{k=1}^{N} \frac{e^{-I(k,\rho)}[I(k,\ \rho)]^{y_k}}{y_k!}. \qquad (17)$$

The above ML estimate of the radius is solved by numerical optimization, where we discretize ρ over an assumed range of values $\rho[g]$, $g = 1, \ldots, G$, and compute the cost function,

$$\varrho[g] = \sum_{k=1}^{N} y_k \log\{I(k,\ \rho[g])\} - I(k,\ \rho[g]). \qquad (18)$$

The value of g for which $\varrho[g]$ takes on the largest value is g_{max}, and finally the GLRT detection statistics is given by

$$\sum_{k=1}^{N} y_k \log\left\{\frac{I(k,\ \rho[g_{max}])}{I(k,\ 0)}\right\} \gtrless \gamma. \qquad (19)$$

As an illustrative example, by fixing the false alarm rate at $P_{FA} = 0.1$, the noise level at $X_e = 20$, and assuming a large detector that detects all the light, regardless of the distance or size of the object, we used the above GLRT framework to search for the smallest detectable object size at different distances and detection rates in heavy fog ($\mu_t = 12.5^{-1}\ \mathrm{m}^{-1}$). Figure 13 illustrates the result of this experiment, where as expected the size of detectable objects first rises as the distance increases.
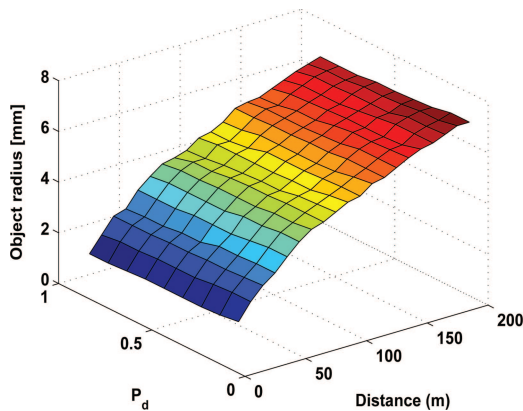

Fig. 13. (Color online) Detection rate versus the (unknown) opaque circular target's radius and the distance between the laser and the detector considering the diffraction limit with $P_{FA} = 0.1$ and $X_e = 20$ in heavy fog ($\mu_t = 12.5^{-1}\ \mathrm{m}^{-1}$).
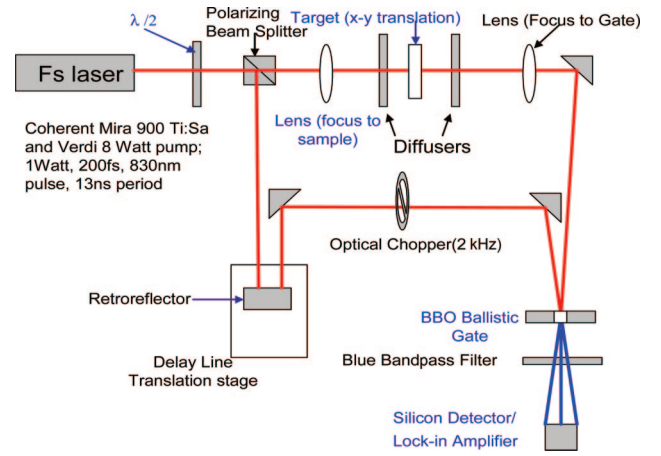
Fig. 14. (Color online) Laser setup at the Ballistic Imaging Laboratory at the University of California, Santa Cruz.

5.   Laboratory Setup and Experiments

A.   Conventional Ballistic Imaging Experimentation

In our experiments, to generate ultrashort optical pulses we used a Coherent Mira 900 Ti:sapphire tunable femtosecond laser pumped by an 8 W pump (Verdi V-8). At the output this laser generates an average power of ~1 W with pulses of 200 fs duration, 13 ns repetition period, and 830 nm wavelength.

As shown in Fig. 14, each laser pulse passes through a $\lambda/2$ plate and is incident on a polarizing beam splitter that divides the pulse into two copies, one used for triggering the ultrafast time gate while the other passes through the scattering medium (which is modeled by two sets of solid diffusers located in front and back of the target). Rotation of the $\lambda/2$ plate determines the power ratio between the two pulses, and we experimentally determined that the best results are achieved in a near 50%/50% splitting ratio. After passing through the diffusers and target, the ballistic photons are incident on the gate at exactly the same time as the triggering pulse and pass through the ultrafast time gate, where due to the phase and polarization difference the scattered photons are rejected. In practice, the triggering pulse timing is controlled by a delay line, which increases or decreases the optical path length, using a computer-controlled translation stage.

The ultrafast time gate used is a nonlinear crystal, β-barium borate (BBO) [21], which utilizes a two-photon process such that the gating time can be as short as the laser pulse width. Additionally, by slightly changing the incident angles of the two pulses on the nonlinear crystal, the time-gated result can be spatially separated from the background signal, greatly increasing the signal-to-noise ratio. This effect is sometimes referred to as background-free cross correlation [22]. The energy of the ballistic photons are then measured by a silicon detector and a lock-in amplifier. The entire setup implemented at the ultrafast imaging laboratory at the University of
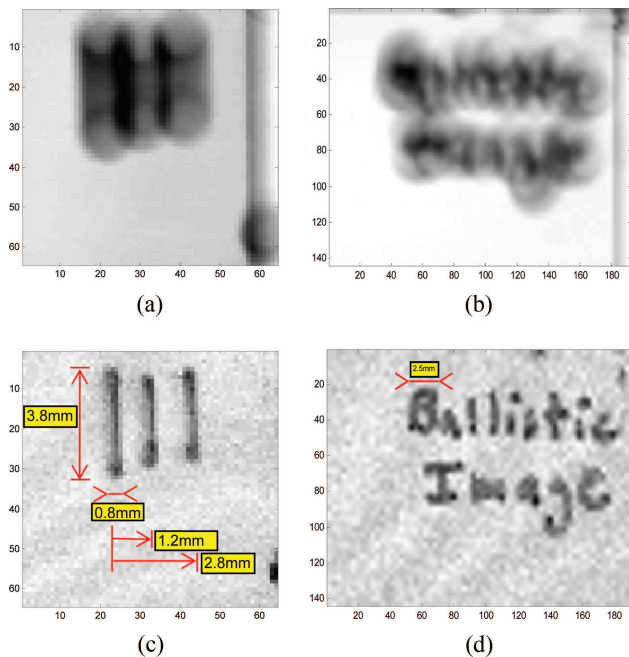
Fig. 15. (Color online) Comparison of diffusive and ballistic imaging. (a), (b) Two diffusive (no time gating) scans. (c), (d) Two corresponding ballistic (time-gated) scans through five solid ground glass diffusers.

California, Santa Cruz, is controlled using LabView and a general purpose interface bus (GPIB) bus.

Figure 15 shows the results of two imaging experiments where the objective is to read the text written on transparency sheets by a ballpoint pen, surrounded by a total of five solid glass (Thorlabs ground glass, DG10-220) diffusers. The thickness of these diffusers is 2 mm each, with the MFP of 0.73 mm (7.3 MFP total). We also note that the dynamic range of our system is approximately 100 dB. Figures 15(a) and 15(b) show the result of scans in the absence and Figs. 15(c) and 15(d) show the result of scans in the presence of the ballistic time gate, without any postprocessing. To acquire the nongated images, the gate was removed and the detector repositioned. Note that Figs. 15(a) and 15(c) illustrate raw data (without any postprocessing) from the imaging system, whereas the results shown in Figs. 15(b) and 15(d) are each upsampled by a factor of 3 via the bicubic interpolation technique. These results show that, although ballistic images are noisier than the non-time-gated (diffusive) ones, they are preferable since they are virtually blur free.

B. Adaptive Sampling Experimentation

As explained in the previous sections, in ballistic imaging, 2-D images of the objects in the scattering media are created by a relatively time-consuming point-by-point scanning scheme in which the field of view (FOV) is sampled at regularly spaced locations. For instance, in a typical laboratory setup with a mechanical translation stage (Fig. 14), creating a 256×256 image (i.e., sampling at 65,536 points)

takes about 4 h, which might be prohibitively long for many real-world applications. Although such excessive time can be reduced if the mechanical translation stage is replaced by a more expensive optical one, faster scans are always desired, and moreover, for many applications, the total number of pulses delivered in a given time period is limited by the average delivered energy due to health concerns.

By making some simplifying assumptions about the objects of interest (e.g., piecewise constancy), irregular scan strategies, such as sampling sparsely in the low-frequency areas and densely in the high-frequency (edge or textured) areas, are shown to be useful in reducing the imaging time. Recently, two related techniques, namely, compressive sensing [23,24] and active learning [25] (adaptive sampling) were proposed to reduce the number of samples required to achieve certain reconstruction accuracy with respect to the regular (passive) scanning technique. We note that it is the sparsity of the signal of interest (in a given overcomplete dictionary of bases) that enables such techniques to gather sufficient information to achieve optimal (if not perfect) reconstruction in the presence of noise, even when the sampling rate is lower than the Nyquist rate [26]. In the compressive sensing technique, random projections of the signal of interest onto an overcomplete set of basis functions are sequentially recorded. Such random projections in practical optical imaging scenarios can be implemented by passing a wide-field beam through binary masks with a random pattern [in practice, a digital micromirror device can be used to generate the random basis patterns [27]]. Unfortunately, in the ballistic imaging setup, creating a wide-field beam is not easy. Moreover, diffraction limits the resolution of the binary mask and therefore implementing a compressive-sensing-based ballistic imaging system is not trivial. On the other hand, in the following we show that adaptive sampling techniques can be readily exploited for ballistic imaging purposes.

We have implemented adaptive sampling as a two-step process [28]. In the first step, we regularly sample the FOV space at $N/2$ points, where N is the total number of samples that we plan to collect. We use these $N/2$ measurements to create a pilot estimate of the unknown FOV. In the next step, the remainder of the $N/2$ points are used to sample the FOV on the edge areas of the estimated image. It can be shown that the decay rate of the mean square error for piecewise constant images is $O(N^{-1/2})$ and $O(N^{-1})$ for the passive and active sampling techniques, respectively [28].

We also note that active learning relies on accurate adaptive image reconstruction algorithms to reconstruct the unknown images from the irregular samples of the FOV. In our implementation, we used an image reconstruction method based on maximum *a posteriori* (MAP) with bilateral total variation prior (regularizer) [29]. The general formulation of this

technique is presented as follows:

$$\underline{\hat{X}}(t) = \arg\min_{\underline{X}(t)}\left[\|A(\underline{X}-\underline{\hat{Z}})\|_2^2 + \psi\sum_{l,m=-P}^{P}\alpha^{|m|+|l|}\|\underline{X} - S_x^l S_y^m \underline{X}\|_1\right], \tag{20}$$

where X of size $[ML \times 1]$ is a vector representing the reconstructed image of size $[M \times L]$ after lexicographic ordering, and Z of size $[ML \times 1]$ is a vector that stores the $N < ML$ measurements. In this vector, the elements that correspond to those pixels in X for which no measurement is available are filled with zeros. The matrices S_x^l and S_y^m are the operators corresponding to shifting the image represented by X by l pixels in the horizontal direction and m pixels in the vertical direction, respectively. The scalar weight, $0 < \alpha \le 1$, is applied to give a spatially decaying effect to the summation of the regularization terms, which in effect represent derivatives across multiple resolution scales. Matrix A of size $[ML \times ML]$ is a diagonal matrix whose values are chosen in relation to our confidence in the measurements that contributed to make each element of $\hat{Z}$ (diagonal elements corresponding to pixels for which no measurement is available are replaced with zeros). The regularization parameter, ψ, is a scalar for properly weighting the first term (data fidelity cost) against the second term (regularization cost).

To validate the applicability of this adaptive sampling and reconstruction technique versus the common passive sampling technique, we performed the following experiment. A metal washer was imaged through a ground glass diffuser (Thorlabs ground glass, DG10-220) via the ballistic imaging setup of Fig. 14. Figure 16(a) shows the result of scanning the medium on a 128 × 128 (16,384 total) regularly sampled grid. Figure 16(b) shows the same image sampled on a regular 32 × 32 (1024) grid and then upsampled by the bicubic interpolation method to a dense 256 × 256 grid. The alternative sampling strategy was performed by exploiting the same experimental setup (distance, turbid medium, target), where a total of 950 irregularly sampled data points were collected in the said two-step adaptive process. Figure 16(c) shows the result of such an adaptive sampling scheme after upsampling to the 256 × 256 grid by the proposed adaptive MAP-based interpolation method. The spatial position of the 984 adaptive samples are marked as white dots on a 256 × 256 grid in Fig. 16(d), which, as expected, is considerably denser on the edge areas.

6. Conclusion and Future Work

In this paper, we have studied a technique for capturing high-resolution images through turbid media. This approach was based on separating the unscattered (ballistic) photons from the diffused ones by implementing an ultrafast time-gating system. The novelty of this paper is in combining the recent advances in optical science with the novel image processing and statistical signal processing techniques. We studied the resolution limits of such a system that were close to diffraction (Rayleigh) limits for longer distances. We derived the fundamental limits on the accuracy of the estimated extinction parameters of an unknown turbid medium and the targets inside it. This study also guided us toward the most efficient experiments (with respect to both time and accuracy) for calibrating the model parameters of the unknown turbid medium as well as the optical properties of the target (which can be used to identify and categorize it). Our results showed that for a medium of practical interest, namely, heavy fog, optical parameters can be estimated with high accuracy. We used the said model to derive optimal statistical tests for detecting objects hidden in turbid media. Performance analysis was carried out by computing ROC curves for the proposed optimal tests, showing that, by considering only the ballistic photons, we are able to detect opaque objects hidden in heavy fog in the range of approximately 380 m (i.e., 30 MFPs). The detection rate of the semitransparent objects is shown to be slightly less than this distance. Also, real experiments attested to the fact that ballistic imaging, especially in longer distances, is difficult, and therefore we developed a multiscale GLRT algorithm to improve the detection rate in such scenarios. To reduce
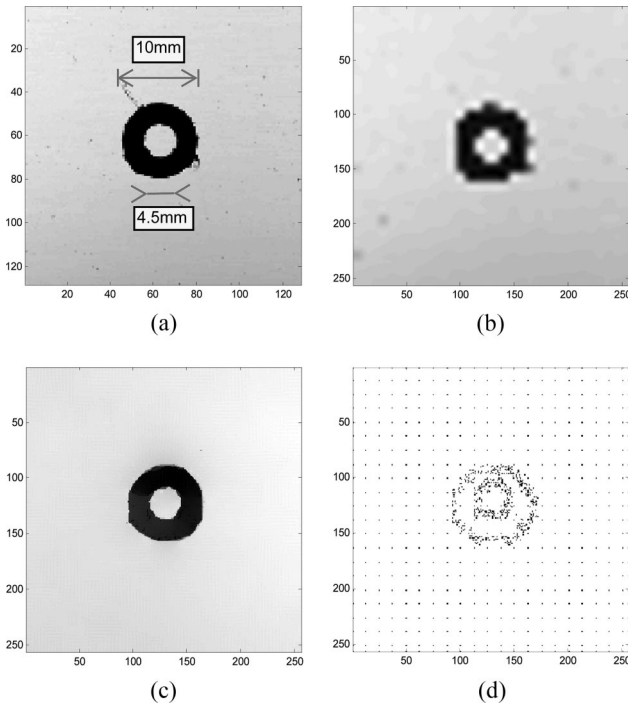
Fig. 16. Comparison of passive and active imaging. (a) Result of scanning the turbid medium on a regular 128 × 128 grid (16,384 dense passive sampling). (b) Result of scanning the turbid medium on a regular 32 × 32 grid (1024 sparse passive sampling) followed by interpolation via bicubic interpolation to reconstruct the image on a 256 × 256 grid. (c) Result of scanning the turbid medium on an irregular grid (984 sparse adaptive sampling) followed by interpolation via adaptive interpolation to reconstruct the image on a 256 × 256 grid. (d) Distribution of the 984 irregular samples.

the data acquisition time that is essential for many real-world applications, we implemented an adaptive sampling scheme that significantly reduced the data acquisition time.

As for future work, one may exploit temporal, spatial, and wavelength diversity and coding for ballistic imaging. We can study the array imaging framework where multiple emitters will transmit coordinated pulses of light, and for their part, a collection of photon-detecting elements will gather the received data and compute a resultant image. Furthermore, there is the possibility of analyzing various ways of coding these pulses (e.g., transmitting sequences of pulses as is done in ultrawideband communications).

Moreover, we believe that detection techniques that exploit all ballistic, snake, and diffused photons [30] (what we term holistic imaging and detection) enable detection of larger objects at significantly longer range. More theoretical and experimental work needs to be done to design a (near) optimal yet practical solution to this important problem.

Appendix A: Decision-Theoretic Resolution Bounds

As explained throughout this paper, the diffraction-limited resolution of ballistic imaging systems [e.g., Figs. 15(c) and (d)] makes them appealing for imaging in relatively short distances. However, in relatively long distances the ballistic signal is too weak and we are bound to rely on the blurry but higher signal-to-noise ratio (SNR) images of conventional imaging systems [e.g., Figs. 15(a) and (b)]. In this Appendix, we adapt a decision-theoretic approach to the resolution bounds and search for the critical distance after which the ballistic imaging systems are of no practical advantage compared with the conventional imaging systems.

1. Ballistic Imaging—Single Point

The problem of determining whether an object lies along the line of sight can be cast as a statistical hypothesis test as follows. Given a received photon count X at the sensor, one must choose between two possible situations. The first situation is that no occluding object exists in the path between the laser and the sensor ($\mathbb{H}_0$). The alternative is that there is an occluding object along the line of sight between the laser and the detector ($\mathbb{H}_1$). Semitransparent objects can be considered to be significantly more scattering than the medium [31], and therefore the detector will collect an attenuated number of ballistic photons (compared with $\mathbb{H}_0$) along with the noise photons.

Following the notation of Subsection 3.B, we define the number of noise photons that will arrive at the detector as $\mathscr{P}(NX_e)$, where $X \sim \mathscr{P}(\chi)$ is a Poisson-distributed random variable with mean χ. Then, the hypothesis test is given by the null hypothesis defined as $\mathbb{H}_0 : X \sim \mathscr{P}(NX_e + NX_s)$ and the alternate hypothesis (object exists) defined as $\mathbb{H}_1 : X \sim \mathscr{P}(NX_e + NX_{s_{inc}})$. As the mean of the Poisson distribution grows, the probability distribution tends to a Gaussian, e.g., averaging many repeated Poissonian trials (i.e., N large) results in a Gaussian-distributed sta-

tistic. Using the Anscombe transformation [31], we obtain the following relationship:

$$X \sim \mathscr{P}(\chi) \Rightarrow 2\sqrt{X + \frac{3}{8}} \sim \mathscr{N}(2\sqrt{\chi},\ 1),$$

where $\mathscr{N}(\zeta, \sigma^2)$ represents Gaussian distribution with mean ζ and variance σ^2. Defining a new variable representing the Anscombe-transformed statistic $X' = 2\sqrt{X + 3/8}$ the hypothesis test becomes

$$\mathbb{H}_0 : X' \sim \mathscr{N}\big(2\sqrt{NX_e + NX_s},\ 1\big),$$

$$\mathbb{H}_1 : X' \sim \mathscr{N}\big(2\sqrt{NX_e + NX_{s_{inc}}},\ 1\big). \quad \text{(A1)}$$

The decision test is now defined as $(X' \lesseqgtr_{\mathbb{H}_0}^{\mathbb{H}_1} \gamma')$, where a user-specified false alarm rate (P_{FA}) determines the value of the threshold (γ') such that $P(X' < \gamma' | \mathbb{H}_0) \le P_{FA}$.

2. Ballistic Imaging—K Points

The problem now is modified to describe an imaging scenario of scanning the FOV at a fixed square array of ($\sqrt{K} \times \sqrt{K}$) points. This results in a multiple hypothesis testing problem (K tests), where for large K it puts a lower bound on the SNR of the observation. To boost the SNR, one could use spatial aggregation by averaging over a number of observation points. This modifies the problem to averaging neighborhoods of points in an area measuring $\sqrt{W} \times \sqrt{W}$, $W < K$, effectively reducing the spatial resolution of the detection map (image). By decreasing the spatial resolution, this also decreases the variance at each point, modifying the decision test to

$$\mathbb{H}_0 : X' \sim \mathscr{N}\left(2\sqrt{NX_e + NX_s},\ \frac{1}{W}\right),$$

$$\mathbb{H}_1 : X' \sim \mathscr{N}\left(2\sqrt{NX_e + NX_{s_{inc}}},\ \frac{1}{W}\right). \quad \text{(A2)}$$

This test is under the assumption that the averaging window will contain either no occluder points or all occluder points. In reality, the averaging filter will result in an observed point, $X'' \sim \mathscr{N}(\varphi E[X' | \mathbb{H}_0] + (1 - \varphi)E[X' | \mathbb{H}_1], 1/W)$, where φ is the fraction of the window containing nonoccluders, and E is the expected value operator. Our goal is to find the lower bound on the value of W that will guarantee an overall false alarm rate of less than P_{FA}, and we only consider the ideal case (all occluders or nonoccluders) in our calculations in order to obtain closed-form solutions.

The Bonferroni correction approach is a conservative method of controlling the false alarm rate for a detection problem under multiple independent and identically distributed tests [33]. The correction adjusts the threshold for each individual test in order to satisfy a lower (per test) false alarm rate

value (P_{FA}/K) such that each of the fixed number K points in the array (and W-point averaging filter) satisfies $[P(X < \gamma' | \mathbb{H}_0) \leq P_{FA}/K]$. With $\Phi(x)$ as the cumulative distribution function of the $\mathcal{N}(0, 1)$ density at the point x, this results in $[\gamma' \leq (1/\sqrt{W})\Phi^{-1}(P_{FA}/K) + 2\sqrt{NX_e + NX_s}]$. To give a satisfactory observation, we also bound the miss probability for detecting a ballistic photon by the same modified value (P_{FA}/K) such that $[P(X > \gamma' | \mathbb{H}_1) \leq P_{FA}/K]$. Using the miss bounds, we determine the lower bound on the necessary averaging window size (W) to image a fixed K-point array as

$$W \geq \left[\frac{1}{2} \frac{\Phi^{-1}\left(1 - \dfrac{P_{FA}}{K}\right) - \Phi^{-1}\left(\dfrac{P_{FA}}{K}\right)}{\sqrt{NX_e + NX_s} - \sqrt{NX_e + NX_{s_{inc}}}} \right]^2. \quad (A3)$$

The minimum width of the occluding object (w_b) that can be reliably resolved for a given parameterized turbid medium can now be derived. Using the lower bound for W found in Eq. (A3), we can solve for the lower bound on the width using $w_b = \sqrt{(\text{FOV} \times W)/K}$.

3. Conventional Imaging Analysis

In the conventional imaging regime, there is no time-gating mechanism and all the photons that reach the detector over a long acquisition time will be observed [acquisition time $\gg (d/c)$ = direct line-of-sight flight time]. Therefore, a large number of photons sent through the medium will be collected by the detector. A problem occurs here, too—although the SNR is high due to the large number of photons, the average number of scattering events on each photon collected will
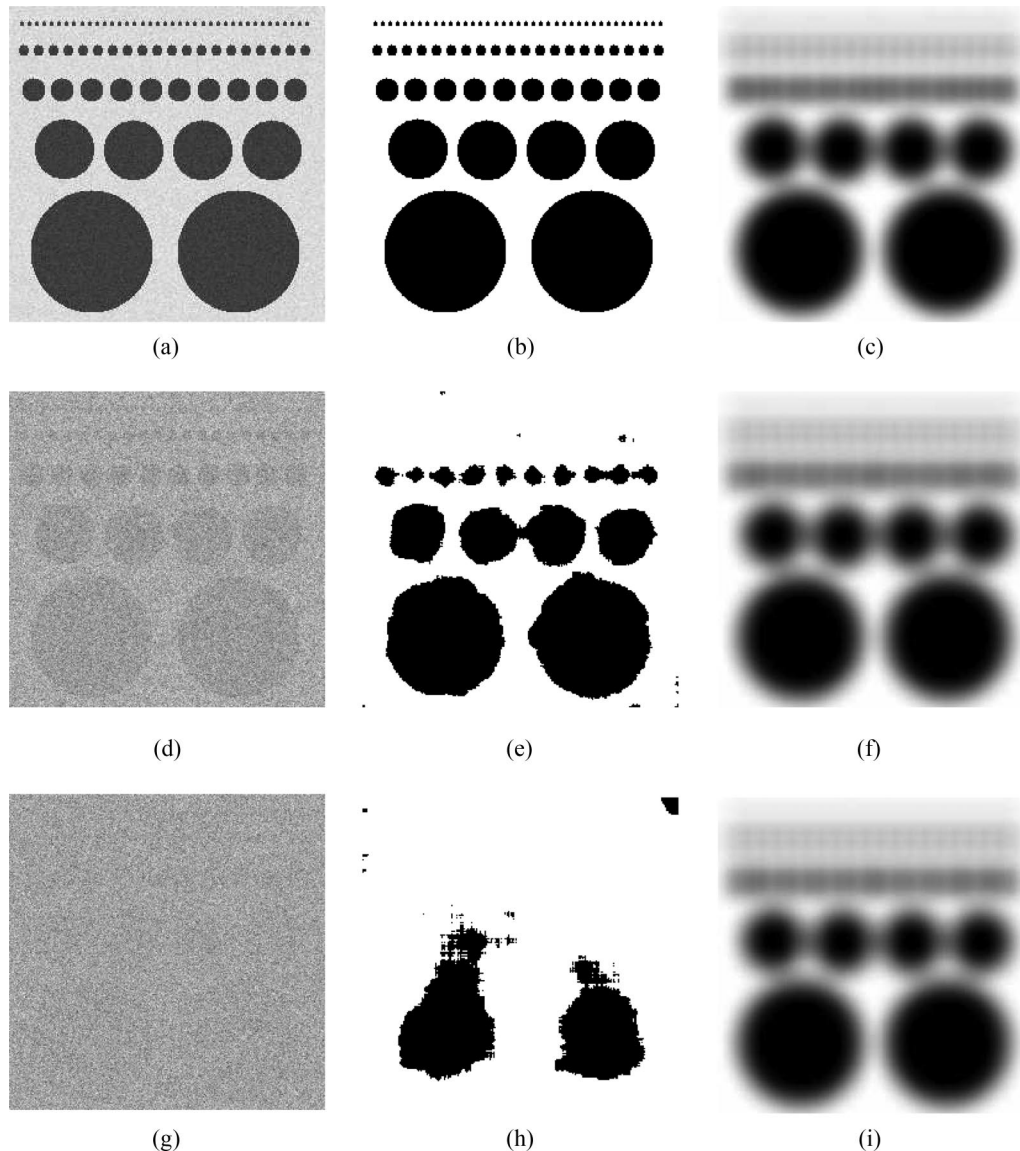
Fig. 17. Simulation experiments with FOV = 50 m × 50 m, $d_{inc} = 0.3$ m, and $\mu_t = 12.5^{-1}$ m^{-1}. (a)–(c) Ballistic, Bonferroni, and conventional observations at $d = 350$ m, respectively. (d)–(f) Ballistic, Bonferroni, and conventional observations at $d = 400$ m, respectively. (g)–(i) Ballistic, Bonferroni, and conventional observations at the critical distane $d = d_{critical} = 417$ m, respectively.

also be high. As the number of scattering events increases for a photon, the spatial resolution of the occluding object will degrade. The lack of spatial information results in a blurred observation. Using random-walk theory [34,35], it is possible to solve for the minimum width of an occluding object that is reliably resolved using a conventional imaging system. The width [36] is found using the photon mean time of flight $\langle \Delta t \rangle$, which can be numerically computed as a function of the parameters of the medium (μ_s, μ_a). The modified minimum full width at half-maximum (FWHM) is equal to $w_{conv} = 0.94(\langle \Delta t \rangle c / \mu_s)^{1/2}$.

4. Optimal Resolution Trade-Offs

Ideally, one should choose the imaging system (ballistic or conventional) that reliably resolves the smallest possible object [$w = \min(w_{conv}, w_b)$]. The decision test using the minimum resolvable sizes derived above becomes

$$
w_{conv} \underset{\text{ballistic}}{\overset{\text{conventional}}{\lessgtr}} w_b \Rightarrow 0.94\left(\frac{\langle \Delta t \rangle c}{\mu_s}\right)^{1/2} \underset{\text{ballistic}}{\overset{\text{conventional}}{\lessgtr}} \sqrt{\frac{\text{FOV} \times W}{K}}. \tag{A4}
$$

Using the lower bound of W from Eq. (A3), one can solve for the critical distance ($d = d_{critical}$), the maximum distance at which ballistic still offers superior resolution relative to conventional imaging.

As an illustrative example, we considered a ballistic scanning experiment at ($K = 256^2$) points, imaging a 50 m × 50 m FOV. The occluding objects were assumed to be circular of diameter 1.0, 2.0, 4.0, 10.0, and 20.0 m each of thickness $d_{inc} = 0.3$ m and $\mu_{inc} = 12.5$ m^{-1}. We used false alarm rate $P_{FA} = 0.05$ and considered a heavy fog turbid medium with $\mu_t = 12.5^{-1}$ m^{-1}. Using the analysis from above, $d_{critical} = 417$ m, which is consistent with earlier results we showed in Section 3. Figure 17 shows the effect of distance on the ballistic resolution, illustrating the captured ballistic and diffused (conventional) images at distances of $d = 350, 400, 417$ m.

References

1. C. Dunsby and P. M. W. French, "Techniques for depth-resolved imaging through turbid media including coherence-gated imaging," J. Phys. D **36,** 207–227 (2003).
2. K. Yoo and R. R. Alfano, "Time-resolved coherent and incoherent components of forward light scattering in random media," Opt. Lett. **15,** 320–322 (1990).
3. A. F. Fercher, W. Drexler, C. K. Hitzenberger, and T. Lasser, "Optical coherence tomography —principles and applications," Rep. Prog. Phys. **66,** 239–303 (2003).
4. M. E. Zevallos, S. K. Gayen, M. Alrubaiee, and R. R. Alfano, "Time-gated backscattered ballistic light imaging of objects in turbid water," Appl. Phys. Lett. **86,** 0111151–0111153 (2005).
5. M. Paciaroni and M. Linne, "Single-shot, two-dimensional ballistic imaging through scattering media," Appl. Opt. **43,** 5100–5109 (2004).
6. D. Contini, F. Martelli, and G. Zaccanti, "Photon migration through a turbid slab described by a model based on diffusion approximation. I. Theory," Appl. Opt. **36,** 4587–4599 (1997).
7. I. Delfino, M. Lepore, and P. L. Indovina, "Experimental tests of different solutions to the diffusion equation for optical characterization of scattering media by time-resolved transmittance," Appl. Opt. **38,** 4228–4236 (1999).
8. W. Cai, S. K. Gayen, M. Xu, M. Zevallos, M. Alrubaiee, M. Lax, and R. R. Alfano, "Optical tomographic image reconstruction from ultrafast time-sliced transmission measurements," Appl. Opt. **38,** 4237–4246 (1999).
9. B. B. Das, F. Liu, and R. R. Alfano, "Time-resolved fluorescence and photon migration studies in biomedical and model random media," Rep. Prog. Phys. **60,** 227–292 (1997).
10. A. Gibson, J. Hebden, and S. Arridge, "Recent advances in diffuse optical imaging," Phys. Med. Biol. **50,** R1–R43 (2005).
11. H. Lischke, T. J. Loeffler, and A. Fischlin, "Aggregation of individual trees and patches in forest succession models: capturing variability with height structured, random, spatial distributions," Theor. Popul. Biol. **54,** 213–236 (1998).
12. S. V. Aert, D. V. Dyck, and A. J. den Dekker, "Resolution of coherent and incoherent imaging systems reconsidered—classical criteria and a statistical alternative," Opt. Express **14,** 3830–3839 (2006).
13. S. M. Kay, *Fundamentals of Statistical Signal Processing: Estimation Theory* (Prentice-Hall, 1993), Vol. 1.
14. L. L. Scharf, *Statistical Signal Processing: Detection, Estimation, and Time Series Analysis* (Addison-Wesley, 1991).
15. G. W. Sutton, "Fog hole boring with pulsed high-energy lasers—an exact solution including scattering and absorption," Appl. Opt. **17,** 3424–3430 (1978).
16. S. M. Kay, *Fundamentals of Statistical Signal Processing Detection Theory* (Prentice-Hall, 1998), Vol. 2.
17. M. Shahram and P. Milanfar, "Imaging below the diffraction limit: a statistical analysis," IEEE Trans. Image Processing **13,** 677–689 (2004).
18. A. Sommerfeld, *Optics Lectures on Theortical Physics* (Academic, 1954), Vol. 4.
19. J. Goodman, *Introduction to Fourier Optics,* 3rd ed. (Roberts and Company, 2005).
20. G. B. Parrent, Jr. and B. J. Thompson, "On the Fraunhofer (far field) diffraction patterns of opaque and transparent objects with coherent background," J. Mod. Opt. **11,** 183–193 (1964).
21. D. N. Nikogosyan, "Beta barium borate (BBO)," Appl. Phys. A **52,** 359–368 (1991).
22. M. Ghotbi and M. Ebrahim-Zadeh, "Optical second harmonic generation properties of BiB$_3$O$_6$," Opt. Express **12,** 6002–6019 (2004).
23. E. Candès, J. Romberg, and T. Tao, "Stable signal recovery from incomplete and inaccurate measurements," Commun. Pure Appl. Math. **59,** 1207–1223 (2006).
24. J. Haupt and R. Nowak, "Signal reconstruction from noisy random projections," IEEE Trans. Inf. Theory **52,** 4036–4048 (2006).
25. R. Castro, J. Haupt, and R. Nowak, "Compressed sensing vs. active learning," in *2006 International Conference on Acoustics, Speech and Signal Processing* (IEEE, 2006), pp. 820–823.
26. D. Donoho, M. Elad, and V. Temlyakov, "Stable recovery of sparse overcomplete representations in the presence of noise," IEEE Trans. Inf. Theory **52,** 6–18 (2006).
27. M. Wakin, J. Laska, M. Duarte, D. Baron, S. Sarvotham, D.

Takhar, K. Kelly, and R. Baraniuk, "An architecture for compressive imaging," in *2006 International Conference on Image Processing* (IEEE, 2006), pp. 1273–1276.

28. R. Castro, R. Willett, and R. Nowak, "Faster rates in regression via active learning," in *2005 Advances in Neural Information Processing Systems 18* (MIT Press, 2005), pp. 179–186.

29. S. Farsiu, D. Robinson, M. Elad, and P. Milanfar, "Fast and robust multi-frame super-resolution," IEEE Trans. Image Processing **13,** 1327–1344 (2004).

30. B. Eriksson and R. Nowak, "Maximum likelihood methods for time-resolved imaging through turbid media," in *2006 International Conference on Image Processing* (IEEE, 2006), pp. 641–644.

31. S. Fantini, S. Walker, M. Franceschini, M. Kaschke, P. Schlag, and K. Moesta, "Assessment of the size, position, and optical properties of breast tumors *in vivo* by noninvasive optical methods," Appl. Opt. **37,** 1982–1989 (1998).

32. F. Anscombe, "The transformation of Poisson, binomial and negative-binomial data," Biometrika **35,** 246–254 (1948).

33. R. Miller, *Simultaneous Statistical Inference* (Springer, 1991).

34. A. Gandjbakhche, G. Weiss, R. Bonner, and R. Nossal, "Photon path-length distributions for transmission through optically turbid slabs," Phys. Rev. E **48,** 810–818 (1993).

35. A. Gandjbakhche, R. Nossal, and R. Bonner, "Resolution limits for optical transillumination of abnormalities deeply embedded in tissues," Med. Phys. **21,** 185–191 (1994).

36. V. Chernomordik, R. Nossal, and A. Gandjbakhche, "Point spread functions of photons in time-resolved transillumination experiments using simple scaling arguments," Med. Phys. **23,** 1857–1861 (1996).

RESOLUTION BOUNDS AND RECONSTRUCTION TECHNIQUES FOR TIME-RESOLVED TRANSILLUMINATION IMAGING

BRIAN ERIKSSON AND ROBERT NOWAK*

Abstract.
Recent technological advances now enable time-gated acquisition of photons at very fast rates. This allows one to separate scattered and unscattered photons by temporal gating, a process termed time-resolved transillumination (TRT) imaging. TRT imaging opens the door to a new type of scanning through turbid (scattering) media such as soft tissue and fog/smoke, and many potential applications in bioimaging and surveillance. This paper investigates the performance tradeoffs between TRT imaging and conventional (un-gated) imaging. On the one hand, time-gated, first-arrival photons are unscattered and therefore provide very high spatial resolution. But, very few photons arrive at the detector without scattering, effectively resulting in a very low SNR. On the other hand, conventional (un-gated) imaging is based on all photons (scattered and unscattered), resulting in lower spatial resolution, but higher SNR (due to the large number of photons). This paper investigates these tradeoffs using a decision-theoretic approach to ascertain bounds on the minimum resolvable occluding object size with and without time-gated photon acquisition. The theoretical predictions are validated through a realistic simulation of tumors in breast tissue. The paper then proposes a novel Maximum Likelihood approach to TRT image reconstruction. Using a novel Expectation-Maximization algorithm, multiple snapshot observations of time-gated photons are used to reconstruct the image. This allows us to obtain the "best-of-both-worlds" by combining the spatial resolution of the first-arrival photons, with the higher SNR provided by scattered photons.

Key words. Transillumination imaging, Time-gated imaging, Photon-limited imaging, Image reconstruction, High-resolution imaging

AMS subject classifications. 62C05, 94A08

1. Introduction. Recent technological advances now enable time-gated acquisitions of photons at very fast rates, fast enough to separately collect unscattered (first-arrival) and scattered (later-arrival) photons in transillumination imaging [1]. We refer to this technology as time-resolved transillumination (TRT) imaging. TRT imaging opens the door to a new type of imaging through turbid (scattering) media (e.g., soft tissue, fog/smoke). The ability to separately detect unscattered, so-called *ballistic*, photons can enable much higher spatial resolution imaging than possible using conventional (un-gated) imaging devices, and this has many potential applications in bioimaging and surveillance. However, a tradeoff exists, since the number of ballistic photons decays exponentially as the thickness/depth of the turbid medium increases. Therefore, the high resolution information that is available is often in a very photon-limited, low SNR regime. This paper explores a novel approach to TRT image reconstruction and a decision-theoretic approach towards deriving bounds on achievable spatial resolution.

In more detail, the TRT imaging problem involves photons traveling through a turbid medium from a source (usually a laser), through a scattering medium, and then onto a detector plane as depicted in Fig. 1.1. Photons traveling through a scattering medium can be roughly classified into three types: ballistic, snake, and diffuse. Ballistic photons experience no scattering and thus travel in a direct line of sight, arriving first at the detector. Because of the lack of scattering, ballistic photons retain their spatial information and arrive at the detector plane at the same

---

*Department of Electrical and Computer Engineering, University of Wisconsin - Madison, 1415 Engineering Hall, Madison, Wisconsin, 53706 (`bceriksson@wisc.edu, nowak@ece.wisc.edu`), This work was partially supported by DARPA/AFOSR grant number FA9550-06-1-0047.

planar location as sent from the light source. In the intermediary regime, "snake photons" experience slight scattering through the medium, this scattering will cause these photons to arrive later than the ballistic photons and likely in a slightly different planar location than the light source (resulting in a small loss of spatial resolution). The third class, diffuse photons, experience large amounts of scattering and arrive at the image plane having lost most of their point of origin information. Due to the large number of scattering events through the medium, the diffuse photons will travel the farthest distance to the detector plane, and therefore will arrive after the snake and ballistic photons. While the inherent spatial information decreases in order of ballistic, snake and diffuse photons, the number of photons (and hence inherent SNR) increases in the same order. So we are faced with high resolution, low SNR data at one extreme (ballistic), and low resolution, high SNR data at the other (diffuse). Furthermore, the diffusion and SNR parameters, which characterize the underlying point spread function (PSF), are not known precisely in practice.
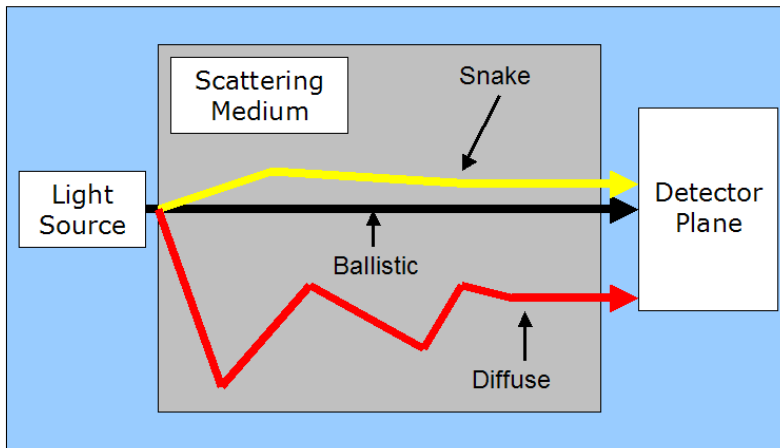
Fig. 1.1. *Example of Photons Through a Scattering Medium*

1.1. Related Works. The majority of the previous work in the area of transillumination imaging has been focused on finding the resolution limits on an observation using the diffuse photons [1],[2],[3],[4],[5],[6]. Relatively little work has been performed on characterizing the resolution limits of the ballistic observation (most notably [7] and [1], neither of which take detection error rates into careful consideration). To the best of our knowledge, this is the first attempt to quantify the tradeoff between ballistic and diffuse photons in terms of achievable spatial resolution. Previous work has been performed on iterative least-squares methods to reconstruct images based on time-resolved turbid medium observations ([8], [9]). This paper is the first attempt at using a maximum likelihood approach to estimate turbid medium parameters, and also the first attempt at developing an EM algorithm for transillumination image reconstruction.

1.2. Organization. This paper is divided into three parts. Section 2 uses a decision-theoretic approach to derive resolution bounds for turbid environments. In Section 3 we introduce an estimation-theoretic approach to TRT image reconstruction. A statistical model for TRT imaging is purposed, and then an EM algorithm using

a penalized maximum likelihood approach is described. Finally, in Section 4 we will simulate transillumination imaging through breast tissue and examine the EM algorithm image reconstruction results.

2. Resolution Bounds for Conventional and Time-Resolved Imaging. The resolution of an transillumination imaging system can be quantified in terms of the smallest occluding object that can be reliably detected and located. To address this issue, we consider the following imaging process. Assume that the source and detector pair scan the area of the detector plane (A) at points on an $n \times n$ grid, to create a pixelated cross-section of the detector plane area A. We assume that the region between the source and detector is a homogenous scattering medium, possibly containing occluding objects embedded in the region. Our goal is to determine the smallest occluding object that can be reliably detected. The size of an occluder is measured by its cross-sectional diameter (w^o in Figure 2) and its thickness (d^o in Figure 2). We adopt a cylindrical object model so that the scattering properties along the line-of-sight between the source and detector are spatially uniform (a spherical object model could also be considered, but because its thickness would vary depending on where the line-of-sight intersects the sphere, its analysis would be slightly more complicated).

For this section, only the two extremes of the imaging regime will be considered, the ballistic regime where only early arriving, unscattered photons are detected using high-speed gating mechanisms, and the conventional imaging regime where all the photons arriving at the detector are utilized (i.e. no time-gating). We characterize the minimum size occluder that can be reliable resolved in these two regimes, and show that there is a distinct threshold on the total image acquisition time, below which conventional imaging offers better spatial resolution an above which ballistic imaging is superior. This threshold is a function of the parameters of the scattering medium and occluding material.
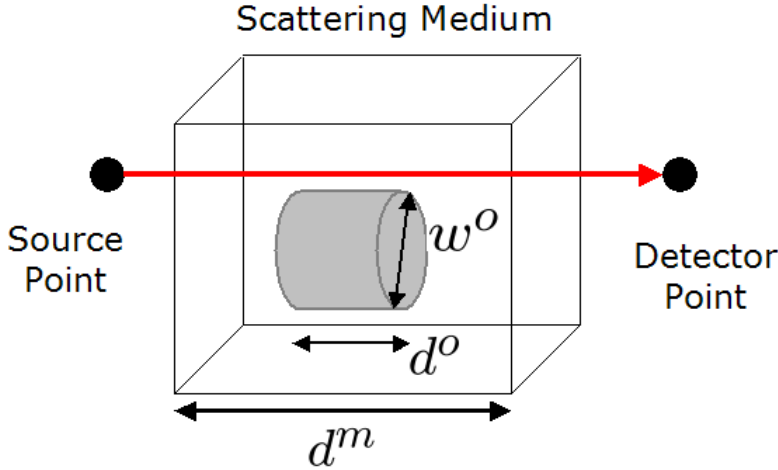

FIG. 2.1. *Turbid Medium Model Example*

A turbid medium may be considered as any scattering material, but for example purposes throughout the paper we will assume it to be a homogeneously scattering

section of human tissue. The scattering material is parameterized by the number of photon scatters per unit length (the *scattering coefficient*) μ_s^m, the fraction of absorptions per length (the *absorbtion coefficient*) μ_a^m, and the length of the medium, d^m. Between the source and detector in the medium there may exist occluding objects, which could represent tumors in the bioimaging context. For the purposes of our resolution bound analysis, we assume that the occluders are located in the plane midway between the source detector, since this is the plane in the medium where the variance of the scattering will be at a maximum [2],[3]. To completely define the environment, one must take into consideration the scattering properties of occluders (scattering and absorption coefficients denoted by μ_s^o, μ_a^o, respectively). In general, the numbers, locations and geometrical properties of occluding objects may be arbitrary, but for the purposes of determining the minimum resolvable occluder size, we assume a cylindrical occluder of thickness d^o and width w^o.

We first consider the spatial resolution of conventional (un-gated) imaging, which can be determined via classical random-walk diffusion techniques and depends only on the properties of the scattering medium, and not on the particular properties of the occluders. Then we consider the spatial resolution achievable from ballistic photon imaging. Since the numbers of detected ballistic photons depend on the properties of both the scattering medium and the occluders, this analysis is somewhat more complex than that of conventional imaging. We cast the ballistic imaging problem as a multiple testing problem, where our goal is to reliable decide whether or not an occluder lies along the line-of-sight between the source and detector at each of the $n \times n$ scan locations.

2.1. Conventional Imaging Resolution. In the conventional imaging, there is no time-gating mechanism and all the photons that reach the detector, over a relatively long integration time, are recorded. This results in a high SNR, but since most of the photons are scattered, the spatial resolution is limited. In effect, the resulting image is blurred, but not very noisy. Methods for determining the blurring caused by scattering vary in complexity. Simple linear techniques found in [4],[10] have been shown to fit experimental data well for short integration times. Due to the absorption of photons traveling long distances, these linear techniques do not hold as the integration time tends to infinity. More complicated methods using Monte Carlo techniques ([6]), or diffusion theory calculations ([1],[5]) are found to be more accurate when considering long integration times. Another method accurate with respect to long integration times uses random walk theory in [2],[3], and due to the accuracy and simplicity of the method we will consider this approach. The blurring effect caused by scattering can be modeled as a convolution with a Gaussian kernel. The standard deviation of the Gaussian kernel is found using the photon mean-time-of-flight $\langle \Delta t \rangle$, which can be numerically solved ([2], Eqn. 16) using the parameters of the medium (μ_s^m, μ_a^m). The full-width half-maximum of the Gaussian kernel is

$$w_{conv}^o = 0.94 \left(\frac{\langle \Delta t \rangle c}{\mu_s^m} \right)^{\frac{1}{2}} \tag{2.1}$$

which provides a reasonable measure of the spatial resolution of a conventional imaging system operating in transillumination mode through the given medium.

2.2. Ballistic Imaging Resolution. To begin, let us first consider the statistics of detected ballistic photons along a single line-of-sight. The problem of determining whether or not an occluder lies along the line-of-sight can be cast as a statistical

hypothesis test, as follows. Given the ballistic photon count X at the detector, one must choose between two hypotheses. The first is that no occluding object exists in the path between the source and detector, which we denote by $\mathcal{H}_0$. The alternative is that there is an occluder along the line-of-sight, denoted by $\mathcal{H}_1$. Occluders are considered to be significantly more scattering than the surrounding medium (e.g., tumors in human tissue [11]), and therefore the detector will collect an attenuated number of ballistic photons under $\mathcal{H}_1$ compared to $\mathcal{H}_0$).

The probability of a photon passing through the scattering medium with no scattering events (i.e. the probability of a photon of being a ballistic photon) is exponentially distributed with rate parameter $(\mu_s^m + \mu_a^m)\, d^m$. Given the source intensity λ, equal to the number of photons sent through the medium by the per unit time, and assuming that no occluder lies along the path between source and detector, one can determine the intensity of the ballistic photon arrival process at the detector:

$$\lambda_0 \;=\; \lambda \exp\left(-\left(\mu_s^m + \mu_a^m\right) d^m\right) \tag{2.2}$$

When an occluder does lie along the path, the intensity of the ballistic photon arrival process is attenuated:

$$\lambda_1 \;=\; \lambda \exp\left(-\left(\mu_s^m + \mu_a^m\right)\left(d^m - d^o\right) - \left(\mu_s^o + \mu_a^o\right) d^o\right) \tag{2.3}$$

In addition to ballistic photons due to the source, stray "noise" photons due to background light sources, arriving during the time-gate interval of acquisition, will also be detected. Let λ_b denote the average intensity of this arrival process.

We can now express the probability distributions of the photon count at the detector, under the two hypotheses.

$$\mathcal{H}_0 : X \sim \mathcal{P}\left((\lambda_b + \lambda_0)\, t\right) \tag{2.4}$$

$$\mathcal{H}_1 : X \sim \mathcal{P}\left((\lambda_b + \lambda_1)\, t\right) \;, \tag{2.5}$$

where t is the length of the time-gate interval in seconds and $\mathcal{P}(\Lambda)$ denotes the Poisson distribution whose probability mass function is given by $p(X = m) = e^{-\Lambda}\Lambda^m/m!$. As the mean, Λ, of the Poisson distribution grows, the probability distribution tends to a Gaussian. Averaging repeated trials (i.e., averaging of multiple laser pulses) therefore results in a Gaussian distributed statistic. Using the Anscombe Transformation [12], we can obtain approximately Gaussian distributed statistics. If $X \sim \mathcal{P}(\Lambda)$, then the Anscombe transformed variable $2\sqrt{X + \frac{3}{8}}$ is asymptotically (as $\Lambda \to \infty$) Gaussian distributed as $\mathcal{N}\left(2\sqrt{\lambda}, 1\right)$ (where $\mathcal{N}\left(\mu, \sigma^2\right)$ is a Gaussian distribution with mean μ and variance σ^2). In fact, the approximation to Gaussian is quite accurate even when Λ is relatively small (e.g., $\Lambda = 20$). Thus, we transform the photon count X to obtain a new statistic $X' = 2\sqrt{X + \frac{3}{8}}$. Letting $T = kt$ denote the total acquisition time, over k trials with t units of time per trial, the resulting Gaussian hypotheses are given by:

$$\mathcal{H}_0 : X' \sim \mathcal{N}\left(2\sqrt{(\lambda_b + \lambda_0)\, T}, 1\right) \tag{2.6}$$

$$\mathcal{H}_1 : X' \sim \mathcal{N}\left(2\sqrt{(\lambda_b + \lambda_1)\, T}, 1\right) \tag{2.7}$$

The decision test is now defined as $\left(X' \lessgtr^{\mathcal{H}_1}_{\mathcal{H}_0} \gamma' \right)$. The probability of error of this test can be expressed in terms of the Gaussian error function $\Phi(t) := \int_t^\infty \frac{1}{\sqrt{2}} e^{-t^2/2}$, as

$$ p \;=\; 2\Phi \left(\sqrt{(\lambda_b + \lambda_0)T} - \sqrt{(\lambda_b + \lambda_1)T} \right) \;=\; 2\Phi \left(\sqrt{T}\Delta_\lambda \right) $$

where $\Delta_\lambda = \sqrt{\lambda_b + \lambda_0} - \sqrt{\lambda_b + \lambda_1}$.

Now recall that our goal is to create a pixelated image at $n \times n$ points over the FOV. In other words, the testing procedure above will be repeated at n^2 different locations. Whenever a statistical test is repeated multiple times, the chance that one or more is in error increases with the number of trials. Our goal is to guarantee a low probability of error at all n^2 locations (i.e., to control the probability that an erroneous decision is made at one or more of the pixel locations). This probability is bounded by the sum of the probability of error at each location. That is, the overall probability that one or more pixels is in error is bounded by $n^2 p$. This bound is called the Bonferroni or union bound. Thus, if we desire an overall probability of error p_e, then we require that

$$ n \;\leq\; \sqrt{p_e/p} \;=\; \left(\frac{p_e}{2\Phi \left(\sqrt{T}\Delta_\lambda \right)} \right)^{1/2} $$

The minimum width of an occluder that can be reliably resolved for a given turbid medium can now be derived. Using the upper bound for n above, we can solve for the lower bound on the width using $w^o_{ballistic} = \sqrt{\frac{A}{n^2}}$ (where A is the area of the detector plane):

$$ w^o_{ballistic} = \sqrt{A/n^2} \tag{2.8} $$

$$ \geq \left(\frac{2A\Phi \left(\sqrt{T}\Delta_\lambda \right)}{p_e} \right)^{1/2} \tag{2.9} $$

This equation shows how the minimum resolvable occluder size depends on the parameters of the imaging system.

This resolution can be contrasted with that of the conventional imaging system given by (2.1). The critical acquisition time, T_{critical} (per pixel), at which the resolution of the ballistic system $w^o_{ballistic}$ is equal to that of the conventional system w^o_{conv}, is given by

$$ T_{\text{critical}} = \left[\Delta_\lambda \, \Phi^{-1} \left((0.94)^2 \frac{p_e \langle \Delta t \rangle \, c}{2A\mu^m_s} \right) \right]^2 \tag{2.10} $$

At acquisition rates below T_{critical}, conventional imaging provides better resolution than ballistic imaging, and the converse is true at faster rates above T_{critical}. Determination of T_{critical} requires specification of the parameters of the turbid medium and occluding material, and the allowable error level in the ballistic case (e.g., $p_e = 0.05$). We will examine the critical acquisition time in examples in the following sections.

3. TRT Image Reconstruction. The analysis above demonstrates that ballistic imaging can provide statistically reliable, higher resolution images than conventional imaging in certain situations. In this section, we develop a novel approach to

TRT image reconstruction that takes advantage of both the high resolution of ballistic photons, and the higher SNR associated with conventional imaging, leveraging the best of both regimes.

The TRT image reconstruction problem can be posed as a statistical inverse problem (a particular form of photon-limited image reconstruction), but to the best of our knowledge our work here is the first to formulate it as such. Due to uncertainties in the blurring kernel (dependent on usually unknown parameters of the turbid medium), the TRT problem is somewhat related to blind image deconvolution (BID). While BID is a well-studied problem, there are several unique aspects in the TRT imaging problem that make it quite different from standard BID problems. In particular, the distinctive features of TRT imaging include the photon-limited nature of the data, the time-gated data acquisition which in effect yields information at multiple spatial resolutions that can be fairly well characterized via a diffusion equation, and most importantly the availability of "unblurred" data corresponding to the ballistic photons. For these reasons "off-the-shelf" BID algorithms are not directly applicable to TRT image reconstruction.

3.1. A Statistical Model of TRT Imaging. The basic statistical model we propose for TRT imaging through homogeneous turbid media is as follows. Assume that we have k time-resolved "snapshots", each acquired over disjoint time intervals $T^{(1)}, \ldots, T^{(k)}$, with $T^{(1)}$ denoting the ballistic time interval. Assume that these intervals form a uniform partition of the overall observation interval, denoted $\mathcal{T} > 0$. Let $X^{(1)}, \ldots, X^{(k)}$ denote the photon data acquired in each interval, respectively. Specifically, the data $X^{(i)}$ are acquired in the form of an $n \times n$ pixel image, and for our mathematical exposition we assume that the columns of this image are "stacked" to form an $n^2 \times 1$ vector. Each entry in $X^{(i)}$ is simply the number of photons detected at the corresponding pixel location during the time interval $T^{(i)} = \left[\frac{i-1}{K}\mathcal{T}, \frac{i}{K}\mathcal{T}\right)$. We assume that each image is Poisson distributed according to the following model:

$$X^{(i)} \sim \text{Poisson}(\alpha^{(i)} P^{(i)} \lambda), \quad i = 1, \ldots, k, \tag{3.1}$$

where λ denotes the underlying $n^2 \times 1$ image intensity function we wish to reconstruct, $P^{(i)}$ denotes the $n^2 \times n^2$ photon transition matrix (from the emission (source) plane to the detector plane) reflecting the diffusion process governing photon migration during each time interval, and $\alpha^{(i)} > 0$ is a scalar gain factor reflecting the varying abundances of detected photons in the differing regimes, from ballistic to diffuse.

The transition matrices are functions of time and a scalar diffusion bandwidth parameter denoted by σ^2. Using the elementary linear models of the photon migration and diffusion process found in [4, 10], we model $P^{(i)}$ as a linear shift-invariant Gaussian blurring kernel with variance proportional to $\sigma^2 t^{(i)}$, where $t^{(i)}$ denotes the midpoint of the i-th acquisition time-interval. Thus, the transition matrices are parametric functions of the form $P^{(i)} = P(\sigma^2 t^{(i)})$, where only the variance coefficient σ^2 needs to be estimated. Also, due to the linear shift-invariant nature of the model, the resulting blurring process is a convolution, and thus the forward solution can be rapidly computed via the Fast Fourier Transform (FFT) algorithm (a property we will exploit in our reconstruction algorithms).

We assume that λ is normalized such that the intensities in λ sum to one (i.e., $\sum_{j=1}^{n^2} \lambda(j) = 1$). Also the transition matrices are normalized so that $\mu^{(i)} = P^{(i)} \lambda$ also satisfies $\sum_{j=1}^{n^2} \mu^{(i)}(j) = 1$. With these normalizations, it is easy to verify that the total intensity (expected total number of detected photons) of the snapshot $X^{(i)}$ is the

gain α_i, $i = 1, \ldots, k$. Furthermore, we adopt the convention that the ballistic image resolution is the finest spatial resolution available and assume that $P^{(1)}$ is the $n^2 \times n^2$ identity matrix. We also assume that the images acquired in each time-interval are statistically independent, and so the joint distribution function of the entire $kn^2 \times 1$ data record, obtained by stacking the snapshots into a single column vector

$$X = \begin{bmatrix} X^{(1)} \\ \vdots \\ X^{(k)} \end{bmatrix},$$

is

$$X \sim \text{Poisson}(P\lambda), \tag{3.2}$$

where P is the $kn^2 \times n^2$ transition matrix obtained by stacking the matrices $\alpha^{(1)}P^{(1)}, \ldots, \alpha^{(k)}P^{(k)}$; i.e.,

$$P = \begin{bmatrix} \alpha^{(1)}P^{(1)} \\ \vdots \\ \alpha^{(k)}P^{(k)} \end{bmatrix}.$$

Let us contrast the above model of the TRT imaging system with a conventional imaging system in which the photon detections are not time-resolved. In this case, we acquire the aggregated photon image $X_a = X^{(1)} + \cdots + X^{(k)}$, which obeys the model

$$X_a \sim \text{Poisson}(P_a\lambda), \tag{3.3}$$

where $P_a = \sum_{i=1}^{k} \alpha^{(i)}P^{(i)}$. We will see that the extra information available in the time-resolved photon acquisition can significantly improve our ability to estimate the underlying intensity λ.

3.2. Maximum Likelihood Reconstructions. Both the TRT imaging model, $X \sim \text{Poisson}(P\lambda)$, and the conventional imaging model, $X_a \sim \text{Poisson}(P_a\lambda)$, are in the form of the basic statistical model usually considered in photon-limited imaging problems [13]. If the parameters of the imaging system (i.e., the gains α_i and the diffusion parameter σ^2) are known, then standard techniques can be applied to find the Maximum Likelihood Estimate (MLE) of λ.

To define the MLE, let $p(X|\lambda)$ denote the likelihood function of the data (i.e., the Poisson probability mass function evaluated at X and viewed as a function of λ). The MLE is the solution to the following optimization:

$$\widehat{\lambda}_{MLE} = \arg\max_{\lambda} p(X|\lambda) \tag{3.4}$$

More specifically, taking the logarithm of the likelihood function (a monotonic transformation), we have

$$\widehat{\lambda}_{MLE} = \arg\max_{\lambda} \sum_{i=1}^{k} \left(\alpha^{(i)}P^{(i)}\lambda + X^{(i)}\log\alpha^{(i)}P^{(i)}\lambda - \log X^{(i)}! \right) \tag{3.5}$$

There is no closed-form solution for the $\widehat{\lambda}_{MLE}$, but the log-likelihood function is convex in λ. Thus, numerical optimization techniques can be readily applied. One very

popular and effective optimization procedure is the so-called Expectation-Maximization (EM) algorithm [13]. The EM algorithm is an iterative procedure that is guaranteed to produce a sequence of iterates, $\lambda^{(1)}, \lambda^{(2)}, \ldots$, that have non-decreasing likelihood values (i.e., each iteration of the algorithm does not decrease the likelihood value). The EM algorithm can work very well in practice, but usually requires an ad hoc stopping criterion, since the MLE solution can very noisy in severely photon-limited and/or ill-posed cases. Stopping the algorithm prior to convergence provides an indirect smoothing of the solution.

A more desirable alternative to the early stopping of the EM algorithm is to tackle the undesirable aspects of the MLE solution more directly. This is usually accomplished by augmenting the likelihood criterion with an additive penalty function which discourages solutions that are rough and irregular. The generic form of penalized solutions is

$$\widehat{\lambda} = \arg\max_{\lambda} \ [\log(p(X|\lambda) \ + \ \text{pen}(\lambda)] \tag{3.6}$$

where $\text{pen}(\lambda) > 0$ is a penalty function that assigns small values to smooth λ and larger values to non-smooth λ. The notion of smoothness depends on the nature of the penalty, and many possibilities have been studied in the literature (see [14] and the references therein). In particular, we advocate the use of multiscale complexity penalty [15, 14], which tends to favor solutions that are piecewise smooth. The multiscale complexity penalty leads to a denoising process akin to wavelet thresholding methods, but particularly adapted to Poisson data [16, 15, 17, 14]. Figure 3.1 illustrates the denoising capability of the multiscale complexity penalty. In this example, a single photon-limited snapshot was acquired, without blur (i.e., the corresponding photon transition matrix is the identity operator). The denoising process is carried out via a computationally efficient multiscale tree-pruning process (akin to wavelet coefficient thresholding) that requires $O(n^2)$ operations for an $n \times n$ image.

(a)   (b)   (c)
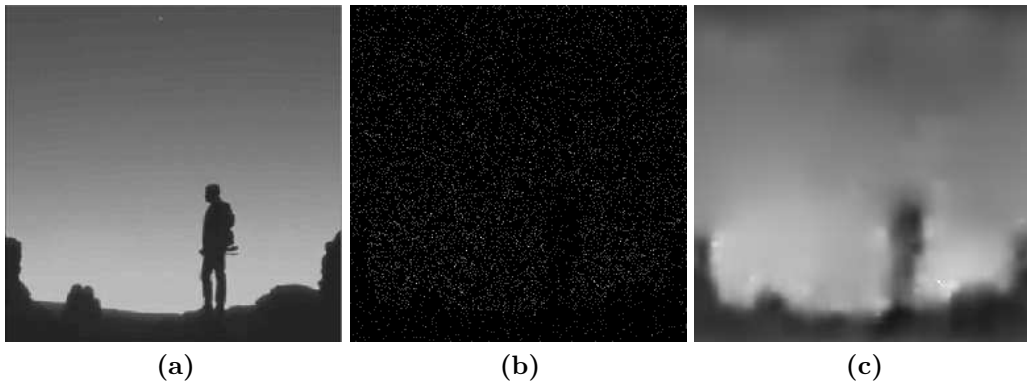
FIG. 3.1. *Night sky image (a) Original Image, (b) Poisson photon count image, (c) MPLE Denoised Image, resulting from the MPLE proposed in*

The multiscale complexity penalty can also be easily integrated into an EM algorithm, by replacing the conventional (MLE) M-step with a denoising step (see [17] for further details). Iterating this modified EM algorithm to convergence produces a Maximum Penalized Likelihood Estimate (MPLE). To the best of our knowledge, the quality of the MPLE solution, in terms of squared error, is state-of-the-art [17],

and so we will exclusively use this reconstruction process here. Each iteration of the EM algorithm follows a two-step procedure. In the E-step, the conditional expectation of the so-called "complete data" is computed. The complete data is an $n^2 \times n^2$ array in which the i, j element is equal to the number of photons emitted from position i and detected at position j. Of course, we only observe the detected photons, without knowledge of where they originated from, and so the complete data must be estimated based on the photon detections X and the current iterate of λ. The E-step requires computing matrix vector products with the transition matrices $P^{(i)}$ (see pseudocode below). Since the transition matrix operation is a linear convolution, these products can be rapidly computed via the Fast Fourier Transform (FFT) algorithm. From the complete data, we can compute the photon emission counts by marginalization (providing data as if no diffusion/blurring process occurred). The exact (not estimated) photon emission counts gives the MLE for λ. Thus, the standard M-step (corresponding to the MLE) simply computing the estimated photon emission counts by marginalizing the expectation of the complete data. The modified M-step (corresponding to the MPLE) is obtained by applying the multiscale complexity penalty denoising process [15, 14] to the estimated photon emission counts. The pseudocode below outlines the steps of the EM algorithm. The algorithm produces a sequence of iterates, and the corresponding sequence of penalized log-likelihood values is monotonic, non-decreasing (see [17] for further details).

Algorithm 1 - MPLE EM Algorithm with Known Parameters

Initialize: Set iteration counter $j = 0$ and $\lambda^{(0)}(m) = 1/n^2$, m=1,…,n^2.

E-Step: Compute the conditional expectation of the complete data (c.f. [13]):

$$Z^{(j)}(\ell, m) = \sum_{i=1}^{k} X^{(i)}(\ell) \frac{\lambda^{(j)}(m) \alpha^{(i)} P^{(i)}(\ell, m)}{\sum_{m=1}^{n^2} \lambda^{(j)}(m) \alpha^{(i)} P^{(i)}(\ell, m)}$$

M-Step:
  1. Compute the expected photon emission counts via marginalization:

$$\mu^{(j)}(m) = \sum_{\ell=1}^{n^2} Z^{(j)}(\ell, m) \quad, \quad i = 1, \ldots, k$$

  2. Apply the multiscale complexity penalized denoising procedure to $\mu^{(j)}$ to obtain updated iterate $\lambda^{(j+1)}$. The Poisson denoising procedure was first proposed in [15], and the implementation employed in this work is a translation invariant version developed by R. Willett. Code is on-line at [18].

Repeat: Set $j = j + 1$. Repeat E- and M-steps until convergence.

3.3. Adapting to Unknown Turbid Media. One of the major challenges in practical imaging problems is that the characteristics of the turbid medium are usually not known precisely. In particular, the values of the parameters $\{\alpha^{(i)}\}$ and σ^2 are unknown and therefore must be estimated along with λ. We can formulate this

as a joint MLE problem, seeking to find values of the parameters and λ which jointly maximize the Poisson likelihood function (or penalized likelihood). At first glance, it may appear that this joint MLE problem may be intractable, but it turns out to have a rather simple solution.

The basic solution approach is as follows. First, the MLEs of the gain factors $\{\alpha^{(i)}\}_{i=1}^k$ can be computed separately from λ and σ^2 due to the following observation. Consider the statistics

$$S^{(i)} = \sum_{\ell=1}^{n^2} X^{(i)}(\ell), \quad i = 1, \ldots, k.$$

These statistics are simply the total photon counts for each image. Due to the normalization of λ and the matrices $\{P^{(i)}\}$ in our model, it follows that

$$S^{(i)} \sim \text{Poisson}(\alpha^{(i)}), \quad i = 1, \ldots, k.$$

It is well-known that the conditional distribution of $X^{(i)}$ given $S^{(i)}$ is multinomial with parameter $\mu^{(i)} = P^{(i)}\lambda$ (see [15]). Therefore, the likelihood factorizes into Poisson factors, each involving one pair $(\alpha^{(i)}, S^{(i)})$, and multinomial factors, each involving λ and one triple $(P^{(i)}, X^{(i)}, S^{(i)})$. Consequently, the MLEs of the gain factors $\{\alpha^{(i)}\}$ can be obtained separately from λ and σ^2 and are given by the simple formula $\widehat{\alpha^{(i)}} = S^{(i)}$, $i = 1, \ldots, k$. Now recall that the matrices $\{P^{(i)}\}$ are parametric in σ^2. To find the MLEs of λ and σ^2 we consider a range of candidate values for σ^2 and for each one we use the EM algorithm described above (with each $\alpha^{(i)}$ set to its MLE $\widehat{\alpha^{(i)}}$) to compute the MPLE, denoted by $\widehat{\lambda}(\sigma^2)$, and the corresponding maximum penalized likelihood value, denoted $L(\sigma^2)$. This can be done exhaustively over a discretized range of σ^2 values, by performing the EM algorithm for each discretized value of σ^2. The value of σ^2 that results in the highest penalized likelihood value $L(\sigma^2)$ is considered the MLE of σ^2, denoted by $\widehat{\sigma^2}$. The MPLE of λ is then $\widehat{\lambda}(\widehat{\sigma^2})$. Another, less computationally expensive option, is to incrementally adjust the value of σ^2 at each iteration of the EM algorithm (see pseudocode below for details). This iterative method of estimation is performed in the experimental portion of this paper and was repeatedly found to converge to the true value of σ^2.

4. Experimental Results. We now present a simulation study of imaging malignant breast tissue through healthy breast tissue. For this simulation, a medium with a 100mm x 100mm detector plane area (A) and length $d^m = 10$mm is defined with circular occluding objects of diameter 2mm, 4mm, 8mm, 20mm, and 40mm. From [11], we use the scattering and absorption coefficients of the two tissue types (healthy breast tissue, malignant tissue). Using a specified thickness of the occluding tumor (d^o=2.5mm) and false alarm rate ($p_e = 0.05$), we use Equation 2.10 and find T_{critical} to equal 154ms. We simulate a series of ten snapshot observations through the medium using four different (per snapshot) acquisition time values ($T = 1, 10, 100, 154$ms).

The first of the ten snapshot images is the ballistic observation (as seen in Figure 4.1(A) for T=1ms, and Figure 4.2(A) for $T = T_{\text{critical}}$=154ms, generated using the formulas in Equations 2.4, 2.5), and the last is a heavily blurred diffuse observation (Figure 4.1(B) and Figure 4.2(B) generated using Equation 2.1). A single-snapshot version of the MPLE EM algorithm (i.e., with $k = 1$) is used to reconstruct the ballistic and diffuse observation images (Figure 4.1(C), 4.1(D) for T=1ms, and Figure 4.2(C), 4.2(D) for $T = T_{\text{critical}}$=154ms).

Algorithm 2 - MPLE EM Algorithm with Unknown Parameters

Initialize:

    1. Set iteration counter $j = 0$,

    2. $\lambda^{(0)}(m) = 1/n^2$, m=1,...,n^2,

    3. $X^{(i)}(\ell)$, $i = 1, \ldots, k$.

    4. Set $(\sigma^{(0)})^2 = 0.164 \left(\frac{ct^{(1)}}{\mu_s^m} \right)$, an elementary estimate of the sigma parameter based on system characteristics (from [10])

    5. Set $\Delta_\sigma = \frac{1}{2}(\sigma^{(0)})^2$,

E-Step: Set $P^{(i)} = P((\sigma^{(j)})^2 t^{(i)})$. Compute the conditional expectation of the complete data (c.f. [13]):

$$Z^{(j)}(\ell, m) = \sum_{i=1}^{k} X^{(i)}(\ell) \frac{\lambda^{(j)}(m) \, \alpha^{(i)} P^{(i)}(\ell, m)}{\sum_{m=1}^{n^2} \lambda^{(j)}(m) \, \alpha^{(i)} P^{(i)}(\ell, m)}$$

M-Step:

    1. Compute the expected photon emission counts via marginalization:

$$\mu^{(j)}(m) = \sum_{\ell=1}^{n^2} Z^{(j)}(\ell, m) \quad , \quad i = 1, \ldots, k$$

    2. Apply the multiscale complexity penalized denoising procedure [18] to $\mu^{(j)}$ to obtain updated iterate $\lambda^{(j+1)}$.

    3. Set $(\sigma^{(j+1)})^2 = \underset{\sigma^2 = \{(\sigma^{(j)})^2 - \Delta_\sigma, (\sigma^{(j)})^2, (\sigma^{(j)})^2 + \Delta_\sigma\}}{\text{argmax}} L(\sigma^2)$.

    4. Set $\Delta_\sigma = \frac{\Delta_\sigma}{2}$.

Repeat: Set $j = j + 1$. Repeat E- and M-steps until convergence and record

---

    The multiple snapshot EM algorithm (from Section 3 is used to fuse the data from all ten snapshots. Figure 4.1(E) and Figure 4.2(E) show the image reconstruction based on the multiple snapshot data given exact knowledge of all attenuation factors and blurring variances. Using the adaptive MLE scheme described in Section 3-3.3, the attenuation factors and blurring variance were jointly estimated along with original image λ, with the resulting image reconstruction shown in Figure 4.1(F) and Figure 4.2(F). Table 4.1 summarizes the reconstruction errors as compared with the original image λ. As expected, the combined oracle reconstruction performs best (in terms of pSNR), with the combined reconstruction with ML estimation of the gain and diffusion parameters close behind.

    The strength of the EM algorithm can be observed, as the EM reconstructed image will tend to the ballistic reconstruction at $T \geq T_{\text{critical}}$, while the EM reconstructed
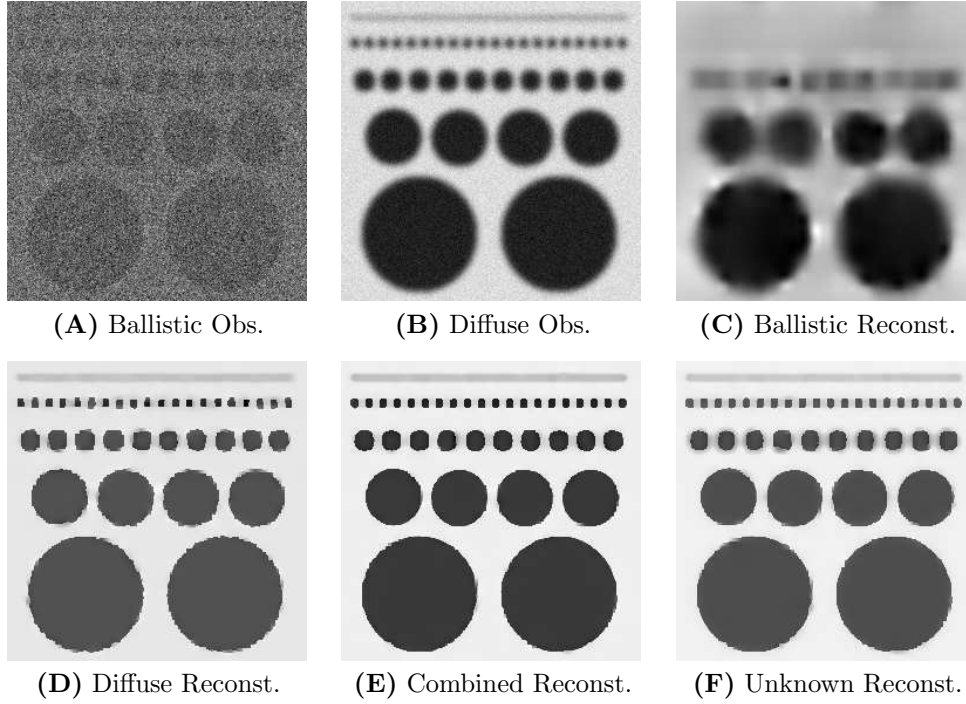
(A) Ballistic Obs.   (B) Diffuse Obs.   (C) Ballistic Reconst.

(D) Diffuse Reconst.   (E) Combined Reconst.   (F) Unknown Reconst.

FIG. 4.1. *EM Reconstruction with 50 iterations, 10 images, FOV = 100mm x 100mm x 10mm, d^t = 2.5 mm, T = 1ms*

T	Ballistic Reconst.	Diffuse Reconst.	Oracle	Unknown
1ms	34.26	39.33	40.93	40.43
10ms	38.09	39.21	41.08	40.60
100ms	41.79	39.26	44.17	43.85
154ms	42.31	39.35	44.88	44.66

TABLE 4.1
Summary of TRT image reconstruction Peak Signal-to-Noise Ratio (pSNR in dB).

image will tend to the diffuse reconstruction at $T < T_{\text{critical}}$. This follows the analysis in Section 2. The conservative nature of the Bonferroni Correction analysis can be seen in Table 4.1, as the ballistic observation reconstruction does outperform (in a pSNR sense) the diffuse observation reconstruction for acquisition times T shorter than the T_{critical}, although the T_{critical} value does appear to be of the correct order of magnitude.

5. Conclusions. This paper presented the resolution bounds and proposed a novel MLE reconstruction algorithm for TRT imaging. Using the decision-theoretic analysis approach, it is shown that for a given turbid medium, the smallest reliably resolved object (in terms of the width w^o) for both the conventional imaging and ballistic regimes, can be derived. The image reconstruction algorithm is based on a combination of the EM algorithm and Poisson denoising. Our simulation study demonstrates the potential of our approach, in particular indicating the added benefit of optimally fusing ballistic and diffuse photon data using the proposed EM algorithm.
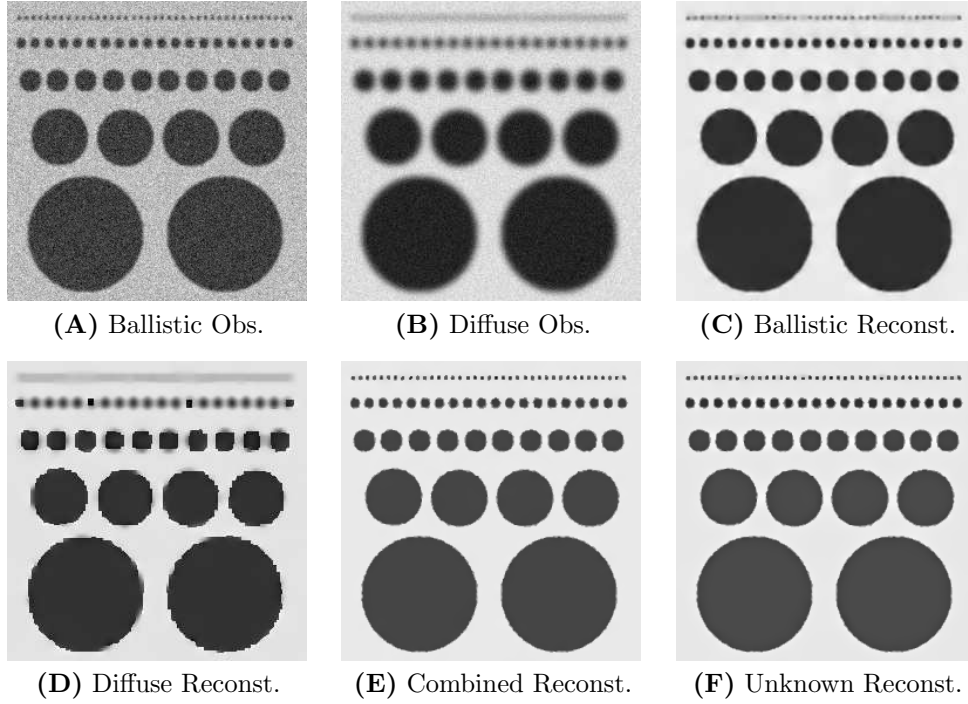
14

(A) Ballistic Obs.　　　**(B)** Diffuse Obs.　　　**(C)** Ballistic Reconst.

(D) Diffuse Reconst.　　**(E)** Combined Reconst.　　**(F)** Unknown Reconst.

Fig. 4.2. *EM Reconstruction with 50 iterations, 10 images, FOV = 100mm x 100mm x 10mm, $d^t = 2.5$ mm, $T = T_{critical} = 154ms$*

REFERENCES

[1] J. A. Moon, P. R. Battle, M. Bashkansky, R. Mahon, M. D. Duncan, and J. Reintjes, "Achievable spatial resolution of time-resolved transillumination imaging systems which utilize multiply scattered light," *Phys. Rev. E*, vol. 53, no. 1, pp. 1142–1155, Jan. 1996.

[2] R. Nossal A. H. Gandjbakhche and R. F. Bonner, "Resolution limits for optical transillumination of abnormalities embedded in tissues," *Medical Physics*, vol. 22, pp. 185–191, 1994.

[3] R. F. Bonner A. H. Gandjbakhche, G. H. Weiss and R. Nossal, "Photon path-length distributions for transmission through optically turbid slabs," *Phys. Rev. E*, vol. 48, pp. 810–818, 1993.

[4] J. C. Hebden, "Evaluating the spatial resolution performance of a time-resolved optical imaging system," *Med. Phys.*, vol. 19, pp. 1081–1087, 1992.

[5] A. J. Joblin, "Method of calculating the image resolution of a near-infrared time-of-flight tissue-imaging system," *Applied Optics*, vol. 35, pp. 752–757, Feb. 1996.

[6] J. C. Hebden and R. A. Kruger, "Transillumination imaging performance: Spatial resolution simulation studies," *Medical Physics*, vol. 17, pp. 41–47, Jan. 1990.

[7] Y. Chen, "Characterization of the image resolution for the first-arriving-light method," *Applied Optics*, vol. 33, pp. 2544–2552, May 1994.

[8] W. Cai, B. B. Das, F. Liu, M. Zevallos, M. Lax, and R. R. Alfano, "Time-Resolved Optical Diffusion Tomographic Image Reconstruction in Highly Scattering Turbid Media," *Proceedings of the National Academy of Science*, vol. 93, pp. 13561–13564, Nov. 1996.

[9] A.H. Hielscher, A.D. Klose, and K.M. Hanson, "Gradient-based iterative image reconstruction scheme fortime-resolved optical tomography," *Medical Imaging, IEEE Transactions on*, vol. 18, pp. 262–271, Mar. 1999.

[10] A. H. Gandjbakhche J. C. Hebden, "Experimental validation of an elementary forumla for estimating spatial resolution for optical transillumination imaging," *Med. Phys.*, vol. 22, pp. 1271–1272, 1995.

[11] M. A. Franceschini M. Kaschke P. M. Schlag K. T. Moesta S. Fantini, S. A. Walker, "Assessment

of the size, position, and optical properties of breast tumors in vivo by noninvasive optical methods," *Appl. Opt.*, vol. 37, pp. 1982–1989, 1998.

[12] F. J. Anscombe, "The transformation of poisson, binomial and negative-binomial data," *Biometrika*, vol. 35, pp. 246–254, 1948.

[13] Y. Vardi, L. Shepp, and L. Kaufman, "A statistical model for positron emission tomography," *J. Amer. Stat. Assoc.*, vol. 80, pp. 8–37, 1985.

[14] R. Willett and R. Nowak, "Multiscale poisson intensity and density estimation," *to appear in IEEE Trans. Info. Th.*, 2007, preprint at `www.ece.wisc.edu/~nowak/multiscale_poisson.pdf`.

[15] E. Kolaczyk and R. Nowak, "Multiscale likelihood analysis and complexity penalized estimation," *Ann. Stat.*, vol. 32, pp. 500–527, 2004.

[16] E. Kolaczyk and R. Nowak, "A statistical multiscale framework for poisson inverse problems," *IEEE Trans. on Image Proc.*, vol. 46, no. 5, pp. 1811–1825, 2000.

[17] R. Willett and R. Nowak, "Platelets: a multiscale approach for recovering edges and surfaces in photon-limited medical imaging," *IEEE Trans. Med. Imaging*, vol. 22, pp. 332–350, 2004.

[18] R. Willett, "Fast translation-invariant poisson image reconstruction," 2005, on-line at `www.ee.duke.edu/~willett/Research/FastTIHaar.html`.

ROBUST KERNEL REGRESSION FOR RESTORATION AND RECONSTRUCTION OF IMAGES FROM SPARSE NOISY DATA

Hiroyuki Takeda, Sina Farsiu, Peyman Milanfar

Department of Electrical Engineering, University of California at Santa Cruz
{htakeda,farsiu,milanfar}@soe.ucsc.edu

ABSTRACT

We introduce a class of robust non-parametric estimation methods which are ideally suited for the reconstruction of signals and images from noise-corrupted or sparsely collected samples. The filters derived from this class are locally adapted kernels which take into account both the local density of the available samples, and the actual values of these samples. As such, they are automatically steered and adapted to both the given sampling "geometry", and the samples' "radiometry". As the framework we proposed does not rely upon specific assumptions about noise or sampling distributions, it is applicable to a wide class of problems including efficient image upscaling, high quality reconstruction of an image from as little as 15% of its (irregularly sampled) pixels, super-resolution from noisy and under-determined data sets, state of the art denoising of images corrupted by Gaussian and other noise, effective removal of compression artifacts; and more.

Index Terms— Inverse problem, image reconstruction, piecewise polynomial approximation, nonlinear estimation

1. INTRODUCTION

Image processing methods have been exploited through the years to improve the quality of digital images. Many of the popular image processing tools have a limited scope of use; some can only be employed as denosing methods, while application of others are limited to upscaling regularly sampled data. Moreover, such methods estimate the underlying signal based on certain assumptions on data and noise models, a common example of which is modeling the noise as pure additive i.i.d. Gaussian. Although such limiting assumptions facilitate the design of optimal methods for a certain type of data, in real situations when the data and noise models do not faithfully describe the measured signal, the performance of such non-robust methods significantly degrades [1].

Classical parametric image processing methods rely on a specific model of the signal of interest, and seek to compute the parameters of this model in the presence of noise. In contrast to the parametric methods, non-parametric methods rely on the data itself to dictate the structure of the model, in which case this implicit model is referred to as *a regression function* [2]. We promote the use and improve upon a class of non-parametric methods called *kernel regression* [3], which generalizes some recently presented methods namely, *normalized convolution* [4], *bilateral filter* [5, 6], and *moving least-squares* [7].

The main advantage of the presented regression method is that it is a generic framework enabling direct use in a variety of applications, from single frame denoising to multi frame super-resolution [3]. Moreover, this method produces better and more stable results comparing to the state of the art methods in the literature, as it is robust to modeling errors and data outliers.

This paper is organized as follows. Section 2 is a brief introduction to the notion of adaptive kernel regression and the novel concept of using weighted l_1 norm penalty term in the kernel regression framework. Section 3 extends and generalizes the previous related methods to derive the details of the proposed robust regression method, focusing on appropriate choices for the kernel function. Simulation results are presented in Section 4, and Section 5 concludes this paper.

2. DATA-ADAPTED KERNEL REGRESSION

We treat the 2-D estimation problem where the measured data y_i at the position $\mathbf{x}_i = [x_{1i}, x_{2i}]^T$ is given by

$$y_i = z(\mathbf{x}_i) + \varepsilon_i, \quad i = 1, \cdots, P, \tag{1}$$

where $z(\cdot)$ is the (hitherto unspecified) regression function (i.e. an unknown image) to be estimated, P is the number of measured pixels, and ε_i's are the independent and identically distributed noise values (with otherwise no particular statistical distribution assumed).

While the specific form of $z(\cdot)$ may remain unspecified, if we assume that it is locally smooth to some order N, then in order to estimate the value of the function at any given point $\mathbf{x}$, we can rely on a generic local expansion of the function about this point. Specifically, if $\mathbf{x}$ is near the sample at $\mathbf{x}_i$, we have the N-term Taylor series

$$
\begin{aligned}
z(\mathbf{x}_i) &\approx z(\mathbf{x}) + \{\boldsymbol{\nabla} z(\mathbf{x})\}^T (\mathbf{x}_i - \mathbf{x}) \\
&\quad + \frac{1}{2}(\mathbf{x}_i - \mathbf{x})^T \{\boldsymbol{\mathcal{H}} z(\mathbf{x})\}(\mathbf{x}_i - \mathbf{x}) + \cdots \quad (2) \\
&= \beta_0 + \boldsymbol{\beta}_1^T (\mathbf{x}_i - \mathbf{x}) \\
&\quad + \boldsymbol{\beta}_2^T \operatorname{vech}\left\{(\mathbf{x}_i - \mathbf{x})(\mathbf{x}_i - \mathbf{x})^T\right\} + \cdots, \quad (3)
\end{aligned}
$$

where $\boldsymbol{\nabla}$ and $\boldsymbol{\mathcal{H}}$ are the gradient and Hessian operators respectively, and $\operatorname{vech}(\cdot)$ is the *half-vectorization operator* [2], which lexicographically orders the "lower-triangular" portion of a matrix into a column vector. Indeed the local approximation can be also built upon bases other than polynomials [8]

The above suggests that if we now think of the Taylor series as a local representation of the regression function, estimating the parameter β_0 can yield the desired (local) estimate of the regression function based on the data. Indeed, the parameters

$\{\boldsymbol{\beta}_n\}_{n=1}^{N}$ will provide localized information on the n-th *derivatives* of the regression function. Naturally, since this approach is based on *local* approximations, classical regression methods estimate the coefficients $\{\boldsymbol{\beta}_n\}_{n=0}^{N}$ from the data while giving the nearby samples higher weights than samples farther away ("geometric" weighting). However, it is also appropriate to weight samples based on their relative location with respect to a local edge ("radiometric" weighting), preforming the regression along and not across the edges, which is the basis of modern adaptive methods . A general formulation we propose, capturing this idea is to solve the following optimization problem:

$$\min_{\{\boldsymbol{\beta}_n\}_{n=0}^{N}} \sum_{i=1}^{P} \Big| y_i - \beta_0 - \boldsymbol{\beta}_1^T(\mathbf{x}_i - \mathbf{x}) -$$

$$\boldsymbol{\beta}_2^T \text{vech}\Big\{(\mathbf{x}_i - \mathbf{x})(\mathbf{x}_i - \mathbf{x})^T\Big\} - \cdots \Big|^m \mathsf{K}(\mathbf{x}_i - \mathbf{x}, y_i - y) \quad (4)$$

where $\mathsf{K}(\cdot)$ is the *kernel function* which penalizes both geometric and radiometric distances and will be described in detail in Section 3, and m is the penalizing parameter. To the best of our knowledge, all kernel regression based methods in the literature choose the penalizing parameter as $m = 2$, and therefore pose (4) as a weighted least-squares problem. In Section 4, we show that robustness with respect to the outliers can be significantly improved by exploiting other values for the penalizing parameter such as $m = 1$, which in effect incorporates a robust l_1 norm estimator [1] in the kernel regression framework. Furthermore, we propose novel ways to adopt the kernel.

Using the matrix form, the optimization problem (4) can be posed as weighted l_m norm:

$$\hat{\mathbf{b}} = \arg\min_{\mathbf{b}} \|\mathbf{y} - \mathbf{X}_{\mathbf{x}}\mathbf{b}\|_{\mathbf{W}_{\mathbf{x}}}^{m}, \quad (5)$$

where

$$\mathbf{y} = [y_1, y_2, \cdots, y_P]^T, \quad \mathbf{b} = \Big[\beta_0, \boldsymbol{\beta}_1^T, \cdots, \boldsymbol{\beta}_N^T\Big]^T, \quad (6)$$

$$\mathbf{W}_{\mathbf{x}} = \text{diag}\left[\mathsf{K}(\mathbf{x}_1 - \mathbf{x}, y_1 - y), \cdots, \mathsf{K}(\mathbf{x}_P - \mathbf{x}, y_P - y)\right], \quad (7)$$

$$\mathbf{X}_{\mathbf{x}} = \begin{bmatrix} 1 & (\mathbf{x}_1 - \mathbf{x})^T & \text{vech}^T\{(\mathbf{x}_1 - \mathbf{x})(\mathbf{x}_1 - \mathbf{x})^T\} & \cdots \\ 1 & (\mathbf{x}_2 - \mathbf{x})^T & \text{vech}^T\{(\mathbf{x}_2 - \mathbf{x})(\mathbf{x}_2 - \mathbf{x})^T\} & \cdots \\ \vdots & \vdots & \vdots & \vdots \\ 1 & (\mathbf{x}_P - \mathbf{x})^T & \text{vech}^T\{(\mathbf{x}_P - \mathbf{x})(\mathbf{x}_P - \mathbf{x})^T\} & \cdots \end{bmatrix}, \quad (8)$$

with "diag" defining the diagonal elements of a diagonal matrix. We use steepest descent to find the solution to this minimization problem:

$$\hat{\mathbf{b}}^{(n+1)} = \hat{\mathbf{b}}^{(n)} + \alpha\mathbf{X}_{\mathbf{x}}^T\mathbf{W}_{\mathbf{x}}\text{sign}\Big(\mathbf{y} - \mathbf{X}_{\mathbf{x}}\hat{\mathbf{b}}^{(n)}\Big)\odot\Big|\mathbf{y} - \mathbf{X}_{\mathbf{x}}\hat{\mathbf{b}}^{(n)}\Big|^{m-1}, \quad (9)$$

where α is a scalar defining the step size in the direction of the gradient, and $\odot$ is the element by element multiplication operator.

The order (N) of regression affects the complexity of the local approximation of the signal. In the non-parametric statistics literature, locally constant, linear and quadratic approximations (corresponding to $N = 0, 1, 2$ respectively) have been most widely considered [2]. In particular, choosing local constant estimation with $m = 2$, a locally linear adaptive filter is obtained,

which is known as the *Nadaraya-Watson Estimator* (NWE) [3]. In general, lower order approximates, such as NWE, result in smoother images (large bias and small variance) as there are fewer degrees of freedom. On the other hand over-fitting happens in regressions using higher orders of approximation, resulting in small bias and larger estimation variance. Note that, in the experiments of Section 4 we used the second order ($N = 2$) approximation.

3. KERNEL FUNCTION SELECTION

The choice of kernel function greatly affects the quality of reconstruction. In this section, first we briefly review the classic "non-adaptive" kernel function, and then generalize it to derive two adaptive kernel functions with superior performance.

3.1. Classic Kernel Function

In classic kernel regression, samples are weighted based only on their spatial distances to a sample of interest, which simplifies the kernel $\mathsf{K}(\cdot)$ in (4) to

$$\mathsf{K}(\mathbf{x}_i - \mathbf{x}, y_i - y) \equiv K_{\mathbf{H}_i}(\mathbf{x}_i - \mathbf{x}), \quad (10)$$

where $K_{\mathbf{H}_i}(\cdot)$ is defined as

$$K_{\mathbf{H}_i}(\mathbf{t}) = \frac{1}{\det(\mathbf{H}_i)} K\left(\mathbf{H}_i^{-1}\mathbf{t}\right), \quad (11)$$

which penalizes distance away from the local position where the approximation is centered. The 2×2 "smoothing" matrix $\mathbf{H}_i$ controls the strength of this penalty. The standard choice of the smoothing matrix is $\mathbf{H}_i = h\mu_i\mathbf{I}_2$, where μ_i is a scalar that captures the local density of data samples and h is the *global smoothing parameter*, extending the kernel to contain "enough" samples. As described in [3], in case of irregularly sampled data, it is reasonable to use smaller kernels in the areas with more available samples, whereas larger kernels are more suitable for the more sparsely sampled areas of the image. The choice of the particular form of the function $K(\cdot)$ is open, and may be selected as any symmetric function, which attains its maximum at zero such as Gaussian.

Since the shape of the classic kernels is independent of the radiometric (gray level) information, as described in [3], classic kernel based regression methods suffer from an inherent limitation due to the local linear action on the data. In what follows, we discuss extensions of the kernel regression method that enable this structure to have nonlinear, more effective, action on the data. The proposed adaptive kernel functions rely on not only the sample location and density, but also the radiometric properties of these samples. Therefore, the effective size and shape of the regression kernel are adapted locally to image features such as edges. This property is illustrated in Fig. 1, where the classical and adaptive kernel shapes in the presence of an edge are compared.

3.2. Bilateral Kernel Function

A simple and intuitive choice of the adaptive kernel $\mathsf{K}(\cdot)$ is to use separate terms for penalizing the spatial and radiometric distances. Indeed this is precisely the thinking behind the *bilateral* filter, introduced in [5, 6]. The bilateral kernel choice is then

$$\mathsf{K}(\mathbf{x}_i - \mathbf{x}, y_i - y) \equiv K_{\mathbf{H}_i}(\mathbf{x}_i - \mathbf{x})K_{h_r}(y_i - y), \quad (12)$$
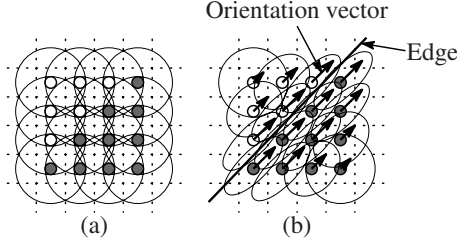
Fig. 1. Kernel spread in a uniformly sampled data set. (a) Kernels in the classic method depend only on the sample density. (b) Adaptive kernels elongate with respect to the edge.

where h_r is the radiometric smoothing scalar that controls the rate of decay, and $K_{\mathbf{H}_i}(\cdot)$ and $K_{h_r}(\cdot)$ are the spatial and radiometric kernel functions, respectively. In general, the application of bilateral kernel is limited to denoising problem, since the pixel value (y) at an arbitral position ($\mathbf{x}$) might not be available from data. This limitation, however, can be overcome by using an initial estimate of y by an appropriate interpolation technique [3]. Also, breaking $\mathsf{K}(\cdot)$ into spatial and radiometric terms as utilized in the bilateral case weakens the estimator performance since it limits the degrees of freedom and ignores correlations between positions of the pixels and their values. The following section provides a solution to overcome this drawback.

3.3. Steering Kernel Function

Based upon the earlier non-parametric framework, the filtering procedure we propose next takes the above ideas one step further. In particular, we observe that the effect of computing $K_{h_r}(y_i - y)$ in (12) is to implicitly measure a function of the local gradient estimated between neighboring values, and to use this estimate to weight the respective measurements. As an example, if a pixel is located near an edge, then pixels on the same side of the edge will have much stronger influence in the filtering. With this intuition in mind, we propose a two-step approach where first an initial estimate of the image gradients is made using some kind of gradient estimator (say the second order *classic* kernel regression method). Next, this estimate is used to measure the dominant orientation of the local gradients in the image. In a second filtering stage, this orientation information is used to adaptively "steer" the local kernel, resulting in elongated, elliptical contours spread along the directions of the local edge structure. With these locally adapted kernels, the denoising is effected most strongly along the edges, rather than across them, resulting in strong preservation of details in the final output. To be more specific, the steering kernel takes the form

$$\mathsf{K}(\mathbf{x}_i - \mathbf{x}, y_i - y) \equiv K_{\mathbf{H}_i^s}(\mathbf{x}_i - \mathbf{x}), \qquad (13)$$

where $\mathbf{H}_i^s$'s are the data-dependent full matrices which we call *steering* matrices. They are defined as

$$\mathbf{H}_i^s = h\mu_i \mathbf{C}_i^{-\frac{1}{2}}, \qquad (14)$$

where $\mathbf{C}_i$'s are (symmetric) covariance matrices based on the local gray-values. A good choice for $\mathbf{C}_i$ will effectively spread the kernel function along the local edges as shown in Fig. 1. It is worth noting that even if we choose a large h in order to have a strong denoising effect, the undesirable blurring effect which

would otherwise have resulted, is tempered around edges with appropriate choice of $\mathbf{C}_i$'s. With such steering matrices, for example, if we choose a Gaussian kernel, the steering kernel is mathematically represented as

$$K_{\mathbf{H}_i^s}(\mathbf{x}_i - \mathbf{x}) = \frac{\sqrt{\det(\mathbf{C}_i)}}{2\pi h^2} \exp\left\{ -\frac{(\mathbf{x}_i - \mathbf{x})^T \mathbf{C}_i (\mathbf{x}_i - \mathbf{x})}{2h^2} \right\}. \quad (15)$$

The local edge structure is related to the gradient covariance (or equivalently, the locally dominant orientation). In [3] we have shown that a convenient form of representing the covariance matrix, is to decompose it into three components as follows:

$$\mathbf{C}_i = \gamma_i \mathbf{U}_{\theta_i} \mathbf{\Lambda}_i \mathbf{U}_{\theta_i}^T, \qquad (16)$$

$$\mathbf{U}_{\theta_i} = \begin{bmatrix} \cos\theta_i & \sin\theta_i \\ -\sin\theta_i & \cos\theta_i \end{bmatrix}, \quad \mathbf{\Lambda}_i = \begin{bmatrix} \sigma_i & 0 \\ 0 & \sigma_i^{-1} \end{bmatrix}. \quad (17)$$

where $\mathbf{U}_{\theta_i}$ is the rotation matrix and $\mathbf{\Lambda}_i$ is the elongation matrix. Now the covariance matrix is given by the three parameters γ_i, θ_i and σ_i, which are the scaling, rotation, and elongation parameters, respectively and the effect of which are as follows. First, the initial circular kernel is elongated by the elongation matrix $\mathbf{\Lambda}_i$ with semi-minor and major axes given by σ_i and σ_i^{-1}, respectively. Second, the elongated kernel is rotated by the matrix $\mathbf{U}_{\theta_i}$. Finally, the kernel is scaled by the scaling parameter γ_i. We refer the reader to [3] for the details of estimating these parameters in an iterative fashion. We note that the presented formulation is close to the apparently independently derived normalized convolution formulation of [4].
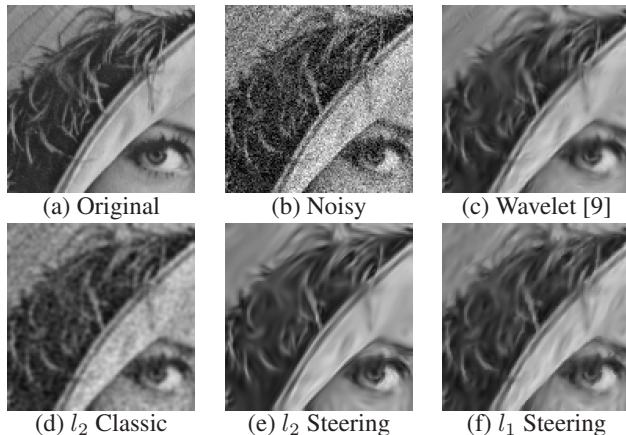
4. EXPERIMENTS

In this section we compare the performance of the proposed algorithm to other methods. We show that in presence of white Gaussian noise the proposed robust kernel regression method works as well if not better than the state of the art recent wavelet based denoising method of [9], and other popular methods. We also note that the wavelet method in general is computationally more efficient than the steering kernel method. However, in presence of other noise models (such as salt and pepper noise) while the performance of non-robust methods dramatically degrades, the proposed l_1 based robust method effectively removes the noise. The criterion for parameter selections in all the examples was to choose parameters which gave the best RMSE values.

In the first experiment, we added white Gaussian noise with standard deviation (STD) of 25 to the original image of Fig. 2(a) resulting in the noisy image of Fig. 2(b). Denoised images using the wavelet[1] method of [9]; classic kernel regression method ($m = 2$, $h = 1.33$), steering kernel regression method ($m = 2$, $h = 1.33$, 7 iterations initialized with l_2 classic), steering kernel regression method ($m = 1$, $h = 3$, 2 iterations initialized with l_1 classic) and corresponding Root Mean Square Error (RMSE) values are shown in Fig. 2(c)-(f), respectively.

In the second experiment we added 20% salt and pepper noise to the original image of Fig. 2(a) resulting in the noisy image of Fig. 3(a). Denoised images using a 3×3 median filter, wavelet method of [9], classic kernel regression method ($m = 2$,

---

[1]This result is produced by the software, available on http://decsai.ugr.es/~javier/denoise/index.html.

(a) Original   (b) Noisy   (c) Wavelet [9]

(d) l_2 Classic   (e) l_2 Steering   (f) l_1 Steering

Fig. 2. Gaussian noise removal experiment. Corresponding RMSE values for (b)-(f) are 25.0, 9.71, 11.36, 10.11, and 10.71, respectively.

(a)Noisy   (b) Median   (c) Wavelet [9]

(d) l_2 Classic   (e) l_2 Steering   (f) l_1 Steering
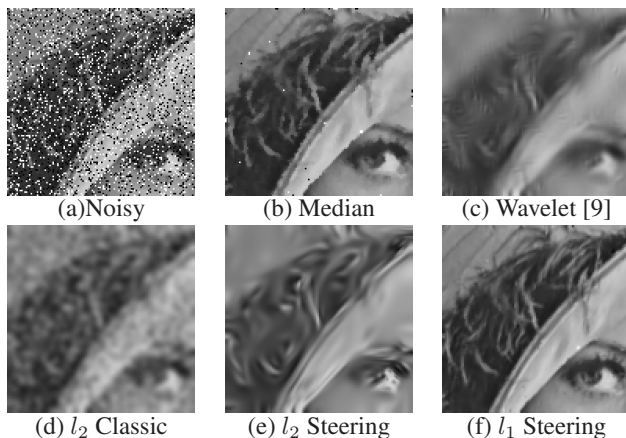
Fig. 3. Salt & pepper noise removal experiment. Corresponding RMSE values for Figures(a)-(f) are 63.84, 11.05, 21.54, 21.81, 21.06, and 7.14, respectively.

$h = 2.46$), steering kernel regression method ($m = 2$, $h = 2.25$, 20 iterations initialized with l_2 classic), steering kernel regression method ($m = 1$, $h = 2.25$, zero iteration initialized with l_1 classic) and corresponding RMSE values are shown in Fig. 3(b)-(f), respectively.

In our final experiment, we added white Gaussian noise with STD of 10 along with 5% salt and pepper noise to the original image of Fig. 2(a). Then, we randomly eliminated 85% of these noisy pixels, creating the sparse image of Fig. 4(a). Interpolated and denoised images using the Delaunay-spline smoother (refer to [3] for details), and the iterative steering kernel regression method ($m = 1$, $h = 3$, 0 iterations) and corresponding RMSE values are shown in Fig. 4(b)-(c), respectively.

5. CONCLUSIONS

In this paper we promoted, extended, and demonstrated kernel regression as a general framework for studying several efficient denoising and interpolation algorithms. To overcome the inherent limitations dictated by the linear filtering properties of the classic kernel regression methods, we introduced the non-linear data-adapted class of kernel regressors with superior performance. Fur-

(a) Subsampled   (b) Del. Spline   (c) l_1 Steering
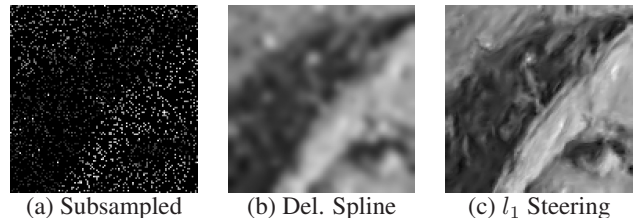
Fig. 4. Sparse-noisy image interpolation experiment. (a) is the input image with 85% of pixels removed, and further corrupted by adding Gaussian and salt and pepper noise. Reconstructed images using the Delaunay-spline smoother (RMSE=22.5), and the l_1 steering kernel regression (RMSE=17.5) methods, are shown in (b)-(c), respectively.

thermore, we achieved robustness with respect to outliers in data and noise model by incorporating the l_1 norm penalty in the kernel regression framework. Image deblurring is also an important issue in image reconstruction, and it is a part of our ongoing work within this framework.

6. REFERENCES

[1] S. Farsiu, D. Robinson, M. Elad, and P. Milanfar, "Fast and robust multi-frame super-resolution," *IEEE Trans. on Image Processing*, vol. 13, no. 10, pp. 1327–1344, Oct. 2004.

[2] D. Ruppert and M. P. Wand, "Multivariate locally weighted least squares regression," *The annals of statistics*, vol. 22, no. 3, pp. 1346–1370, Sept. 1994.

[3] H. Takeda, S. Farsiu, and P. Milanfar, "Kernel regression for image processing and reconstruction," submitted to IEEE Trans. on Image Proc., 2005, available at *http://www.soe.ucsc.edu/~milanfar*.

[4] T. Q. Pham, L. J. van Vliet, and K. Schutte, "Robust fusion of irregularly sampled data using adaptive normalized convolution," *EURASIP Journal on Applied Signal Processing*, 2006.

[5] C. Tomasi and R. Manduchi, "Bilateral filtering for gray and color images," *in Proc. IEEE Int. Conf. Computer Vision, New Delhi, India*, pp. 836–846, Jan. 1998.

[6] M. Elad, "On the origin of the bilateral filter and ways to improve it," *IEEE Trans. on Image Processing*, vol. 11, no. 10, pp. 1141–1150, Oct. 2002.

[7] N. K. Bose and N. Ahuja, "Superresolution and noise filtering using moving least squares," submitted to IEEE Trans. on Image Proc., 2005.

[8] W. Hardle, M. Muller, S. Sperlich, and A. Werwatz, *Nonparametric and Semiparametric Models*, Springer Series in Statistics. Springer, Berlin ; New York, 2004.

[9] J. Portilla, V. Strela, M. Wainwright, and E. P. Simoncelli, "Image denoising using scale mixtures of Gaussians in the wavelet domain," *IEEE Trans. on Image Proc.*, vol. 12, no. 11, pp. 1338–1351, Nov. 2003.

MULTI-SCALE STATISTICAL DETECTION AND BALLISTIC IMAGING THROUGH TURBID MEDIA

Sina Farsiu
Eye Research Center, Duke University
Durham, NC 27710, USA.
sina.farsiu@duke.edu

Peyman Milanfar
EE Department, University of California
Santa Cruz, CA 95064, USA.
milanfar@ee.ucsc.edu

ABSTRACT

We exploit recent advances in the physical design of fast optical systems which enable active imaging with "ballistic" light. In this modality, fast bursts of optical energy are propagated into a medium, and the ballistic component of light (which travels with minimal diffusive distortion) is detected after transmission through the target and the medium. To improve the detection rate of the common single pixel optimal detectors, we exploit sampling at a diversity of locations in space, and develop a multi-scale algorithm based upon the Generalized Likelihood Ratio Test (GLRT) framework, which takes advantage of the spatial correlation of nearby samples. Experimental results show that objects of different size and shape that are completely unrecognizable using the common single pixel detection techniques, are detectable with very high accuracy using the said multi-scale GLRT technique.

Index Terms— Ballistic Photons, Poisson Statistics, Adaptive Reconstruction, GLRT, Coherent Imaging, Turbid Media.

1. INTRODUCTION

High resolution imaging and detection of objects hidden in a turbid (scattering) medium have long been challenging and important problems with many industrial, military, and medical applications. While turbid media such as fog, smoke, haze, or body tissue are virtually transparent to radar range electromagnetic waves, the resolution of radar-based imaging systems is often insufficient for many practical applications. On the other hand, while the resolution of imaging systems using ultra short wavelengths (e.g. X-rays) is very desirable, there exist potential health hazards for imaging subjects and technicians alike.

As an alternative, imaging systems working in the optical/ infra-red spectrum range (laser scanners) are potentially able to produce high resolution images without the likely health hazards. Unfortunately, even a very thin and powerful collimated laser beam quickly diffuses as it travels in turbid me-

dia, similar to a car's headlights in fog. Therefore, a naive approach to optical imaging of objects hidden inside a turbid medium results in very blurry images, where targets are often indistinguishable from each other or the background.

Fortunately, the advent of the new tunable solid state lasers and ultra-fast optical detectors has enabled us to acquire high-quality images through turbid media where the resolution is only limited by diffraction. While many efficient imaging systems for capturing high-resolution images through turbid media have been proposed through the years, in this paper we mainly focus on ultra-fast time-gated or coherent imaging systems first introduced in [1].

Ultra-fast time-gated imaging is based on scanning the region of interest (ROI) point-by-point by sending very fast bursts of optical energy (laser pulses) and detecting the un-scattered (coherent) photons that have passed through the medium or reflected from the object. Although most of the photons in a laser pulse are either randomly scattered (losing their coherence) or absorbed as they travel through turbid media, across short distances, a few photons keep their coherence and pass through in straight lines without being scattered. These coherent photons are commonly referred to as the *ballistic* photons. Aside from the diffusive and ballistic photons, the photons that are slightly scattered retaining some degree of coherence are referred to as *snake* photons. Since the diffusive and ballistic photons have different path lengths, a femto-second laser pulse generator and an ultra fast time gate can be paired to separate the relatively slow (delayed) diffusive photons from the ballistic ones.

In what follows in this paper, we focus on studying and improving the performance of ballistic imaging systems. In Section 2, we describe a statistical model for the signal and noise in a typical ballistic imaging scenario. In Section 3, we study optimal single pixel detection systems and show that better detection rates are achievable using a multi-pixel detection technique which is based on the GLRT principle. Section 4 concludes this paper.

2. STATISTICAL MODEL FOR BALLISTIC IMAGING SYSTEMS

To have a better understanding of the practical issues involved in photon limited imaging via ballistic systems, let us con-

sider the imaging system described in [2], where the pumped Ti:Sapphire laser radiates 800nm pulses at a repetition rate of 1 kHz and an average power of 60mW. It is easy to show that the number of photons in each packet of energy (pulse) is computed as

$$I_0 = \frac{\text{Pulse Energy}}{\text{Photon Energy}} = \frac{\frac{60 \times 10^{-3} \times 1s}{1000}}{2.4830 \times 10^{-19}} = 2.4164 \times 10^{14}. \quad (1)$$

Due to the statistical nature of pulse propagation, as a laser beam travels through a diffusive medium, it is possible that some of the photons emerge without being scattered. By selecting these unscattered "ballistic" photons, and rejecting the scattered (diffused) ones, it is possible to obtain non-blurred images which are the sharp shadows of targets buried in the diffusive medium.

As expected, in relatively long distances, the number of detected ballistic photons is extremely small. Indeed, Beer's Law dictates an exponential relationship between the intensity of the transmitted light, and that of the ballistic component as

$$I_b = I_0 \exp(-\frac{d}{L}). \quad (2)$$

In this expression, I_0 is the number of the generated photons in one laser pulse before entering the turbid medium, I_b is the number of the ballistic photons which survive traveling through the medium, d is the distance traveled through the medium, $L = \frac{1}{\mu_t}$ is the mean free path (MFP) length (average distance photons travel before being scattered), and μ_t is the medium extinction factor. From (1) and (2), it is clear that for typical laser powers, it is fairly unlikely that any ballistic photon survive imaging scenarios where the ratio of d/L is larger than ~ 30 MFP.

The exponential drop in the number of received photons is the main prohibitive factor for using such high-resolution optical imaging systems across long distances. In such imaging scenarios, we are forced to rely on the less informative snake and diffusive photons. In [3], an accurate yet computationally manageable mathematical model for diffusive light propagation in turbid media is presented. An example of such imaging modality and experimental analysis is presented in [4] and some excellent literature surveys on the subject of diffusive imaging systems are presented in [5]. However, imaging systems that are able to time-resolve both ballistic *and* diffusive photons are rather expensive and are not discussed in this paper. Here, we focus on imaging systems that detect ballistic photons only. We exploit these statistical studies to improve the performance of ballistic imaging systems even in long distances where the signal power is weak.

It is important to note that due to the stochastic nature of photon propagation, I_b, calculated in (2), is merely the expected value of a Poisson random variable that estimates the number of surviving ballistic photons. Moreover, we assume that the received signal at the detector is contaminated with some amount of independent Poisson noise due to shot noise

and other degrading effects. Therefore, since the received signal at the detector is the unweighted summation of two Poisson random variables, it can be modeled as a Poisson random process with the following expected value

$$I = I_0 \, e^{-\mu_t d} + X_e = X_s + X_e,$$

where X_e and X_s are the expected values of the noise and signal, respectively.

Considering such imaging model, the probability density function of the received signal is given by

$$f(\underline{y}|X_{\underline{s}} + X_{\underline{e}}) = \prod_{k=1}^{N} \frac{e^{-(X_{e_k} + X_{s_k})}(X_{e_k} + X_{s_k})^{y_k}}{y_k!}, \quad (3)$$

where y_k is the k-th measurement, $\underline{y} = [y_1, y_2, ..., y_k, ..., y_N]^T$, $X_{\underline{e}} = [X_{e_1}, X_{e_2}, ..., X_{e_k}, ..., X_{e_N}]^T$, and $X_{\underline{s}} = [X_{s_1}, X_{s_2}, ..., X_{s_k}, ..., X_{s_N}]^T$. Note that the laser emits thousands of pulses per second and in practical implementation each spatial position is measured N times to improve the quality of estimation, and therefore the model in (3) is presented in the vector form. Since the average power of laser or the detector (and medium) characteristics are assumed not to be changing abruptly, to simplify notations, we assume that $X_{e_1} = X_{e_2} = ... = X_{e_N} = X_e$, and $X_{s_1} = X_{s_2} = ... = X_{s_N} = X_s$ (extension to the more general time-varying signal and noise case is straight forward).

3. OPTIMAL DETECTION OF OPAQUE OBJECTS IN TURBID MEDIA

In this section, assuming that the medium, laser, target, and turbid medium are accurately calibrated, we present the statistical optimal detectors of opaque objects hidden in a turbid medium.

3.1. Single Pixel Optimal Detection

In this subsection, we study the Neyman-Pearson (N.P.) type statistical test [6] for detecting opaque objects hidden in a turbid medium. In this test, we basically compare the likelihood of the following two scenarios:

- $\mathbb{H}_0$: An opaque object is hidden in the scattering medium, blocking the laser pulse (i.e. measurements contain only noise).

- $\mathbb{H}_1$: No opaque object exists in the propagation line of the laser pulse (i.e. measurements contain noise plus attenuated laser pulse).

The probability density function of these two scenarios when such tests are repeated N times are given by

$$\mathbb{H}_0 \quad : \quad f(\underline{y}|X_e) = \prod_{k=1}^{N} \frac{e^{-(X_e)}(X_e)^{y_k}}{y_k!},$$

$$\mathbb{H}_1 \quad : \quad f(\underline{y}|X_s + X_e) = \prod_{k=1}^{N} \frac{e^{-(X_e + X_s)}(X_e + X_s)^{y_k}}{y_k!}, \quad (4)$$

and therefore the N.P. test is derived by comparing the log likelihood ratio to a threshold as:

$$\log \prod_{k=1}^{N} \left(\frac{\frac{e^{-(X_e+X_s)}(X_e+X_s)^{y_k}}{y_k!}}{\frac{e^{-X_e}(X_e)^{y_k}}{y_k!}} \right) \underset{\mathbb{H}_0}{\overset{\mathbb{H}_1}{\gtrless}} \gamma$$

$$\Longrightarrow \sum_{k=1}^{N} y_k \underset{\mathbb{H}_0}{\overset{\mathbb{H}_1}{\gtrless}} \frac{\log(\gamma) + NX_s}{\log(\frac{X_e+X_s}{X_e})} = \gamma'. \quad (5)$$

Noting that $\sum_{k=1}^{N} y_k$ is yet another poisson process, the probabilities of false alarm (P_{FA}) and detection (P_D) are computed as

$$P_{FA} = P\{\sum_{k=1}^{N} y_k > \gamma' | \mathbb{H}_0\} = 1 - \sum_{k=0}^{\gamma'} \frac{e^{-NX_e}(NX_e)^k}{k!}, \quad (6)$$

$$P_D = 1 - \sum_{k=0}^{\gamma'} \frac{e^{-NX_e - NX_S}(NX_e + NX_S)^k}{k!}. \quad (7)$$

3.2. Multi-pixel GLRT Detection

As explained in Section 1, in ballistic imaging the field of view is scanned at multiple points to create a 2-D image of the objects in the ROI. In this section, we propose an effective algorithm that exploits the spatial correlation of the nearby samples in a multi-pixel imaging scenario to improve on the performance of the single pixel optimal detectors developed in the previous section.

The proposed multi-pixel detection technique generalizes the single pixel detection techniques and preforms optimal tests on "super-pixels", which are the collective intensities of a set of neighboring pixels in size and shape of the hidden objects. However, since in general the size and shape of the hidden objects is not known *a priori*, we develop a GLRT based algorithm that simultaneously tests the existence, and estimates the shape and size of the objects hidden in turbid media.

The outline of the proposed GLRT algorithm is illustrated by an example in Fig.1. First, for a given (fixed) false alarm rate the optimal detectors developed in the previous section are exploited to test the existence or absence of objects at each individual pixel. As an illustrative example, this test is applied to the central pixel (shaded) of Fig.1(a), where the measured pixel value (0.4) is compared to the N.P. test threshold (0.5). Of course, the greater the distance of the measurement from the threshold, the more confident we are in the accuracy of the test result. Next, we integrate the gray-level values of all immediate neighboring pixels, and in effect consider them as one "super-pixel", as illustrated in Fig.1(b). Since the false alarm rate is fixed for all scales, the decision threshold is different than the threshold calculated in the previous step, which is recalculated based on the grayvalue of the super-pixel. In the next steps, we repeat this process by fixing the
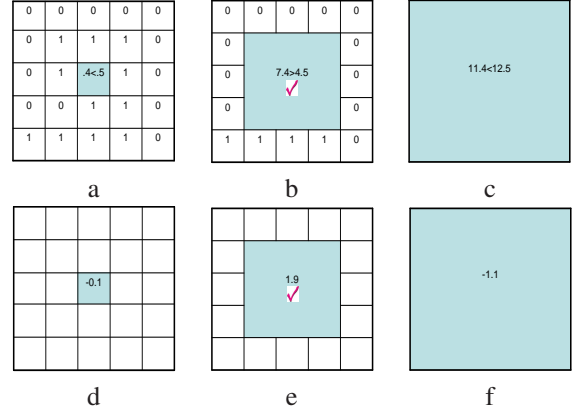
Fig. 1. An illustrative example showing the outline of the proposed multi-scale GLRT algorithm. a: Scale 1 measurement. b,c: Scales 2,3 super-pixels, respectively. d-f: Confidence values for scales 1-3, respectively. The check marked second scale gives the highest confidence value for the central pixel.

false alarm rate and considering larger neighborhoods. The generalized N.P. test for these steps is formulated as follows

$$y_{m,l}^{scale} \underset{\mathbb{H}_0}{\overset{\mathbb{H}_1}{\gtrless}} \frac{\log(\gamma^{scale}) + N_{scale}X_s}{\log(\frac{X_e+X_s}{X_e})}, \quad (8)$$

where $y_{m,l}^{scale}$ is the summation of the pixel values in the $N_{scale} = N(2 \times scale - 1)^2$ pixels neighborhood around the pixel $[m, l]$ (note that other neighborhood expansion strategies with different shape and size can be also considered in this algorithm). Our confidence in the decision made on each scale is defined as the distance between the summation of measurements in the super-pixel and that of the threshold set by the GLRT:

$$\text{Confidence}_{m,l}^{scale} = |y_{m,l}^{scale} - \frac{\log(\gamma^{scale}) + N_{scale}X_s}{\log(\frac{X_e+X_s}{X_e})}|. \quad (9)$$

Note that the optimal scale is not unique for all pixels, as finer scales are more suitable for pixels located on the texture or edge areas, and coarser scales are more suitable for the pixels located in flat areas. Therefore, we decide on the presence or absence of the object at a particular pixel based on the test result of the scale that shows the highest confidence value. The memory requirement of this technique is independent of the maximum scale number, since we only need to keep the original image, the last estimated image and the corresponding confidence values.

To have a better understanding of the proposed multi-scale GLRT technique and its performance, we set up an illustrative controlled imaging scenario. Fig.2(a) shows ideal (noiseless and deterministic) image of objects of different size and shape. To depict an experiment at the limit distance where the signal of interest is very weak, we consider an imaging scenario where the average number of received ballistic photons

for each pixel is one photon. Fig.2(b) shows such Poissonian random signals (yet free of noise effects). Detection of such signals becomes more difficult when we consider the system noise as illustrated in Fig.2(c), where the Poisson noise variance is 40. Fig.2(d) is an image reconstructed by implementing the point-by-point single pixel detection techniques, considering a false alarm rate of 0.00125, where none of the objects are correctly identified. On the other hand, Fig.2(e) is the result of exploiting the multi-scale GLRT technique, showing a considerably more accurate detection of such objects.

Fig.2(f) illustrates the scale from which each pixel in the final image of Fig.2(e) is selected. Note that as expected, the pixels in the flat area are selected from the coarser scales, while the pixels on the edge areas are selected from the finer scales. Fig.2(g) shows the confidence in the detection result (9) with respect to the corresponding pixels. This figure shows higher confidence levels in the flat, and less confidence in the edge areas. Also, in Fig.2(g) we see that the area with the lowest confidence is the place where most misclassifications happen. This is good news, since to increase the detection rate, we may opt to do a second (and very quick) round of scans, sampling only on these very low-confidence regions. In Fig.2(h), we plot the misclassification rates at each scale (blue line), and compare it to the overall multi-scale one (red line). These experimental plots show that the performance of the proposed pixelwise GLRT technique (depending on the noise level) is either very close or even better than the best fixed scale technique. In Fig.2(i), the performance of single pixel detection technique is compared with the multi-scale ones via their corresponding ROC curves (with 25 Monte Carlo experiments). Once again, the multi-scale technique shows the best or close to the best performance.

4. CONCLUSION

In this paper, we studied a technique for improving the quality of the ballistic images captured through turbid media.The novelty of this paper is in combining the recent advances in optical science with the novel image processing and statistical signal processing techniques.

5. REFERENCES

[1] K.M. Yoo and R.R. Alfano, "Time-resolved coherent and incoherent components of forward light scattering in random media," *Optics Letters*, vol. 15, no. 6, pp. 320–322, Mar. 1990.

[2] M. E. Zevallos, S. K. Gayen, M. Alrubaiee, and R. R. Alfano, "Time-gated backscattered ballistic light imaging of objects in turbid water," *Applied Physics Letters*, vol. 86, pp. 011115–1–011115–3, Jan. 2005.

[3] D. Contini, F. Martelli, and G. Zaccanti, "Photon migration through a turbid slab described by a model based on
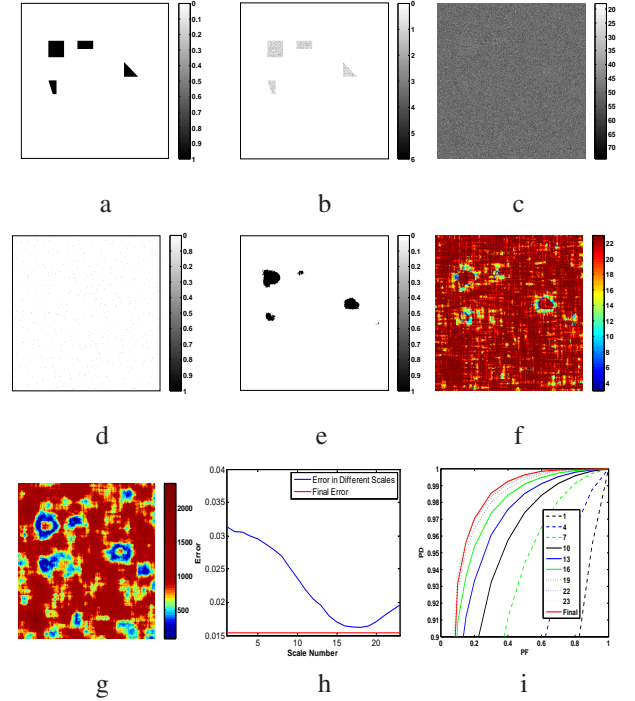
Fig. 2. An ideal deterministic and noise free image of four objects of different size and shapes is shown in (a). (b) shows the corresponding image as a Poissonian noise free stochastic signal, with $X_s = 1$. (c) is the result of adding Poisson noise ($X_e = 40$) to (a). (d) is the result of the single pixel detection, and (e) is the result of the proposed multi-scale detection technique. (f) shows an image that corresponds to the selected scales for the image shown in (e), and (g) shows the corresponding confidence values. (h) shows the misclassification probability in different scales. ROC plots for the proposed multi-scale detection scenario are shown in (i). The numerical labels "1,4,...,23", correspond to the scale at which detection tests are performed, and the plot labeled "Final" represents the performance of the proposed multiscale (fused) technique.

diffusion approximation. i. theory," *Applied Optics*, vol. 36, no. 19, pp. 4587–4599, July 1997.

[4] W. Cai, S. K. Gayen, M. Xu, M. Zevallos, M. Alrubaiee, M. Lax, and R. R. Alfano, "Optical tomographic image reconstruction from ultrafast time-sliced transmission measurements," *Appl. Opt.*, vol. 38, no. 19, pp. 4237–4246, July 1999.

[5] A.P. Gibson, J.C. Hebden, and S.R. Arridge, "Recent advances in diffuse optical imaging," *Physics in Medicine And Biology*, vol. 50, pp. R1–R43, Feb. 2005.

[6] S. M. Kay, *Fundamentals of statistical signal processing:detection theory*, vol. II, Prentice-Hall, Englewood Cliffs, New Jersey, 1998.

A DECISION-THEORETIC APPROACH TO TRANSILLUMINATION IMAGING IN BIOLOGICAL MEDIUMS

Brian Eriksson and Robert Nowak

University of Wisconsin - Madison

ABSTRACT

The tradeoffs between ballistic imaging (time-gated imaging of first-arrival, unscattered photons) and conventional imaging for resolving tumors in biological scattering media are examined. For ballistic imaging, closed form expressions are derived to characterize the resolvability using five degrees of freedom (laser intensity, scattering coefficient, thickness of medium, false alarm rate, and number of observations). For conventional imaging, a numerical approximation is used to find the asymptotic resolution using the scattering and absorption coefficients of the medium. Using the characterizations of both approaches, a decision-theoretic approach to determining the minimum resolvable object size is developed, which provides clear guidelines as to when time-gated ballistic imaging methods offer advantages over conventional imaging. The theoretical predictions are validated through a realistic simulation of tumors in breast tissue.

Index Terms— Transillumination Imaging, Decision Theoretic, Resolution, Ballistic

1. INTRODUCTION

Ballistic photon imaging is a promising methodology for studying highly scattering media such as human tissue. Recent advances allow for the time-gating of early arriving photons introduced into a scattering (turbid) medium. This allows for the ability to separately detect unscattered or ballistic photons that exit the medium. Due to the lack of scattering, these photons will retain the spatial information of the medium. A tradeoff occurs, as the number of ballistic photons decays exponentially fast as the thickness/depth of the turbid medium increases. This results in an observation from ballistic photons that offers a high resolution but low SNR.

The basic imaging model considered here is a single laser point source and a single photon detector placed on either side of a turbid (scattering) medium. We assume that the source and detector can be positioned at arbitrary points, to allow probing through any desired set transects through the medium. A turbid medium can be considered any scattering material, and in this specific analysis we assume it to be

a homogeneously scattering section of human tissue. This scattering material will be parameterized by the number of scatters per unit length (μ_s^m), the fraction of absorptions per length (μ_a^m), and the length of the medium (d^m). At certain points between the source and detector in the medium there may exist an occluder of interest. The occluders, which are assumed to be opaque, represent tumors embedded in tissue for a biomedical imaging application. We assume that the occluders are located at the mid-point of the medium being probed, as this is the point in the medium where the variance of the scattering will be at a maximum [1,2]. To completely define the environment, one must take into consideration the scattering properties of the occluding tumor (μ_a^t, μ_s^t), and the physical properties of the occluding tumor (depth = d^t, width = w^t).
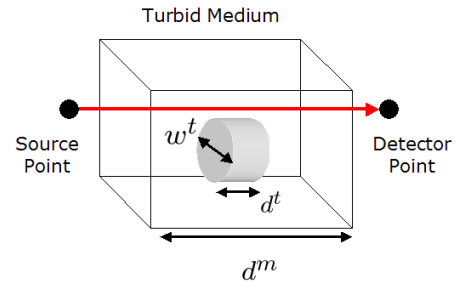

Figure 1. Turbid Medium Model Example

To create an observation of the environment, the source and detector pair will make a raster scan of the field of view to create an estimated cross-section of the environment. Our goal is to find, given the parameters of the medium and the occluder, lower bounds on the width and depth of the occluder (d^t, w^t) that can be reliably resolved in the medium. Two imaging regimes will be considered, the ballistic regime where only early arriving photons are detected using high-speed gating mechanisms, and the conventional imaging regime, where all the photons arriving at the detector are utilized (i.e., no time-gating). The advantage of the ballistic photons is that they are not scattered, providing very high spatial resolution. The limitation of ballistic imaging is that very few photons will propagate through the medium without scattering, resulting in a very poor signal-to-noise ra-

tio (SNR). Conventional imaging uses all photons (scattered and unscattered) and thus provides a complementary trade-off (lower resolution but higher SNR). A decision-theoretic technique is then derived to determine which technique should be used for a given parameterized scattering medium in order to resolve small tumors.

2. BALLISTIC ANALYSIS

The ballistic imaging regime consists of probing points in a Field-of-View (FOV) and acquiring a count of the number of ballistic photons that arrive at each point in the FOV. These photons traverse in a straight line-of-sight between the source point and the detector, and therefore retain the spatial characteristics of the occluding objects in the turbid medium. Due to their direct line-of-sight characteristics, these photons will travel the shortest length and will arrive at the detector before any scattering photons. In order to collect only ballistic photons, time-gating is performed to restrict the observation to only early arriving photons (i.e. photons with no scattering events). If a perfect occluder is in the line-of-sight between the source and detector, then no ballistic photons will arrive at the detector. Therefore, the detection of ballistic photons indicates a "clear" line-of-sight and the absence of a tumor along the given transect. However, a problem occurs – as the turbidity of the medium increases, the less likely a photon is to arrive at the sensor having no scattering events. As a consequence, the total number of ballistic (non-scattering) photons for a medium might be very low. In addition, stray "noise" photons from other sources corrupt the observed signal, resulting in an observation that has high spatial resolution, but low SNR.

2.1. Ballistic Imaging - Single Point

The detected time-gated photons are ballistic photons from the source or stray "noise" photons arriving during the time-gate interval from other ambient light sources. The problem of determining whether or not a tumor lies along the line-of-sight can be cast as a statistical hypothesis test, as follows. Given a received photon count X at the sensor, one must choose between two possible situations. The first situation, is that no occluding tumors exist in the path between the laser and the sensor ($\mathcal{H}_0$). The alternative is that there is an occluding tumor along the line-of-sight between the laser and the sensor ($\mathcal{H}_1$). Tumors can be considered to be significantly more turbid scattering medium than the healthy tissue [3], and therefore the detector will collect an attenuated number of ballistic photons (compared to $\mathcal{H}_0$) along with the noise photons.

We define the number of noise photons that will arrive at the detector as $\mathcal{P}(t\lambda_0)$ (where $X \sim \mathcal{P}(\lambda)$ is a Poisson distributed random variable with mean $= \lambda$, and where t is the duration of photon acquisition time-gating). The ballistic pho-

tons traveling through only healthy tissue will be $\mathcal{P}\left(t\lambda_{L(tissue)}\right)$ (where $\lambda_{L(tissue)} = \lambda_L\left(\exp\left(-\mu^m d^m\right)\right)$), while the ballistic photons traveling through both healthy tissue and tumor will be $\mathcal{P}\left(t\lambda_{L(tissue+tumor)}\right)$ (where $\lambda_{L(tissue+tumor)} = \lambda_L\left(\exp\left(-\left(\mu^m d^m - \mu^m d^t + \mu^t d^t\right)\right)\right)$, with λ_L is the expected number of photons sent through the medium by the laser per unit time, $\mu^m = \mu_s^m + \mu_a^m$, and $\mu^t = \mu_s^t + \mu_a^t$).

This can be expressed as a hypothesis test with the null hypothesis (only tissue) defined as $\mathcal{H}_0 : X \sim \mathcal{P}\left(t\left(\lambda_0 + \lambda_{L(tissue)}\right)\right)$ and the true hypothesis (tissue and tumor) defined as $\mathcal{H}_1 : X \sim \mathcal{P}\left(t\left(\lambda_0 + \lambda_{L(tissue+tumor)}\right)\right)$. As the mean of the Poisson distribution grows, the probability distribution tends to a Gaussian. Averaging repeated trials (i.e. averaging of multiple laser pulses) therefore results in a Gaussian distributed statistic. Using the Anscombe Transformation [4], we obtain the following relationship (where $X \sim \mathcal{N}\left(\mu, \sigma^2\right)$ is a gaussian distributed random variable with mean $= \mu$ and variance $= \sigma^2$) then $X \sim \mathcal{P}(\lambda) \Rightarrow 2\sqrt{X + \frac{3}{8}} \sim \mathcal{N}\left(2\sqrt{\lambda}, 1\right)$. Defining a new variable representing the Anscombe Transformed statistic $X' = 2\sqrt{X + \frac{3}{8}}$ the hypothesis test becomes:

$$\mathcal{H}_0 : X' \sim \mathcal{N}\left(2\sqrt{t\left(\lambda_0 + \lambda_{L(tissue)}\right)}, 1\right) \quad (1)$$

$$\mathcal{H}_1 : X' \sim \mathcal{N}\left(2\sqrt{t\left(\lambda_0 + \lambda_{L(tissue+tumor)}\right)}, 1\right) \quad (2)$$

The decision test is now defined as $\left(X' \lessgtr_{\mathcal{H}_0}^{\mathcal{H}_1} \gamma'\right)$. Using the test, a user-specified false alarm rate (α) determines the value of the threshold (γ') such that $P\left(X' < \gamma' \mid \mathcal{H}_0\right) \leq \alpha$.

2.2. Ballistic Imaging - K Points

The problem now is modified to trying to image a fixed square array of ($\sqrt{K}$ x $\sqrt{K}$) points. This results in a multiple hypothesis testing problem (K tests), and for large K it is difficult to control the overall probability of false-alarm (i.e., false tumor detection at one or more point). A standard technique is to increase the acquisition time (t) for each point, but by the setup of the problem increasing t will increase not only the number of signal photons, but also the number of noise photons. This puts a lower bound on the SNR of the observation. To boost the SNR, one could use spatial aggregation by averaging over a number of observation points. This modifies the problem to averaging neighborhoods of points in an area measuring $\sqrt{M}$ x $\sqrt{M}$, $M < K$, effectively reducing the spatial resolution of the detection map (image). By decreasing the spatial resolution, this also decreases the variance at each point, modifying the decision test to:

$$\mathcal{H}_0 : X' \sim \mathcal{N}\left(2\sqrt{t\left(\lambda_0 + \lambda_{L(tissue)}\right)}, \frac{1}{M}\right) \quad (3)$$

$$\mathcal{H}_1 : X' \sim \mathcal{N}\left(2\sqrt{t\left(\lambda_0 + \lambda_{L(tissue+tumor)}\right)}, \frac{1}{M}\right) \quad (4)$$

This test is under the assumption that the averaging window will contain either no occluder points or all occluder points. In reality, the averaging filter will result in an observed point: $X'' \sim \mathcal{N}\left(\rho E\left[X'|\mathcal{H}_0\right] + (1-\rho)E\left[X'|\mathcal{H}_1\right], \frac{1}{M}\right)$ (where ρ is the fraction of the window containing non-occluders). Our goal is to find the lower bound on the value of M that will guarantee an overall false alarm rate of less than α, we consider the ideal case (all occluders or non-occluders) in our calculations in order to obtain closed-form solutions.

2.2.1. Bonferroni Correction

The Bonferroni Correction approach is a conservative method of controlling the false alarm rate for a detection problem under multiple i.i.d. tests [5]. The correction adjusts the threshold for each individual test in order to satisfy a lower (per test) false alarm rate value ($\frac{\alpha}{K}$) such that each of the fixed number K-points in the array (and M-point averaging filter) satisfies $\left(P\left(X < \gamma'|H_0\right) \leq \frac{\alpha}{K}\right)$. With $\Phi(x)$ as the cumulative distribution function of the $\mathcal{N}(0,1)$ density at the point x, this results in $\left(\gamma' \leq \frac{1}{\sqrt{M}}\Phi^{-1}\left(\frac{\alpha}{K}\right) + 2\sqrt{t\left(\lambda_0 + \lambda_{L(tissue)}\right)}\right)$. To give a satisfactory observation, we also bound the miss probability for detecting a ballistic photon by the same modified value ($\frac{\alpha}{K}$) such that $\left(P\left(X > \gamma'|H_1\right) \leq \frac{\alpha}{K}\right)$. Using the miss bounds, we determine the lower bound on the necessary averaging window size (M) to image a fixed K-point array.

$$M \geq \left(\frac{\frac{1}{2\sqrt{t}}\left(\Phi^{-1}\left(1 - \frac{\alpha}{K}\right) - \Phi^{-1}\left(\frac{\alpha}{K}\right)\right)}{\left(\sqrt{(\lambda_0 + \lambda_{tissue})} - \sqrt{(\lambda_0 + \lambda_{tissue+tumor})}\right)}\right)^2 \quad (5)$$

The minimum width of the occluding tumor ($w_{ballistic}^t$) that can be reliably resolved for a given parameterized turbid medium can now be derived. Using the lower bound for M found in Eqn 5, we can solve for the lower bound on the width using $w_{ballistic}^t = \sqrt{\frac{FOV*M}{K}}$. Due to M being a function of the tumor depth d^t, we can also numerical solve for the minimum tumor depth possible for a parameterized system.

2.2.2. False Discovery Rate

While the closed form resolution bounds for the Bonferroni Correction were derived, it is a very conservative approach and may obtain a poor reconstruction in order to avoid false alarm errors. To improve the reconstruction, we can increase the resolution by decreasing the M value (averaging filter size), and then use a modified False Discovery Rate (FDR) algorithm [6] for the multiple point test. To obtain the threshold, take the K number of observed signal values and determine the p-value (p_i) under each observed value (X'_i).

$$
\begin{aligned}
p_i &= P\left(x < X'_i \mid \mathcal{H}_0\right) &(6)\\
&= \Phi\left(\sqrt{M}\left(X'_i - 2*\sqrt{t\left(\lambda_0 + \lambda_{L(tissue)}\right)}\right)\right) &(7)
\end{aligned}
$$

To choose the FDR threshold (γ'), take the threshold corresponding to the largest index (n) such that $p_n \leq 1 - (1-\alpha)^{\frac{1}{K+1-n}}$. In practice, False Discovery Rate will result in a less conservative reconstruction, but it cannot be analyzed to obtain closed form bounds.

3. CONVENTIONAL IMAGING ANALYSIS

In the conventional imaging regime, there is no time-gating mechanism and all the photons that reach the detector over a long acquisition time will be observed (acquisition time $\gg \left(\frac{d}{c}\right)$ = direct line-of-sight flight time). Therefore, a large number of photons sent through the medium will be collected by the detector. A problem occurs here, too — while the signal-to-noise ratio is high due to the large number of photons, the average number of scattering events on each photon collected will also be high. As the number of scattering events increases for a photon, the less the photon will retain the spatial resolution of the occluding object. The lack of spatial information results in a blurred observation. Using random walk theory in [2], it is possible to solve for the minimum width of an occluding tumor that is reliably resolved using the conventional imaging regime. The width is found using the photon mean-time-of-flight $\langle\Delta t\rangle$, which can be numerically solved as a function of the parameters of the medium (μ_s^m, μ_a^m). The minimum width is equal to $w_{conv}^t = 0.408\left(\frac{\langle\Delta t\rangle c}{\mu_s^m}\right)^{\frac{1}{2}}$.
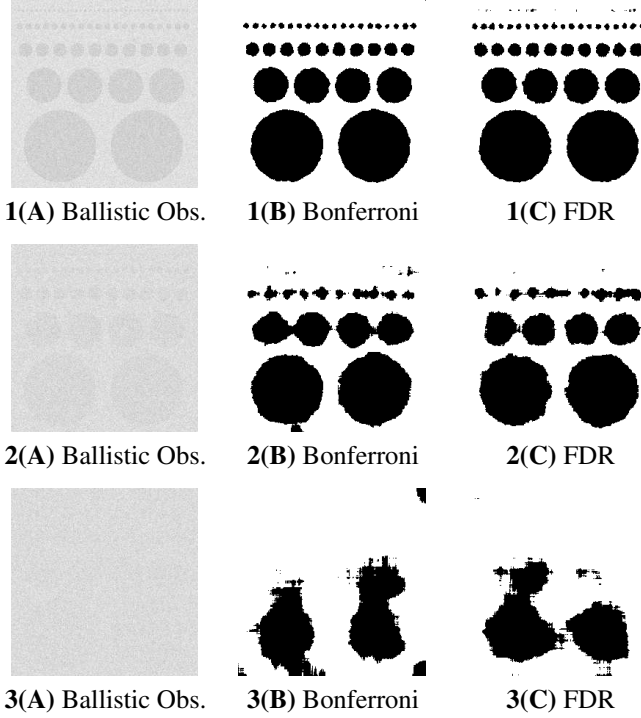
4. OPTIMAL RESOLUTION TRADEOFFS

Ideally, one should choose the imaging system (ballistic or conventional) that reliably resolves the smallest possible object ($w^t = \min\left(w_{conv}^t, w_{ballistic}^t\right)$). The decision test $w_{conv}^t \underset{ballistic}{\overset{conv}{\lessgtr}} w_{bal}^t$, using the minimum resolvable sizes derived above becomes: $0.408\left(\frac{\langle\Delta t\rangle c}{\mu_s^m}\right)^{\frac{1}{2}} \underset{ballistic}{\overset{conv}{\lessgtr}} \sqrt{\frac{FOV*M}{K}}$. Using the lower bound of M from Eqn. 5, one can solve for the critical distance ($d^m = d_{critical}$), the maximum distance at which ballistic still offers superior resolution relative to conventional imaging.

4.1. Simulation Study - Breast Tissue

We now present a simulation study of imaging malignant breast tissue through healthy breast tissue. For this simulation, a 10cm x 10cm FOV (as a K=256^2 point array) is defined with circular occluding objects of diameter 0.2 cm, 0.4 cm, 0.8 cm, 2.0 cm, and 4.0 cm. From [3], we use the scattering and absorption coefficients of the two tissue types. Using a specified depth of the occluding tumor (d^t=0.25cm) and false alarm rate ($\alpha = 0.05$), we solve for the minimum width of the occluding tumor under the ballistic observation

with Bonferroni Correction testing ($w_{bal(bon)}^t$, along with the size of the averaging filter M), and the conventional imaging observations minimum occluding width (w_{conv}^t). To obtain a better observation of the model, a higher resolution ($w_{bal(fdr)}^t = \frac{3}{4} w_{bal(bon)}^t$) observation using the False Discovery Rate (FDR) method was also simulated. Three medium distances ($d^m = 1.6, 1.7, 1.8$ cm) are used to show the effects that the distance of the medium has on the number of ballistic photons received.

1(A) Ballistic Obs.	1(B) Bonferroni	1(C) FDR
2(A) Ballistic Obs.	2(B) Bonferroni	2(C) FDR
3(A) Ballistic Obs.	3(B) Bonferroni	3(C) FDR

Figure 2. Simulations under FOV = 10x10cm, $d^t = 0.25$ cm (1) $d^m = 1.6$ cm, (2) $d^m = 1.7$ cm, (3) $d^m = 1.8$ cm

d^m	M	$w_{bal(bon)}^t$	w_{conv}^t	$pSNR_{bon}$	$pSNR_{fdr}$
1.6	31	0.217	1.012	15.52	16.34
1.7	301	0.678	1.04	11.27	11.33
1.8	3195	2.21	1.07	5.73	6.21

Table 1. Derived properties of the malignant/healthy breast tissue environment (distances in cm, pSNR in dB)

Figure 2 shows the effect of distance on the resolution of the observed image. One can observe the ballistic observation with Bonferroni Correction testing width size increasing dramatically as $d \rightarrow d_{critical}$ (numerically found here to be =1.73cm), this is due to the Bonferroni Correction being a very conservative estimate. For $d \geq d_{critical}$ one can observe that the conventional imaging observation performs significantly better than the ballistic observation under Bonferroni ($w_{bal(bon)}^t \geq w_{conv}^t$). As stated previous, the Bonferroni Method obtains a lower bound for the resolution of the observation while retaining the false alarm rate. Using the higher resolution False Discovery Rate (FDR) approach, we obtain a higher SNR than the conservative Bonferroni approach while maintaining the false alarm rate. A point of interest is that the filter window will generally contain both occluding and non-occluding points (non-ideal case), but this does not greatly degrade the reconstruction quality.

5. CONCLUSIONS

Using the decision-theoretic analysis approach, it is shown that the resolution of the turbid medium, the smallest reliably resolved object (in terms of the width w^t) for both the conventional imaging and ballistic regimes, can be derived. For the ballistic regime, a trade-off between resolution, distance, laser intensity and confidence level was shown. The ballistic regime was considered under two multiple hypothesis test method, the Bonferroni Correction and False Discovery Rate. Under the conservative Bonferroni Correction, the optimal choice between ballistic and conventional imaging was derived and can be used to find the best reconstruction technique for a given system as a function of the parameters of the medium. Using the False Discovery Rate approach, it was shown how to obtain a higher resolution observation while still maintaining a specified false alarm rate.

6. REFERENCES

[1] A. H. Gandjbakhche, R. Nossal, and R. F. Bonner, "Resolution limits for optical transillumination of abnormalities embedded in tissues," *Medical Physics, vol. 22*, pp. 185-191, 1994.

[2] A. H. Gandjbakhche, G. H. Weiss, R. F. Bonner, and R. Nossal, "Photon path-length distributions for transmission through optically turbid slabs," *Phys. Rev. E 48*, pp. 810-818, 1993.

[3] S. Fantini, S. A. Walker, M. A. Franceschini, M. Kaschke, P. M. Schlag, K. T. Moesta "Assessment of the size, position, and optical properties of breast tumors in vivo by noninvasive optical methods," *Appl. Opt., vol. 37*, pp. 1982-1989, 1998.

[4] F. J. Anscombe "The Transformation of Poisson, Binomial and Negative-Binomial Data," *Biometrika, vol. 35*, pp. 246-254, 1948.

[5] R. G. Miller "Simultaneous Statistical Inference," Springer-Verlag, 1991.

[6] M. Pacifico, C. Genovese, I. Verdinelli, L. Wasserman "False Discovery Control for Random Fields," *Journal of American Statistical Association, vol. 99*, pp. 1002-1014, 2004

MAXIMUM LIKELIHOOD METHODS FOR
TIME-RESOLVED IMAGING THROUGH TURBID MEDIA

Brian Eriksson and Robert Nowak

University of Wisconsin - Madison
Department of Electrical and Computer Engineering
1415 Engineering Drive, Madison, WI 53706
bceriksson@wisc.edu, nowak@engr.wisc.edu

ABSTRACT

Recently technological advances now enable time-gated acquisitions of photons at very fast rates. This can allow one to separate scattered and unscattered photons in transillumination imaging. Time-resolved transillumination (TRT) imaging opens the door to an new type of imaging through turbid (scattering) media such as soft tissue and fog/smoke, and exciting potential applications in bioimaging and surveillance. This paper proposes a novel Maximum Likelihood based approach to TRT image reconstruction.

Index Terms— Image reconstruction, Poisson processes, EM Algorithm, Time-resolved Transillumination Imaging

1. TIME-RESOLVED TRANSILLUMINATION IMAGING

Recently technological advances now enable time-gated acquisitions of photons at very fast rates, fast enough to separately collect unscattered (first arrival) and scattered (later arrival) photons in transillumination imaging [1]. We refer to this technology as time-resolved transillumination (TRT) imaging, which is described in more detail in the next paragraph and depicted in Fig. 1. TRT opens the door to an new type of imaging turbid (scattering) media (e.g., soft tissue, fog/smoke). The ability to separately detect unscattered or *ballistic* photons can enable much higher resolution imaging than possible using conventional imaging devices, and this has exciting potential applications in bioimaging and surveillance. However, the number of ballistic photons decays exponentially fast as the thickness/depth of the turbid medium increases. Therefore, the high resolution information that is available is also in a very low SNR regime. This paper explores a novel approach to TRT image reconstruction.

In more detail, the TRT imaging problem involves of photons traveling through a turbid medium from an source, through an object plane, and then onto an imaging plane as depicted in Fig. 1. Photons traveling through a scattering medium can be roughly classified into three types: ballistic, snake, and diffuse. Ballistic photons experience no scattering and travel in a direct line of sight arriving first at detectors in the image plane. Because of the lack of scattering, ballistic photons retain their spatial information and arrive at the imaging plane at the same relative location as sent from the object plane. Snake photons experience some slight scattering through the medium, this scattering will cause these photons to arrive later than the ballistic photons and likely in a slightly different location than sent from the object plane. Diffuse photons experience large amounts of scattering and arrive at the image plane having lost most of their point of origin information. Due to the large number of scattering events through the medium, the diffuse photons will travel the farthest distance to the image plane, and therefore will arrive after the snake and ballistic photons. While the inherent spatial information decreases in order of ballistic, snake and diffuse photons, the number of photons (and hence inherent SNR) increases in the same order. So we are face with high resolution, low SNR data at one extreme (ballstic), and low resolution, high SNR data at the other (diffuse). Furthermore, the diffusion and SNR parameters, which characterize the underlying point spread function (PSF), are not known precisely in practice.
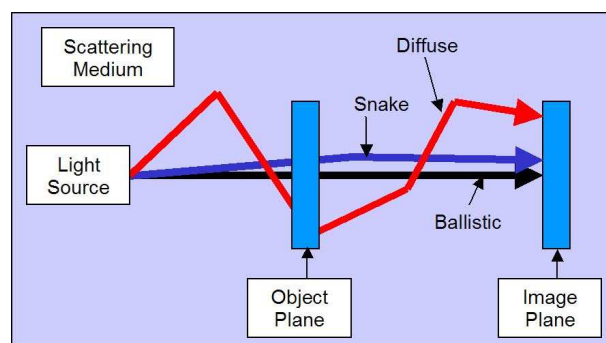
Fig. 1. Example of Photons Through a Scattering Medium

The TRT image reconstruction problem is essentially a statistical inverse problem (a particular form of photon-limited image reconstruction), but to the best of our knowledge our work here is the first to formally pose it as such. Due to uncertainties in the PSF, the TRT problem somewhat related to blind image deconvolution (BID). While BID is a well-studied problem, there are several unique aspects in the TRT imaging problem that make it quite different from standard BID problems. In particular, the distinctive features of TRT imaging include the photon-limited nature of the data, the time-gated data acquisition which in effect yields information at multiple spatial resolutions that can be fairly well characterized via a diffusion equation, and most importantly the availability of "unblurred" data corresponding to the ballistic photons. For these reasons "off-the-shelf" BID algorithms are not directly applicable to TRT image reconstruction.

This paper is organized as follows. In Section 2 we propose a statistical model for TRT imaging through a homogeneous turbid medium. In Section 3 we review a multiscale Poisson denoising technique that can be applied directly to the ballistic data, and will also be an integral component of our overall reconstruction procedure. In Section 4 we show that an Expectation-Maximization (EM) algorithm based on the Poisson denoising scheme can be used to solve the image reconstruction problem when one has perfect knowledge of the scattering properties of the medium. In Section 5 we propose a novel scheme (based on the EM algorithm) for computing the joint Maximum Penalized Likelihood Estimate of the underlying image intensity and key diffusion and SNR parameters of the scattering environment. Section 6 evaluates the performance of our scheme in simulations and concluding remarks are made in Section 7.

2. A STATISTICAL MODEL OF TRANSILLUMINATION IMAGING

The basic statistical model we propose for TRT imaging through homogeneous turbid media is as follows. Assume that we have k time-resolved "snapshots" , each acquired over disjoint time intervals $T_1, \ldots, T_k$, with T_1 denoting the ballistic time interval. Assume that these intervals form a uniform partition of the overall observation interval T. Let $X_1, \ldots, X_k$ denote the photon data acquired in each interval, respectively. Specifically, the data X_i are acquired in the form of an n-pixel image, and for our mathematical exposition we assume that the columns of this image are "stacked" to form an $n \times 1$ vector. Each pixel value in X_i is simply the number of photons detected at the corresponding location during the time interval T_i. Each image is Poisson distributed according to the following model:

$$X_i \quad \sim \quad \text{Poisson}(\alpha_i P_i \lambda), \;\; i = 1, \ldots, k, \qquad (1)$$

where λ denotes the underlying $n \times 1$ image intensity function, P_i denotes the $n \times n$ photon transition matrix from the

emission (source) plane to the detection (image) plane, and $\alpha_i > 0$ is a scalar gain factor. The transition matrices are functions of time and a scalar diffusion bandwidth parameter denoted by σ^2. In particular, according to the basic physics of photon propagation through turbid media [1], row s of P_i is a probability mass function modeled by a sampled Gaussian density with mean s and variance proportional to $\sigma^2 t_i$, where t_i denotes the midpoint of the i-th acquisition time-interval. Thus, the transition matrices are parametric functions of the form $P_i = P(\sigma^2 t_i)$. We assume that λ is normalized such that the intensities in λ sum to one (i.e., $\sum_{j=1}^n \lambda_j = 1$). Also the transition matrices are normalized so that $\mu_i = P_i \lambda$ also satisfies $\sum_{j=1}^n \mu_{i,j} = 1$. With these normalizations, it is easy to verify that the "total" intensity (integrated spatially over the image plane and temporally over the i-th time-interval) is α_i. Furthermore, we adopt the convention that the ballistic image resolution is the finest spatial resolution available and assume that $P_1 = I_{n \times n}$, the $n \times n$ identity matrix. We also assume that the images acquired in each time-interval are statistically independent, and so the joint distribution function of the entire data record $X = [X_1^T, \ldots, X_k^T]^T$ (the superscript T denotes matrix transposition) is

$$X \quad \sim \quad \text{Poisson}(P\lambda), \qquad (2)$$

where P is the $kn \times n$ transition matrix obtained by stacking the matrices $\alpha_1 P_1, \ldots, \alpha_k P_k$; i.e., $P = [\alpha_1 P_1^T, \ldots, \alpha_k P_k^T]^T$.

Let us constrast this imaging system with a conventional system in which the photon detections are not time-resolved. In this case, we acquire the aggregated photon image $X_a = X_1 + \cdots + X_k$ which obeys the model

$$X_a \quad \sim \quad \text{Poisson}(P_a \lambda), \qquad (3)$$

where $P_a = \sum_{i=1}^k \alpha_i P_i$. We will see that the extra "information" available in the time-resolved photon acquisition can significantly improve our ability to estimate the underlying intensity λ.

3. PHOTON-LIMITED IMAGE DENOISING

The ballistic photon image X_1 has high spatial resolution but extremely poor SNR due to the very limited number of ballistic photons. As a starting point for our work, let us consider the problem of estimating the underlying image intensity based on the ballistic photon data alone. This boils down to a Poisson image "denoising" problem, which has recently received a significant amount of attention in the image processing and statistics literature.

One state-of-the-art Poisson denoising scheme is based on the recursive dyadic partition (RDP) framework proposed in [2]. This scheme is a Poisson analog of the more familiar wavelet denoising methods developed for the classical "signal+noise" model. Also like wavelet denoising, additional improvements in denoising quality are possible using

a translation-invariant version of the basic approach [3, 4], which can be computed in $O(n \log n)$ operations.

The Poisson denoising method will be an integral component of our EM algorithm for time-resolved transillumination imaging. The EM algorithm optimally combines information from the entire record time-resolved photons (i.e., from the ballistic, quasidiffuse and diffuse limits). But before moving on, let us illustrate the performance of the method by estimating the underlying image intensity using only the ballistic photon data. Figure 2 depicts the results of denoising a ballistic photon image using the methodology described above (specifically, we employ the translation-invariant Haar estimation scheme described in [4] and implemented in the superb Matlab package developed by Prof. Rebecca Willett [5]). Note that the denoising method results in an intensity estimate that reduces "noise" while preserving edges and other details.

(a) Image Intensity   (b) Ballistic Data   (c) MPLE
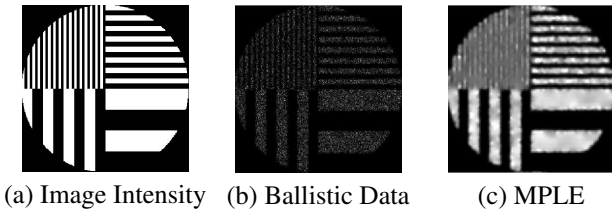
Fig. 2. Example of ballistic photon image MPLE denoising.

4. AN EM ALGORITHM FOR IMAGE RECONSTRUCTION

If the attenuation factors $\{\alpha_i\}$ and scattering matrices $\{P_i\}$ are known, then the MLE of λ given X (or given X_a) can be computed using the well-known Expectation-Maximization (EM) algorithm [6]. For the general problem, the standard E and M steps are computed using X and P, while in the case of aggregated photon data the steps employ X_a and P_a. The algorithm is initialized with a starting guess for MLE of λ (e.g., all pixels set to 1).

Under mild conditions, the sequence of estimates converges to an MLE solution. Unfortunately, because P is usually poorly-conditioned, the exact MLE solution is usually undesirable. For example, in the case of the ballistic data alone, the MLE of λ is simply X_1, which as seen from Figure 2, is highly variable and typically has a very poor MSE. So, instead of seeking the MLE we aim to recover a Maximum Penalized Likelihood Estimate (MPLE), using the Poisson denoising criterion described in Section 3 as our penalty term. This MPLE approach was first proposed in [7]. The MPLE can also be computed using the EM algorithm. In this case, the E-Step remains the same as above and the M-Step is computed by applying the translation-invariant denoising algorithm [4, 5] to the usual M-step result prior to re-computing the E-Step (see [7] for further details).

5. ADAPTING TO UNKNOWN TURBID MEDIA

One of the major challenges in practical imaging problems is that the characteristics of the turbid medium are usually not known precisely. In particular, the values of system parameters $\{\alpha_i\}$ and σ^2 are unknown and therefore must be estimated along with λ. We can formulate this as a joint MLE problem, seeking to find values of the system parameters and λ which jointly maximize the Poisson likelihood function (or penalized likelihood). At first glance, it may appear that this joint MLE problem may be intractable, but it turns out to have a rather simple solution which is one of the main contributions of this paper.

The basic solution approach is as follows. First, the MLEs of the gain factors $\{\alpha_i\}_{i=1}^k$ can be computed separately from λ and σ^2 due to the following observation. Consider the statistics

$$S_i = \sum_{j=1}^{n} X_{i,j}, \ \ i = 1, \ldots, k,$$

the subscript j indexes the pixels in each image. These statistics are simply the total photon counts for each image. Due to the normalization of λ and the matrices $\{P_i\}$ in our model, it follows that

$$S_i \ \sim \ \text{Poisson}(\alpha_i), \ \ i = 1, \ldots, k.$$

It is well-known that the conditional distribution of X_i given S_i is multinomial with parameters $\mu_i = P_i\lambda$ (see [2]). Therefore, the likelihood factorizes into Poisson factors, each involving one pair (α_i, S_i), and multinomial factors, each involving λ and one triple (P_i, X_i, S_i). Consequently, the MLEs of the gain factors $\{\alpha_i\}$ can be obtained separately from λ and σ^2 and are given by the simple formula $\widehat{\alpha}_i = S_i$, $i = 1, \ldots, k$. Now recall that the matrices $\{P_i\}$ are parametric in σ^2. To find the MLEs of λ and σ^2 we consider a range of candidate values for σ^2 and for each one we use the EM algorithm described above (with each α_i set to its MLE $\widehat{\alpha}_i$) to compute the MPLE, denoted by $\widehat{\lambda}(\sigma^2)$, and the corresponding maximum penalized likelihood value, denoted $L(\sigma^2)$. This can be done exhaustively (over a discretized range of σ^2 values) or systematically (assuming unimodality of the maximum penalized likelihood as a function of σ^2 and employing a bisection method). The value of σ^2 that results in the highest penalized likelihood value $L(\sigma^2)$ is the MLE of σ^2, denoted $\widehat{\sigma^2}$. The MLE of λ is then $\widehat{\lambda}(\widehat{\sigma^2})$.

6. A TRT IMAGING EXAMPLE

The potential of the proposed EM algorithm is evaluated in the following simulation study. Using the λ intensity function depicted in Figure 2a, a ballistic image is generated using low photon count Poisson data and a diffuse image is generated by first blurring λ using a high variance blurring kernel and then

generating a large number of photons from the blurred intensity function. The reconstruction based only on the ballistic photon data is depicted in Figure 2c, and the reconstruction using only the diffuse image and assuming perfect knowledge of the blurring variance σ^2 is depicted in Figure 3a). Figure 3b shows the reconstruction based on both ballistic and diffuse photon data and assuming perfect knowledge of attenuation factors (α_1, α_2) and blurring variance (σ), using the EM algorithm described in Section 4. Using the adaptive MLE scheme described in Section 5, the attenuation factors and blurring variance were jointly estimated along with λ, and the resulting intensity estimate shown in (Figure 3c). Table 1 summarizes the reconstuction errors over 10 independent trials of the experiment. As expected, the combined (ballistic+diffuse) oracle reconstruction performs best, with the combined reconstruction with ML estimation of the gain and diffusion parameters close behind.

The algorithm developed in Section 5 the final reconstruction is the estimate with largest likelihood value chosen from a set of reconstructed images generated using different σ^2 values. In all our experiments, the likelihood appears to be unimodal in σ^2 (one such likelihood is seen in (Figure 3d)), allowing for systematic searches such as a bisection method. We conjecture that the likelihood is always unimodal in σ^2, but we have not yet proved this result.
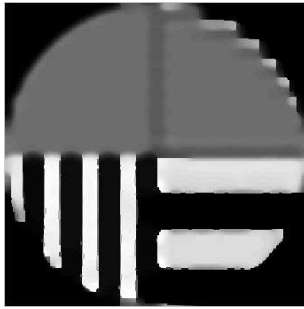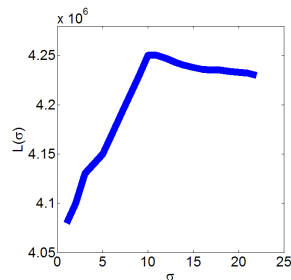

(a) MPLE Diffuse
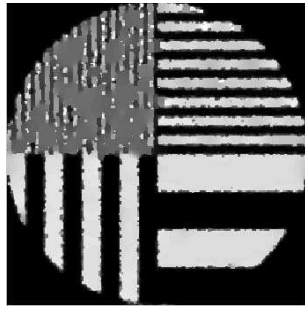
(b) MPLE Ballistic + Diffuse
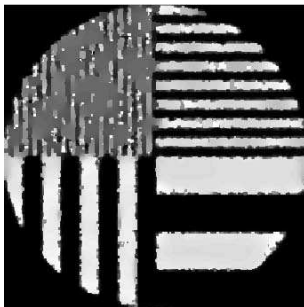
(c) MPLE Ballistic + Diffuse
w/ Unknown parameters

(d) Log-Likelihood Plot

Fig. 3. Examples of TRT image reconstruction.

Table 1. Summary of TRT image reconstruction errors.

Image	PSNR (dB)
Ballistic Image	4.08
Diffuse Image	7.00
MPLE Ballistic	11.90
MPLE Diffuse	9.42
MPLE Ballistic + Diffuse	12.92
MPLE Ballistic + Diffuse w/ unknown params	12.71

7. CONCLUSIONS

This paper proposed a novel MLE reconstruction algorithm for TMT imaging. The algorithm is based on a combination of the EM algorithm and Poisson denoising. Our simulation study demonstrates the potential of our approach, in particular indicating the added benefit of optimally fusing ballistic and diffuse photon data. Our future work includes the application of this theory to real-data experiments, detailed analysis of fundamental performance limits in TRT imaging, and extensions to inhomogeneous media.

8. REFERENCES

[1] J. A. Moon, P. R. Battle, M. Bashkansky, R. Mahon, M. D. Duncan, and J. Reintjes, "Achievable spatial resolution of time-resolved transillumination imaging systems which utilize multiply scattered light," *Phys. Rev. E*, vol. 53, no. 1, pp. 1142–1155, Jan. 1996.

[2] E. Kolaczyk and R. Nowak, "Multiscale likelihood analysis and complexity penalized estimation," *Ann. Stat.*, vol. 32, pp. 500–527, 2004.

[3] R. Willett and R. Nowak, "Multiscale poisson intensity and density estimation," *submitted to IEEE Trans. Info. Th.*, 2005, preprint at www.ee.duke.edu/~willett/papers/WillettInfoTh2005.pdf.

[4] R. Willett and R. Nowak, "Fast, near-optimal, multiresolution estimation of poisson signals and images," in *Proc. Twelth European Signal Processing Conference — EUSIPCO '04*, Wien, Austria, 2004.

[5] R. Willett, "Fast translation-invariant poisson image reconstruction," 2005, on-line at www.ee.duke.edu/~willett/Research/FastTIHaar.html.

[6] Y. Vardi, L. Shepp, and L. Kaufman, "A statistical model for positron emission tomography," *J. Amer. Stat. Assoc.*, vol. 80, pp. 8–37, 1985.

[7] R. Willett and R. Nowak, "Platelets: A multiscale approach for recovering edges and surfaces in photon limited medical imaging," *IEEE Trans. Med. Im.*, pp. 332–350, 2003.